Influence of Composition and Morphology on the Electronic Properties of Semiconductor Nanostructures and Alloys

by

Christian M. Greenhill

A dissertation submitted in partial fulfillment
of the requirements for the degree of
Doctor of Philosophy
(Materials Science and Engineering)
in the University of Michigan
2021

Doctoral Committee:

Professor Rachel S. Goldman, Chair
Professor Cagliyan Kurdak
Professor Pierre Ferdinand P. Poudeu
Assistant Professor Liang Qi

Christian Greenhill

cmgreen@umich.edu

ORCID iD: 0000-0003-4913-9241

Acknowledgements

I would like to thank my advisor, Rachel Goldman, and my co-advisor Prof. Cagliyan Kurdak, for their support throughout my studies at the University of Michigan, as well as Profs. Ferdinand Poudeu, and Liang Qi for their time and guidance as members of my dissertation committee. I would like to thank Prof. Ganesh Balakrishnan for his insight on mechanisms related to quantum dots, Dr. Alexander Chang for his patient mentorship on STM and atom probe. I warmly thank the $(MC)^2$ staff for their training.

This dissertation would not have been possible without the support of my fellow group members, past and present. Thank you especially to Dr. Jenna Walrath, Gregory Cunningham, Grace Fedele, Dr. Jordan Occena, Dr. Tim Jen, Hongling Lu, Tao-Yu Huang, Jared Mitchell, Kyle Hammond, and Sam Frisone.

I would like to thank for their friendship and support, Dr. Crystal Green, Alelia Higgenbottom, Melanie Freeman, Dr. Corine Jackman, Dr. Davide del Gaudio, Dr. Rosalyn Kent, Dr. Kim Ransom, Lydia Mensah, and Deborah Payne. My personal and professional successes in this journey would not have been without Dr. Emma Flores-Scott, Crystal Ashby, Regina Hairston, Dr. Robert Marchini, and Dr. Barbara Bekis.

Finally, I deeply thank my husband, Charles Richmond, and my parents for their immense and tireless support. Couldn't have done it without any of you, truly.

I dedicate this dissertation to my son Prince-Charles A. Richmond, Jr.

Table of Contents

List of Figures

List of Tables

List of Appendices

Abstract

Recent advances in fabrication techniques have led to the successful nano-engineering of semiconductor heterostructures with nanometer-scale structures. Such heterostructures make it possible to tune band gap energies and control carrier confinement for a range of electronic and optoelectronic applications, including solar cells, light emitters, and quantum-computing applications. However, the nanoscale morphologies (i.e., sizes, shapes, and local compositions) of complex heterostructures and their influence on electronic characteristics are not fully understood. To address these issues, it is essential to probe materials on the nanoscale using advanced experimental and computational tools. Therefore, this dissertation focuses on investigating the effects of nanostructure morphologies on the electronic structure of epitaxially-grown semiconductor materials that employ alloying and/or low-dimensional structures (such as quantum dots). In particular, we investigate GaAsNBi and BiSbTe alloys, and InAs/GaAs and GaSb/GaAs quantum dots (QDs) using nanoscale experimental probes in conjunction with self-consistent Schrödinger-Poisson simulations using nextnano.

First, we demonstrate an approach to examine apparent stoichiometry in GaAs-based alloys and nanostructures using local electrode atom probe (LEAP) tomography, in conjunction with Rutherford Backscattering Spectrometry (RBS) and high-resolution x-ray diffraction (HRXRC). Using the LEAP conditions identified for achievement of near-stoichiometry in GaAs, we investigate local N and Bi compositions in GaAsNBi alloys and local Si concentrations in the vicinity of Si-doped InAs/GaAs QD superlattices. For the

GaAsNBi alloys, LEAP-determined average Bi compositions correlate with those determined using RBS. These are the first known studies that use LEAP to directly measure N and Bi compositions for GaAsNBi films. For Si-doped InAs/GaAs QD superlattices, 3D LEAP data reveals laterally and vertically inhomogeneous Si incorporation, with clusters of Si throughout the layers.Using the local In, Ga, As, and Si compositions from 3D LEAP data as input into Schrodinger-Poisson simulations, we find that electrons are predicted to be localized near both the QDs and the Si clusters.

Furthermore, we determined the distribution of compositions within Ga(As)Sb quantum dots (QDs), clusters, and circular arrangements of smaller QDs, termed QD-rings (QDRs) using LEAP. Sizes, shapes, and compositional gradients are used as input into self-consistent Schrödinger-Poisson simulations to compute confinement energies for individual nanostructure types. The computed confinement energies and the measured photoluminescence emission energies increase from QDs to QD-rings to 2D layers, enabling direct association of nanostructure morphologies with the optical properties of the GaSb/GaAs multilayers. This is the first known work that uses measured compositional gradients as input into 8 x 8 **k·p** calculations for Ga(As)Sb/GaAs nanostructures, opening opportunities for tailoring emission energies for near to far-infrared optoelectronics by varying the QD morphology.

Finally, we have investigated the bulk and local electronic states in $(Bi_{1-x}Sb_x)_2Te_3$ alloys using scanning tunneling spectroscopy (STS) and magnetoresistance (MR) measurements. STS reveals both the Fermi level and Dirac point located inside the bulk bandgap, indicating bulk-like insulating behavior with accessible topological surface states (TSSs). STS and reveals a transition from n-type to p-type conduction at $x \approx 0.6$. We use a

two-channel analysis of MR data to differentiate the charge carrier types for surface and bulk transport; we conclude that surface transport is dominated by electrons and bulk transport is dominated by holes. Prior to this work, direct detection of topological surface states in BiSbTe systems has been achieved only for T<10 K.

Chapter 1

Introduction

1.1 Overview

Over the past few decades, advances in thin film growth have enabled fabrication of semiconductor alloys and heterostructures of nanometer sizes.[1-25] For example, fabrication techniques, such as molecular beam epitaxy (MBE), allow for ternary and quaternary alloys to be grown as epitaxial layers on binary substrates with alloy compositions properly chosen to maintain lattice-matching.[26] Lattice-matching is important for reducing material defects, thus improving electronic characteristics. Furthermore, multilayered structures and superlattices with quantum dots (QDs) can also be grown, resulting in new material systems that feature a wide range of artificially engineered electronic characteristics. Such characteristics include the potential ability to control band gap energies, band alignments, carrier concentration, and carrier confinement for electronic and optoelectronic applications.[6,7,13,14,19,27-29]

Of particular interest to materials research is understanding the effects of nanostructure morphologies (i.e., size, shape, and local compositions) on the band structure in semiconductor films. For example, the incorporation of dilute species of nitrogen (N) and bismuth (Bi) into gallium arsenide (GaAs) leads to a large reduction in band gap energies,[30-32] allowing for access to a range of wavelengths in the near-infrared for lasers,

photodetectors, and ultra-high-efficiency solar cells.[33-36] It is expected that N primarily shifts the conduction band while Bi primarily shifts the valence band during co-alloying, effectively allowing for independent control of the conduction and valence band offsets in heterostructures.[35,36] Second, growing three-dimensional nanostructures, such as GaSb QDs, within GaAs combines two different materials with different band structures, and the result is a band alignment or *band offset* at the GaSb QD-GaAs matrix interfaces. Through precise control of QD size, shape, and local compositions, band offsets can be tuned to control carrier confinement and redistribution for light emitting,[37] photovoltaic,[38] and memory storage applications.[39,40] Finally, the ability to tune the Fermi level, Dirac point, and conduction through alloying in BiSbTe films makes it possible for carrier type switching, which is useful for spintronic and quantum computing applications.[41-43]

Each of the material systems stated above employs the use of alloying (i.e., with Sb, Bi, and/or N) and/or the incorporation of low-dimensional nanostructures (i.e., QDs) to alter the conduction and valence band positions. Resultant changes to their electronic and optical characteristics are not yet completely understood. Challenges lie within the uncertainties of how alloying and nanostructuring influence strain and defects within the material and at interfaces. Therefore, for unleashing the full potential of nanotechnology, understanding physics at the nanoscale level and further development of nanoscale techniques for probing these material systems are essential. This dissertation describes our explorations of the structural-property relationships in epitaxially-grown semiconductor films, specifically GaAsNBi/GaAs epilayers, InAs/GaAs QD superlattices, GaSb/GaAs multilayers, and BiSbTe alloys using combined experimental-computational approaches.[44]

The following projects are described in this dissertation: (1) Investigating the role of pulsed-voltage vs. pulsed-laser mode, and the respective laser energies on the apparent stoichiometry in GaAs layers. Using the LEAP conditions identified for the nearest stoichiometry for GaAs, we apply this approach to investigate local N and Bi compositions in GaAsNBi alloys and local Si concentrations in the vicinity of Si-doped InAs/GaAs QD superlattices. Dilute nitride-bismide semiconductor alloys are of emerging interest for long-wavelength applications ranging from temperature-insensitive laser diodes to ultra-high efficiency multijunction photovoltaic cells.[45] (2) The use of nanoscale microscopic techniques, such as transmission electron microscopy (TEM) and local electrode atom probe tomography (LEAP or APT) to evaluate size, shape and compositional gradients within GaSb/GaAs quantum dots (QDs): Structural data from these experiments are used to evaluate their electronic and optical characteristics for potential use in near- to far-infrared devices. (3) The probing of electronic states and carrier transport in BiSbTe alloys using scanning tunneling microscopy/spectroscopy (STM/S) and magnetotransport measurements: BiSbTe alloy compositions and film thickness dependence on band structure and transport properties are discussed.

Chapter 1 begins by describing the properties of compound semiconductors and highlighting their use in emerging technologies. Concepts of band structuring engineering are presented, followed by an overview of the methods used for investigating the material systems in this work. Finally, the outline for this dissertation is presented.

1.2 Band structure engineering for optoelectronic devices

The electronic and optical properties of semiconductor devices are primarily determined by the material system's energy band structure (i.e., band gap, band edge positions, confined or impurity states, and carrier dynamics). For light-emitting applications, such as lasers and light-emitting diodes, electrons in the conduction band and holes in the valence band recombine, and energy is released as photons of light. The energies of the emitted photons depend on the effective band gap of the device, which can be tuned by the heterostructure design. Inversely, for solar cell, photodetectors, and memory-storage applications, electron-hole pairs are generated after valence electrons absorb energies equal to or greater than the energy gap. Excited electrons are then transferred to the conduction band and can then be used to carry current or to store information, as for solar cell or memory applications, respectively. Like light emitters, conversion efficiencies between carriers and photons in solar cell applications depend on the device's band structure, as well as other carrier behavior within the material.

Epitaxially-grown compound semiconductor alloys that combine elements from group III and group V of the periodic table are at the heart of many modern optoelectronic applications. Advances in the nanoscale fabrication techniques that use III-V materials have made it possible to achieve a wide variety of energy bandgaps that are required for these applications. One method of altering the energy bandgap is through alloying semiconductors with solute atoms. The band anti-crossing (BAC) model[46] predicts that the addition of solute atoms leads to a formation of localized impurity states near the band edges (i.e. conduction and valence band edges), whose interaction with delocalized states of the crystal will lead to band splitting. Due to alloying, the effective conduction and valence band edges shift, and the band gap can be described by an interpolation between

the band gaps of its constituent elements or compounds. For example, the band gap, E_g, of an alloy $A_{1-x}B_x$, is typically described as a linear interpolation between the bandgaps of its binary constituents, A and B, modified by a bowing parameter, b:[26]

$$E_g(A_{1-x}B_x) = (1-x)E_g(A) + xE_g(B) - bx(1-x) \quad (1.1)$$

The band gap versus lattice parameter for several binary III-V compounds is shown in Figure 1.1. The bowed solid lines between points represent the bandgaps and lattice parameters of ternary (quaternary) compounds formed by alloying the corresponding binary (ternary) compounds, e.g., $GaAs_{1-x}Sb_x$ formed by alloying GaAs and GaSb ($GaAsN_{1-x}Bi_x$ formed by alloying GaAsN and GaAsBi). As evident in Figure 1.1, the change in bandgap achieved by alloying compounds is accompanied by a change in lattice parameter, where the lattice parameter of the alloy typically follows Vegard's Law,[47] expressed as a linear interpolation of the lattice parameters of the binary compounds. For epitaxially-grown semiconductor alloys, it is usually necessary for the alloy lattice parameter to closely match that of the substrate to avoid strain-driven formation of crystal defects and dislocations[48] that may be detrimental to device performance. Therefore, a semiconductor alloy should ideally be capable of accessing a range of bandgaps corresponding to technologically important wavelengths while being nearly lattice-matched to a commercially available substrate material, such as those marked by vertical gray bars in Figure 1.1.

An alternative method of engineering the band structure as opposed to alloying involves using semiconductor heterostructures, where semiconductors with different band gap energies are superimposed, as for quantum wells (QWs), nanowires (NWs), and quantum dots (QDs). Due to the different energy positions of the conduction and valence

band edges of the joined semiconductors, a band alignment or *band offset* is created at the interface. The band alignment can be tuned for specific applications by superimposing different semiconductors. Figure 1.2 shows a simplified schematic of the energy potential for two different heterostructure systems. A type-I band alignment, as shown in Figure 1.2(a), facilitates radiative electron-hole recombination, which is useful for light emitting diodes and lasers. On the other hand, a type-II alignment, as shown in Figure 1.2(b), leads to a spatial separation of charge carriers (i.e., electrons and holes), which is useful for solar cells and charge-based memory applications. For several technologically important III-V and II-V quantum systems, there are conflicting reports in the literature regarding precise band offset values and alignment types. For example, in the GaAsSb/GaAs material system, a type-I alignment with $\Delta E_c \sim 35$meV is reported for Sb mole fractions of 0.12[49] and 0.30,[50] respectively in two different studies. Contradictory, a type-II band alignment with offset ratios (Q_v) ranging from 1.05 to 2.1 is also reported in separate studies.[51-57] Due to the large discrepancies, offset values are often averaged, which can be misleading when predicting the band structure. In this work, we explore nanoscale compositions within GaSb/GaAs heterostructures (QWs and QDs) and use structural information to calculate the band alignment within this system.

1.3 Self-assembled semiconductor quantum dots (QDs)

Self-assembled semiconductor QDs form spontaneously due to the relaxation of strain energy in epitaxial systems where the lattice parameter of the deposited material is larger than that of the underlying material. QDs confine charge carriers in three directions. Though QDs are promising for a variety of optoelectronic applications, a variety of issues

plague these devices, such as non-radiative carrier recombination, carrier trapping, and dark current.[58,59] In addition, non-uniformities, such as inhomogeneous dot, size, shape, and compositions lead to broadening of the density of energy states, which lower device efficiencies. Further advances in QD devices require an improved understanding and control of dot morphology (i.e., size, shape, and composition). In this work, we use local electrode atom probe (LEAP) tomography, which can measure local changes in size and compositions, to obtain three-dimensional images of atoms within QDs. Used in conjunction with transmission electron microscopy (TEM), an overall study of QD structural morphology is described. Structural information from LEAP experiments is then used as input to model the electronic structure of QD systems. More details on LEAP and TEM are described in Chapter 2, while LEAP investigations of Si-doped InAs/GaAs QDs and GaSb/GaAs QDs are presented in Chapters 3 and 4, respectively.

1.4 Topological insulators

Topological insulators (TIs) have a unique band structure, recently emerging as an exciting class of quantum materials that stands on the boundary between insulation and conductance. TIs have an insulating energy gap in the bulk with gapless, metallic edge or topological surface states (TSSs), as shown in Figure 1.3. The surface states operate as a pair of topological transport channels confined to the sample's surface. Spin-polarization in TSSs has two primary consequences: (1) The orientation of the spin can be controlled by reversing the direction of the applied current, opening up a wide range of potential applications including quantum computing and spintronic devices, and (2) spin-momentum locking suppresses backscattering, resulting in ultra-high carrier mobility.[60-63] Many

recently discovered topological insulators are also well-known thermoelectric materials, such as Bi_2Te_3, Sb_2Te_3, Bi_2Se_3, and related compounds. It has been proposed that these highly mobile TSSs may be capitalized upon to enhance thermoelectric efficiency by carefully tuning the interactions between the surface and bulk states.[64-66]

Bi_2Te_3-Sb_2Te_3 alloys are of particular interest for topological insulator applications. Alloying these two binary compounds has been reported to induce a mid-gap Dirac point (E_D), allowing for a decoupling of bulk and surface transport.[67,68] We probe the TSSs of Bi_2Te_3-Sb_2Te_3 alloys using scanning tunneling spectroscopy (STS) and locate their Dirac points at room temperature. In addition, STS reveals both compositional and film thickness dependencies on E_F, resulting in n-type, p-type, and/or mixed-carrier type conduction.[63] Such characteristics are ideal for applications that can use the dynamics of carrier switching for storing and manipulating information (i.e., quantum computers). We probe the carrier dynamics within these films using magnetoresistance and Hall transport measurements. Details of these STS and magnetotransport measurements are also described in Chapter 2, while details of their use for the BiSbTe alloys are presented in Chapter 5.

1.5 Outline of the dissertation

This dissertation is organized as follows. In Chapter 2, the experimental and computational techniques used for the growth and characterization of GaAsNBi films, Si-doped InAs/GaAs QDs, GaSb/GaAs multilayers, and BiSbTe films are described, including molecular-beam epitaxy (MBE), electron microscopy, local electrode atom probe (LEAP) tomography, photoluminescence (PL) spectroscopy, scanning tunneling microscopy/spectroscopy (STM/S), magneto-transport measurements, and nextnano.

While LEAP is emerging as an important technique for advancing semiconductor materials research, [69,70] the evaporation effects of group III-V alloys are not yet completely understood,[71,72] which presents challenges in estimating apparent stoichiometric ratios in III-V materials. In Chapter 3, we demonstrate an approach to examine apparent stoichiometry in GaAs-based alloys and nanostructures using local electrode atom probe (LEAP) tomography, in conjunction with Rutherford Backscattering Spectrometry (RBS) and high-resolution x-ray diffraction (HRXRC). We examine the role of pulsed-voltage vs. pulsed-laser mode, analyzing atomic fractions for both cases when the 75 (150) Da peak is assigned to As^+ or As_2^{2+} (As_2^+ or As_4^{2+}). Using the LEAP conditions identified for achievement of near-stoichiometry in GaAs, we investigate local N and Bi compositions in GaAsNBi alloys and local Si concentrations in the vicinity of Si-doped InAs/GaAs QD superlattices. For the GaAsNBi alloys, LEAP-determined average Bi compositions correlate with those determined using RBS. These are the first known studies that use LEAP to directly measure N and Bi compositions for GaAsNBi films. For Si-doped InAs/GaAs QD superlattices, 3D LEAP data reveals laterally and vertically inhomogeneous Si incorporation, with clusters of Si throughout the layers. Using the local In, Ga, As, and Si compositions from 3D LEAP data as input into Schrodinger-Poisson simulations, [73] we find that electrons are predicted to be localized near both the QDs and the Si clusters. The study presents a wholistic view of evaporation behaviors present in a range of III-V materials that have been investigated in the Goldman group using LEAP, including extensions of work previously presented by Dr. Tim Jen[74] and Dr. Jenna Walrath.[75]

Chapter 4 presents our investigation for characterizing the nanoscale morphology of GaSb/GaAs multilayers with and without 3D nanostructures using scanning transmission electron microscopy (STEM) and LEAP. In these experiments, atomic structures ranging from QDs to quantum-dot rings (QDRs) and clusters are observed, which is common for this material system. Using nanostructure sizes and shapes from STEM and local Sb compositions from LEAP as input into self-consistent Schrödinger-Poisson simulations, the confinement energies for GaSb QDs, QDRs, and 2D layers are computed using nextnano. The computed confinement energies and the measured photoluminescence emission energies increase from QDs to QD-rings to 2D layers, enabling direct association of nanostructure morphologies with the optical properties of the GaSb/GaAs multilayers. This is the first known work that uses measured compositional gradients as input into 8 x 8 $\mathbf{k}\cdot\mathbf{p}$ calculations for Ga(As)Sb/GaAs nanostructures, opening opportunities for tailoring emission energies for near to far-infrared optoelectronics by varying the QD morphology.

In Chapter 5, we present our investigations of the local band structure and carrier transport in topologically insulating $(Bi_{1-x}Sb_x)_2Te_3$ thin films using scanning tunneling microscopy/spectroscopy (STM/S) and magneto-transport measurements. STS reveals both the Fermi level and the Dirac point located inside the bulk band gap, indicating bulk-like insulating behavior with accessible TSSs. STS reveals a transition from n-type to p-type conduction at $x \approx 0.6$. We use a two-channel analysis of MR data to differentiate the charge carrier types for surface and bulk transport; we conclude that surface transport is dominated by electrons and bulk transport is dominated by holes. Finally, in Chapter 6, a summary and suggestions for future work are presented.

1.6 Figures

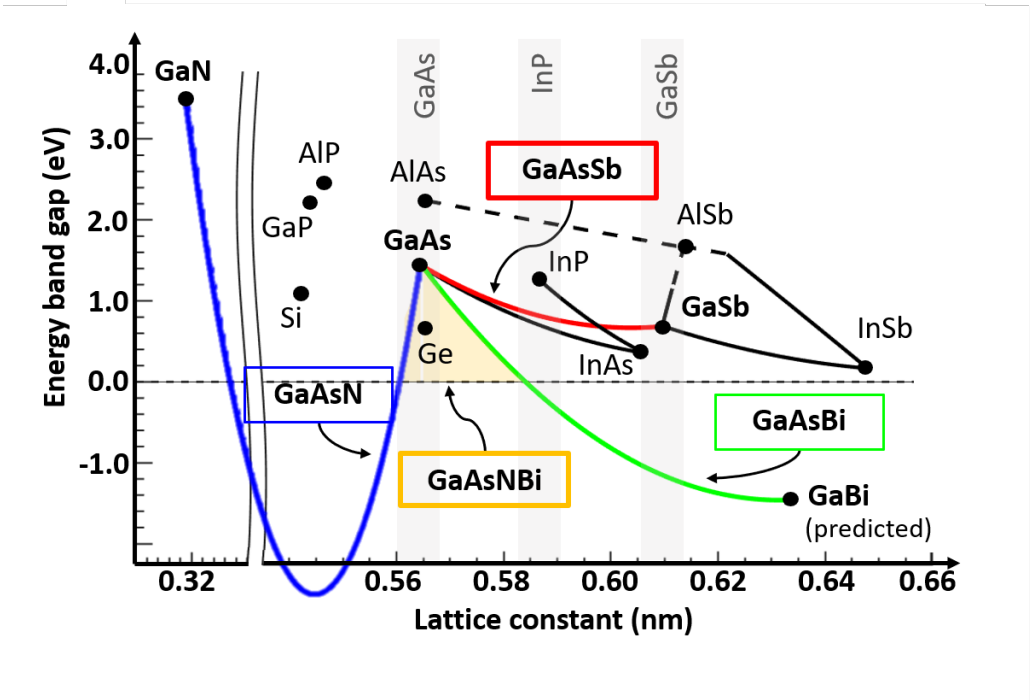

Figure 1.1 Lattice parameter versus energy band gap for common group III-V binary compound semiconductors. Solid lines between two points represent the direct band gaps and lattice parameters for ternary (quaternary) alloys composed of their constituent binary (ternary) compounds. For example, the incorporation of Sb within GaAs reduces the band gap energies into the infrared region of the visible spectrum, as indicated by the red line. Similarly, co-incorporation of both N and Bi within GaAs gives access to a wide range of band energies, while remaining lattice-matched with GaAs, as shown by the orange shaded region. Gray vertical bars indicate the lattice parameters of several commercially available substrates. Adapted from Ref 76.[76]

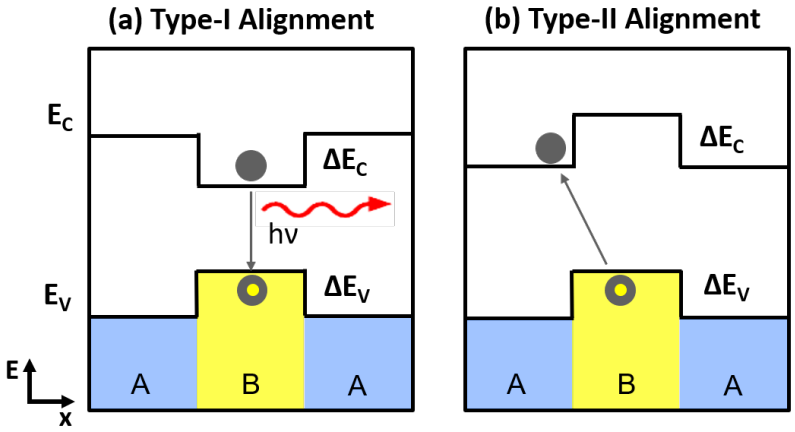

Figure 1.2 Simplified schematic of the energy potential for two different semiconductor materials, A and B, superimposed. (a) Type-I band alignment: Electrons and holes within material B recombine for spontaneous light emission, which is useful for lasers and light-emitting diodes. (b) Type-II band alignment: Electrons in material A and holes in material B are spatially separated, prohibiting spontaneous recombination, which is useful for solar cell and charge-based memory applications. Conduction band offsets (ΔE_{CB}) and valence band offsets (ΔE_{VB}) are determined by the energy difference between the conduction band edges and valence band edges, respectively, of the two different semiconductor materials, A and B.

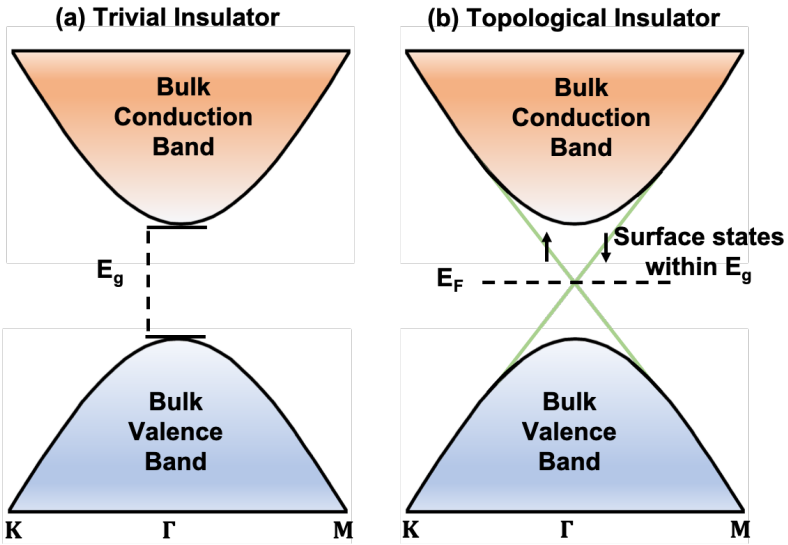

Figure 1.3 (a) Schematic representation of the energy bands (i.e., bulk conduction band [BCB] and bulk valence band [BVB]) as a function of momentum for a trivial insulator. The energy band gap (E_g) is the difference between the lowest point of the BCB and highest point of the BVB. (b) Schematic representation of surface energy levels in a 2D topological insulator as a function of crystal momentum. The shaded region shows the BCB and BVB (i.e., the bulk continuum states), and the lines show discrete surface bands localized near one of the surfaces.

1.7 Reference

[1] Y. Horikoshi, M. Kawashima, and H. Yamaguchi, "Low-Temperature Growth of GaAs and AlAs-GaAsQuantum-Well Layers by Modified Molecular Beam Epitaxy", Jpn. J. Appl. Phys. 25, L868 (1986).

[2] G.M. Guryanov, G.E. Cirlin, V.N. Petrov, N.K. Polyakov, A.O. Golubok, S.Y. Tipissev, V.B. Gubanov, Y.B. Samsonenko, N.N. Ledentsov, V.A. Shchukin, M. Grundmann, D. Bimberg, and Zh.I. Alferov, "STM and RHEED Study of InAs/GaAs Quantum Dots Obtained by Submonolayer Epitaxial Techniques", Surf. Sci. 352, 651 (1996).

[3] J.-I. Chyi, T.-E. Nee, C.-T. Lee, J.-L. Shieh, and J.-W. Pan, "Formation of Self-organized $In_{0.5}Ga_{0.5}As$ Quantum Dots on GaAs by Molecular Beam Epitaxy", J. Crystal Growth 175-176, 777 (1997).

[4] T. Haga, M. Kataoka, N. Matsumura, S. Muto, Y. Nakata, and N. Yokoyama, "Interdiffusion Between InAs Quantum Dots and GaAs Matrices", Jpn. J. Appl. Phys. 36, L1113 (1997).

[5] G.E. Cirlin, V.N. Petrov, V.G. Dubrovskii, A.O. Golubok, S.Y. Tipissev, G.M. Guryanov, M.V. Maximov, N.N. Ledentsov, and D. Bimberg, "Direct Formation of InGaAs/GaAs Quantum Dots During Submonolayer Epitaxies from Molecular Beams", J. of Phys. 47, 379 (1997).

[6] D. Loss and D.P. DiVincenzo, "Quantum Computation with Quantum Dots", Phys. Rev. A 57, 120 (1998).

[7] J.D. Phillips, K. Kamath, and P.K. Bhattacharya, "Far-infrared Photoconductivity in Self-organized InAs Quantum Dots", Appl. Phys. Lett. 72, 2020 (1998).

[8] W. Cheng, Z. Zhong, Y. Wu, Q. Huang, and J. Zhou, "The Self-Organized $In_{0.25}Ga_{0.75}As$ Quantum Dots Grown by Migration Enhanced Epitaxy", J. Crystal Growth 183, 279 (1998).

[9] P.B. Joyce, T.J. Krzyzewski, G.R. Bell, B.A. Joyce, and T.S. Jones, "Composition of InAs Quantum Dots on GaAs (001): Direct Evidence for (In, Ga)As Alloying", Phys. Rev. B 58, R15981 (1998).

[10] P. Frigeri, A. Bosacchi, S. Franchi, P. Allegri, and V. Avanzini, "Vertically Stacked Quantum Dots Grown by ALMBE and MBE", J. Crystal Growth 201-202, 1136 (1999).

[11] Y. Horikoshi, "Advanced Epitaxial Growth Techniques: Atomic Layer Epitaxy and Migration-enhanced Epitaxy", J. Crystal Growth 201, 150 (1999).

[12] J. Phillips, P. Bhattacharya, S.W. Kennerly, D.W. Beekman, and M. Dutta, "Self-assembled InAs-GaAs Quantum-dot Intersubband Detectors", IEEE J. of Quantum Electonics 35, 936 (1999).

[13] A. Stintz, G.T. Liu, A.L. Gray, R. Spillers, S.M. Delgado, and K.J. Malloy, "Characterization of InAs Quantum Dots in Strained $In_xGa_{1-x}As$ Quantum Wells", J. of Vac. Sci. & Technol. B 18, 1496 (2000).

[14] E. Biolatti, R.C. Iotti, P. Zanardi, and F. Rossi, "Quantum Information Processing with Semiconductor Macroatoms", Phys. Rev. Lett. 85, 5647 (2000).

[15] A.D. Stiff, S. Krishna, P. Bhattacharya, and S. Kennerly, "High-detectivity, Normal-incidence, Mid-infrared ($\lambda \sim 4\mu m$) InAs/GaAs Quantum-dot Detector Operating at 150K", Appl. Phys. Lett. 79, 421 (2001).

[16] A. Rosenauer, D. Gerthsen, D. V. Dyck, M. Arzberger, G. Böhm, and G. Abstreiter, "Quantification of Segregation and Mass Transport in $In_xGa_{1-x}As$/GaAs Stranski-Krastanow Layers", Phys. Rev. B 64, 245334 (2001).

[17] J.O. Winter, T.Y. Liu, B.A. Korgel, and C.E. Schmidt, "Recognition Molecule Directed Interfacing Between Semiconductor Quantum Dots and Nerve Cells", Adv. Mater. 13, 1673 (2001).

[18] R. Songmuang, S. Kiravittaya, and O. G. Schmidt, "Shape Evolution of InAs Quantum Dots During Overgrowth", J. Crystal Growth 249, 416 (2003).

[19] H.Y. Liu, M. Hopkinson, C.N. Harrison, M.J. Steer, R. Frith, I.R. Sellers, D.J. Mowbray, and M.S. Skolnick, "Optimizing the Growth of 1.3 μm InAs/InGaAs Dots-in-a-well Structure", J. of Appl. Phys. 93, 2931 (2003).

[20] C. Heyn and W. Hansen, "Ga/In-intermixing and Segregation during InAs Quantum Dot Formation", J. Crystal Growth 251, 140 (2003).

[21] J.D. Song, Y.M. Park, J.C. Shin, J.G. Lim, Y.J. Park, W.J. Choi, I.K. Han, J.I. Lee, H.S. Kim, and C.G. Park, "Influence of Arsenic During Indium Deposition on the Formation of the Wetting Layers of InAs Quantum Dots Grown by Migration Enhanced Epitaxy", J. of Appl. Phys. 96, 4122 (2004).

[22] I.R. Sellers, H.Y. Liu, K.M. Groom, D.T. Childs, D. Robbins, T.J. Badcock, M. Hopkinson, D.J. Mowbray, and M.S. Skolnick, "1.3/spl mu/m InAs/GaAs Multilayer Quantum-dot laser with Extremely Low Room-temperature Threshold Current Density", Electronics Lett. 40, 1412 (2004).

[23] G. Costantini, A. Rastelli, C. Manzano, P. Acosta-Diaz, R. Songmuang, G. Katsaros, O. Schmidt, and K. Kern, "Interplay between Thermodynamics and Kinetics in the Capping of InAs/GaAs(001) Quantum Dots", Phys. Rev. Lett. 96, 226106 (2006).

[24] H. C. Yu, J. S. Wang, Y. K. Su, S. J. Chang, F. I. Lai, Y. H. Chang, H. C. Kuo, C. P. Sung, H. P. D. Yang, K. F. Lin, J. M. Wang, J. Y. Chi, R. S. Hsiao, and S. Mikhrin, "1.3-μm InAs-InGaAs Quantum-dot Vertical-cavity Surface-emitting Laser with Fully Doped DBRs Grown by MBE", IEEE Photon. Techn. Lett. 18, 418 (2006).

[25] J. M. Ulloa, C. Celebi, P. M. Koenraad, A. Simon, E. Gapihan, A. Letoublon, N. Bertru, I. Drouzas, D. J. Mowbray, M. J. Steer, and M. Hopkinson, "Atomic Scale Study of the Impact of the Strain and Composition of the Capping Layer on the Formation of InAs Quantum Dots", J. of Appl. Phys. 101, 081707 (2007).

[26] I. Vurgaftman and J.R. Meyer, "Band Parameters for III–V Compound Semiconductors and their Alloys", J. Appl. Phys. 89, 5815 (2001).

[27] G. Yusa and H. Sakaki, "Trapping of Photogenerated Carriers by InAs Quantum Dots and Persistent Photoconductivity in Novel GaAs/*n*-AlGaAs Field-effect Transistor Structures", Appl. Phys. Lett. 70, 345 (1997).

[28] A.D. Stiff-Roberts, "Quantum-dot Infrared Photodetectors: A Review", J. of Nanophotonics 3, 031607 (2009).

[29] "Dilute III-V Nitride Semiconductors and Material Systems", edited by A. Erol (Springer, Berlin, Heidelberg, 2008).

[30] M. Kondow, K. Uomi, K. Hosomi, and T. Mozume, "Gas-Source Molecular Beam Epitaxy of GaN_xAs_{1-x}Using a N Radical as the N Source", Jpn. J. Appl. Phys. 33, L1056 (1994).

[31] S. Francoeur, M.J. Seong, A. Mascarenhas, S. Tixier, M. Adamcyk, and T. Tiedje, "Band gap of $GaAs_{1-x}Bi_x$, $0 < x < 3.6\%$", Appl. Phys. Lett. 82, 3874 (2003).

[32] S. Tixier, M. Adamcyk, T. Tiedje, S. Francoeur, A. Mascarenhas, P. Wei, and F. Schiettekatte, "Molecular Beam Epitaxy Growth of $GaAs_{1-x}Bi_x$", Appl. Phys. Lett. 82, 2245 (2003).

[33] S.R. Bank, H. Bae, L.L. Goddard, H.B. Yuen, M.A. Wistey, R. Kudrawiec, and J.S. Harris, "Recent Progress on 1.55- μm Dilute-Nitride Lasers", IEEE J. Quantum Elect. 43, 773 (2007).

[34] I.P. Marko and S.J. Sweeney, "Progress Toward III–V Bismide Alloys for Near- and Midinfrared Laser Diodes", IEEE J. Quantum Elect. 23, 1501512 (2017).

[35] C.A. Broderick, M. Usman, S.J. Sweeney, and E.P. O'Reilly, "Band Engineering in Dilute Nitride and Bismide Semiconductor Lasers", Semicon. Sci. Tech. 27, 094011 (2012).

[36] S.J. Sweeney and S.R. Jin, "Bismide-nitride Alloys: Promising for Efficient Light Emitting Devices in the Near- and Mid-infrared", J. Appl. Phys. 113, 043110 (2013).

[37] S.-Y. Lin, C.-C. Tseng, W.-H. Lin, S.-C. Mai, S.-Y. Wu, S.-H. Chen, and J.-I. Chyi, "Room-temperature Operation type-II GaSb/GaAs Quantum-dot Infrared Light-emitting Diode", Appl. Phys. Lett. 96, 123503 (2010).

[38] Y. Shoji, R. Tamaki, and Y. Okada, "Multi-stacked GaSb/GaAs type-II Quantum Nanostructures for Application to Intermediate Band Solar Cells" AIP Adv. 7, 065305 (2017).

[39] M. Geller, C. Kapteyn, L. Müller-Kirsch, R. Heitz, and D. Bimberg, "450 meV Hole Localization in GaSb/GaAs Quantum Dots" Appl. Phys. Lett. 82, 2706 (2003).

[40] M. Hayne, R.J. Young, E.P. Smakman, T. Nowozin, P. Hodgson, J.K. Garleff, P. Rambabu, P.M. Koenraad, A. Marent, L. Bonato, A. Schliwa, and D. Bimberg, "The Structural, Electronic and Optical Properties of GaSb/GaAs Nanostructures for Charge-based Memory", J. Phys. D: Appl. Phys. 46, 264001 (2013).

[41] P. Roushan, J. Seo, C.V. Parker, Y.S. Hor, D. Hsieh, D. Qian, A. Richardella, M.Z. Hasan, R.J. Cava, and A. Yazdani, "Topological Surface States Protected from Backscattering by Chiral Spin Texture", Nature (London) 460, 1106 (2009).

[42] T. Zhang, P. Cheng, X. Chen, J.-F. Jia, X. Ma, K. He, L. Wang, H. Zhang, X. Dai, Z. Fang, X. Xie, and Q.-K. Xue, "Experimental Demonstration of Topological Surface States Protected by Time-Reversal Symmetry", Phys. Rev. Lett. 103, 266803 (2009).

[43] J.E. Moore, "The Birth of Topological Insulators", Nature, 464, 194 (2010).

[44] A.V. Semichaevsky, R.S. Goldman, and H.T. Johnson, "Linking Computational and Experimental Studies of III-V Quantum Dots for Optoelectronics and Photovoltaics", JOM, 63, 20 (2011).

[45] "Dilute III-V Nitride Semiconductors and Material Systems", edited by A. Erol (Springer, Berlin, Heidelberg, 2008).

[46] J. Wu, W. Shan, and W. Walukiewicz, "Band Anticrossing in Highly Mismatched III-V Semiconductor Alloys", Semicond. Sci. Technol. 17, 860 (2002).

[47] A.R. Denton and N.W. Ashcroft, "Vegard's Law", Phys. Rev. B. 43, 3161 (1991).

[48] R. Hull and J.C. Bean, "Misfit Dislocations in Lattice-mismatched Epitaxial Films", Critical Reviews in Solid State and Materials Sciences. 17, 507 (1992).

[49] T. Anan, M. Yamada, K. Tokutome, S. Sugou, K. Nishi, and A. Kamei, "Room-temperature Pulsed Operation of GaAsSb/GaAs Vertical-cavity Surface-emitting Lasers", Electron. Lett. 35, 903 (1999).

[50] A.D. Prins, D.J. Dunstan, J.D. Lambkin, E.P. O'Reilly, A.R. Adams, R. Pritchard, W.S. Truscott, and K.E. Singer, "Evidence of Type-I Band Offsets in Strained $GaAs_{1-x}Sb_x$/GaAs Quantum Wells from High-pressure Photoluminescence", Phys. Rev. B47, 2191 (1993).

[51] G. Ji, S. Agarwala, D. Huang, J. Chyi, and H. Morkoc, "Band Lineup in $GaAs_{1-x}Sb_x$/ GaAs Strained-layer Multiple Quantum Wells Grown by Molecular-beam Epitaxy", Phys. Rev. B. 38, 10571 (1988).

[52] M. Peter, K. Winkler, M. Maier, N. Herres, J. Wagner, and K. H.Bachem, "Realization and Modeling of a Pseudomorphic ($GaAs_{1-x}Sb_x$–$In_yGa_{1-y}As$)/ GaAs Bilayer-quantum Well", Appl. Phys. Lett. 67, 2639 (1995).

[53] G. Liu, S.-L. Chuang, and S.-H. Park, "Optical Gain of Strained GaAsSb/GaAs Quantum-well Lasers: A Self-consistent Approach", J. Appl. Phys. 88, 5554 (2000).

[54] M. Dinu, J. E. Cunningham, F. Quochi, and J. Shah, "Optical Properties of Strained Antimonide-based Heterostructures", J. Appl. Phys. 94, 1506 (2003).

[55] R. Teissier, D. Sicault, J. C. Harmand, G. Ungaro, G. Le Roux,and L. Largeau, "Temperature-dependent Valence Band Offset and Band-gap Energies of pPseudomorphic GaAsSb on GaAs", J. Appl. Phys. 89, 5473 (2001).

[56] Gh. Dumitras and H. Riechert, "Determination of Band Offsets in Semiconductor Quantum Well Structures using Surface Photovoltage", J. Appl. Phys. 94, 3955 (2003).

[57] X.D. Luo, C.Y. Hu, Z.Y. Xu, H.L. Luo, Y.Q. Wang, J.N. Wang, and W.K. Ge, "Selectively Excited Photoluminescence of $GaAs_{1-x}Sb_x$/GaAs Single Quantum Wells", Appl. Phys. Lett. 81, 3795 (2002).

[58] W.K. Bae, S. Brovelli and V.I. Klimov, "Spectroscopic Insights into the Performance of Quantum Dot Light-emitting Diodes", MRS Bulletin. 38, 721 (2013).

[59] A.D. Stiff-Roberts, "Quantum Dot Infrared Photodetectors: Advantages, Challenges, and Future Research Directions", IEE-NANO, 444 (2009).

[60] Y.L. Chen, J.G. Analytis, J.H. Chu, Z.K. Liu, S.K. Mo, X.L. Qi, H.J. Zhang, D.H. Lu, X. Dai, Z. Fang, S.C. Zhang, I.R. Fisher, Z. Hussain, and Z.X. Shen, "Experimental

Realization of a Three-dimensional Topological Insulator, Bi_2Te_3", Science 325, 178 (2009).

[61] D.X. Qu, Y.S. Hor, J. Xiong, R.J. Cava, and N.P. Ong, "Quantum Oscillations and Hall Anomaly of Surface States in the Topological Insulator Bi_2Te_3", Science 329, 5993 (2010).

[62] K. Hoefer, C. Becker, D. Rata, J. Swanson, P. Thalmeier, and L.H. Tjeng, "Intrinsic Conduction through Topological Surface States of Insulating Bi_2Te_3 Epitaxial Thin Films", PNAS 111, 14979 (2014).

[63] W. Liu, H. Chi, J.C. Walrath, A.S. Chang, V.A. Stoica, L. Endicott, X. Tang, R.S. Goldman, and C. Uher, "Origins of Enhanced Thermoelectric Power Factor in Topologically Insulating $Bi_{0.64}Sb_{1.36}Te_3$ Thin Films", Appl. Phys. Lett. 108, 043902 (2016).

[64] Y. Xu, Z.X. Gan, and S.C. Zhang, "Enhanced Thermoelectric Performance and Anomalous Seebeck Effects in Topological Insulators", Phys. Rev. Lett. 112, 226801 (2014).

[65] D.J. Singh, "Doping-dependent Thermopower of PbTe from Boltzmann Transport Calculations", Phys. Rev. B 81, 195217 (2010).

[66] J.S. Zhang, X. Feng, Y. Xu, M.H. Guo, Z.C. Zhang, Y.B. Ou, Y. Feng, K. Li, H.J. Zhang, L.L. Wang, X. Chen, Z.X. Gan, S.C. Zhang, K. He, X.C. Ma, Q.K. Xue, and Y.Y. Wang, "Disentangling the Magnetoelectric and Thermoelectric Transport in Topological Insulator Thin Films", Phys. Rev. B 91, 075431 (2015).

[67] J.S. Zhang, C.Z Zhu, Z.C. Zhang, J. Wen, X. Feng, K. Li, M.H. Liu, K. He, L.L. Wang, X. Chen, Q.K. Xue, X.C. Ma, and Y.Y. Wang, "Band Structure Engineering in $(Bi_{1-x}Sb_x)_2Te_3$ Ternary Topological Insulators", Nature Commun. 2, 574 (2011).

[68] X. He, H. Li, L. Chen, and K. Wu, "Substitution-induced Spin-splitted Surface States in Topological Insulator $(Bi_{1-x}Sb_x)_2Te_3$", Sci. Rep. 5, 8830 (2015).

[69] B.P. Gorman, A.G. Norman, and Y. Yan "Atom Probe Analysis of III–V and Si-Based Semiconductor Photovoltaic Structures", Microsc. Microanal. 13, 493 (2007).

[70]A.S. Chang and L.J. Lauhon, "Atom Probe Tomography of Nanoscale Architectures in Functional Materials for Electronic and Photonic Applications", 22, 171 (2018).

[71] E. Di Russo. "Study of the Physical Mechanisms Leading to Compositional Biases in Atom Probe Tomography of Semiconductors", Ph.D. Thesis, Normandie Université, 2018.

[72] R. Cuduvally, R.J.H. Morris, P. Ferrari, J. Bogdanowicz, C. Fleischmann, D. Melkonyan, and W. Vandervorst, "Potential Sources of Compositional Inaccuracy in the Atom Probe Tomography of $In_xGa_{1-x}As$", Ultramicroscopy, 210, 112918 (2020).

[73] S. Birner, S. Hackenbuchner, M. Sabathil, G. Zangler, J. A. Majewski, T. Andlauer, T. Zibold, R. Morschl, A. Trellakis, and P. Vogl, "Modeling of Semiconductor Nanostructures with nextnano^3", Acta Phys. Pol. A 110, 111 (2006).

[74] T. Jen, "Ion Beam Analysis of Solute Incorporation in GaAsN and GaAsNBi Alloys", Ph.D. Thesis, University of Michigan, 2016, pp. 106-112.

[75] J. Walrath, "Probing the Band Structure and Local Electronic Properties of Low-Dimensional Semiconductor Structures", Ph.D. Thesis, University of Michigan, 2017, pp. 51-72.

[76] C.-H. Chiou, P.-H. Wu, S.-F. Chen, I.-L. Chen, J.-T. Hsu, A.-Y. Tzeng, and C.-H. Wu, "Solar Cell with Superlattice Structure and Fabricating Method Thereof", US20070151595 A1 (5 July 2007).

Chapter 2

Experimental Procedures

2.1 Overview

This chapter describes the experimental procedures used for the fabrication of the semiconductor thin films examined in this thesis, as well as the analysis techniques used for their structural, electronic, and optical characterizations. All alloys were grown by molecular-beam epitaxy (MBE) on GaAs (001) or sapphire (0001) substrates. For the multi-layered GaSb/GaAs heterostructures, scanning transmission electron microscopy (STEM) was used to examine the nanoscale structure and photoluminescence (PL) spectroscopy was used to characterize their optical properties. Local electrode atom probe (LEAP) tomography was used to measure the local compositions within GaAs, GaAsNBi, multi-layered InAs/GaAs QDs, and multi-layered GaSb/GaAs films. Band energies (i.e., valence band energies, conduction band energies, and confined energies) and carrier concentrations were calculated using a self-consistent Schrödinger-Poisson solver within nextnano,[1] a commercial software package. Finally, scanning tunneling microscopy/spectroscopy (STM/STS) and magneto-transport measurements were used to examine the surface and bulk conduction within BiSbTe alloys.

2.2 Molecular-beam epitaxy

Molecular-beam epitaxy (MBE) is a vapor deposition technique that enables growth of high-quality epitaxial films and heterostructures.[2-6] The sublimation of solid sources materials produces molecular beams that interact with a heated single-crystalline substrate, depositing atoms or molecules on the growth surface to form epitaxial films. Deposition for the samples discussed in this dissertation was performed in ultra-high vacuum (~10^{-9} Torr) conditions. Depositions were controlled the opening and closing of shutters of effusion cells that contain the source materials. Atomic compositions of the deposited epitaxial films were controlled by choosing temperatures based upon beam flux readings.[5]

GaAsNBi alloys and InAs/GaAs QD superlattices described in Chapter 3 were grown in the Goldman MBE lab at the University of Michigan by the author, Dr. Tim Jen, and Dr. Davide Del Gaudio. MBE-grown GaSb/GaAs QDs described in Chapter 4 were grown by Professor Ganesh Balakrishnan's lab at the University of New Mexico. Finally, BiSbTe thin films described in Chapter 5 were grown by Dr. V.A. Stoica, Dr. W. Lin, and Mr. L. Endicott in Professor Citrad Uher's lab in collaboration with Professor Roy Clark at the University of Michigan. Sample structure and growth procedure details are given in the respective chapters.

2.3 Transmission electron microscopy (TEM)

The nanoscale structure within GaSb/GaAs QDs, described in Chapter 4, was examined using a transmission electron microscope (TEM). In a TEM, a beam of high-energy electrons (200-300 keV) illuminates a very thin specimen (<100 nm) and is

projected onto a screen or a camera generating an image of the specimen, as shown in Figure 2.1(a). Most of the electrons are transmitted through the specimen without being scattered to produce bright-field images, and another part of the electrons are diffracted out of axis by interaction with the specimen, generating dark-field images. Contrast from differences in film thickness, atomic number, phases, and crystal orientation allow for the observation of specimen features, such as chemical compositions, dislocations and nanostructures. In this thesis, we used a double C_s-corrected JEOL 3100R05 Cold-FEG TEM at $(MC)^2$, operating at 300 kV to investigate GaSb/GaAs nanostructure sizes and shapes. TEM analyses were performed using. All specimens were prepared and imaged by the author.

2.3.1 HAADF-STEM

The JEOL 3100R05 combines both TEM and scanning transmission electron microscope (STEM) modes. In STEM, the electron beam is highly focused and scans the surface of the specimen. Electrons that have not been scattered or have been scattered inelastically at very small angles (milliradians or less) are collected by the BF detector, as shown in Figure 2.1(b), and used to generate STEM bright-field images. STEM offers significant benefits in dark-field mode using a unique imaging mode called high-angle annular dark field (HAADF), where only electrons scattered at high angles (>30 milliradians) are collected using an annular detector, also shown in Figure 2.1(b). STEM images are therefore formed by elastically scattered electrons that have passed very close to the atomic nuclei of the specimen. The signal intensity is proportional to the square of the atomic number Z^2, providing important information in the images about the chemical

nature of the specimen. In this work, STEM is used to differentiate Sb-containing regions from GaAs regions in multi-layered GaSb/GaAs QD specimens.

2.3.2 Specimen preparation for cross-sectional STEM

For the structural analysis of the GaSb/GaAs heterostructures, cross-section STEM specimens normal to the [110] and [1$\bar{1}$0] directions were prepared using conventional mechanical grinding or polishing to <20μm, followed by ion milling using a Gatan Precision Ion Polishing system as described in Ref 7.[7] For mechanical polishing, two cleaved sample pieces were first glued together with their (001) epilayer surfaces facing inward using M-Bond 610 adhesive. This "sandwiched" specimen was subsequently thinned along both <110> directions using 800, 1000, and finally 1200 grit silicon carbide abrasive grinding paper. The specimen was glued to a PELCO (1 x 2) mm titanium slot grid and then milled with Ar^+ ions, using a Gatan Precision Ion Polishing system with an accelerating voltage of 2 kV and incident angle of 2º for approximately 30 minutes to 1 hour. The final polishing step was performed at 1.0 kV and 0.5º for 5 minutes.

2.4 Local electrode atom probe (LEAP) tomography

For local electrode atom probe (LEAP) tomography, a conical-shaped specimen is sequentially evaporated to generate a three-dimensional map of local compositions within the specimen volume.[8,9] Figure 2.2 shows a general schematic of the experimental setup for LEAP analysis. A direct current (DC) voltage is applied between the specimen and electrode positioned <100 μm from the apex of the conical-shaped specimen. Atomic ionization and ion evaporation from the apex of the specimen are then triggered by electric

or laser pulses. Thus, positively charged ions (m^{n+}) are generated and accelerated towards a position-sensitive detector. Thus, the chemical identity and original position of each ion is determined by its time-of-flight (TOF) and mass-to-charge ratio (m/z). This sequence is repeated multiple times until the specimen fractures, or the experiment is ended by the user. For this thesis, we used the Cameca LEAP 4000X and 5000X to investigate the atomic arrangements of GaAs, GaAsNBi, InAs/GaAs quantum dots and GaSb/GaAs multilayers. For all experiments, we fix the detection rate and allow the DC voltage to vary to maintain that detection rate.

Reconstruction algorithms within Cameca's Integrated Visualization Analysis Software (IVAS) suite were then used to render 3D reconstructions, enabling 3D images of the atoms within the specimens. GaAs and GaAsNBi LEAP experiments, 3D reconstructions, and analyses were performed by the author, Dr. Tim Jen, and Mr. Tao-Yu Huang. LEAP experiments of InAs/GaAs quantum dots were performed by Dr. Jenna Walrath; 3D reconstructions and analyses were performed by Ms. Grace Fedele and the author. LEAP experiments of GaSb/GaAs multilayers were performed by Mr. Eric Zech; 3D reconstructions, and analyses were performed by author.[10] Detailed descriptions about reconstruction parameters and data analyses are presented in Appendix B and C, respectively.

2.4.1 Specimen preparation for LEAP

A FEI Helios secondary electron microscope (SEM), equipped with a focused-ion-beam (FIB), is used to prepare LEAP specimens. In general, sample wafers (~ 2 cm x 2 cm) were loaded onto the SEM stage such that the growth direction (001) is parallel to the

SEM beam. For this system, the FIB ion beam is tilted at an angle of 52º with respect to the sample surface and stage. For lift-out, a portion of the epilayer was cut, 'lifted out', and transferred onto a microtip array, which is a prefabricated silicon wafer with ~100 μm tall Si posts with an end diameter of 2 μm. After placement of the specimen onto the Si post, the sample is shaped into a needle-shape using the FIB. A detailed description of the specimen preparation procedures is presented in Appendix A.

2.4.2 Pulsed-voltage versus pulsed-laser mode

The Cameca LEAP 4000x and 5000x offer two modes of evaporation – pulsed-voltage-assisted and pulsed-laser-assisted evaporation, both of which were used in the analysis of III-V materials studied in this dissertation. In pulsed-voltage (pulsed-laser) mode, field evaporation is attained by a combination of an applied standing voltage and a pulsed voltage (laser). Details on evaporation differences between voltage and laser modes can be found in Ref. 11.[11] For experiments, LEAP specimens (or "tips") were immediately loaded into a UHV (~10^{-10} Torr) buffer chamber after preparation to avoid surface oxidation, minimizing the chances of premature tip-fracture during the experiment. After ~8 hours of pumping on the buffer chamber, samples were transferred to the analysis chamber (~10^{-11} Torr), and the sample stage temperature was lowered to 25K for experimental analysis.

For the multi-layered GaSb/GaAs, specimens were analyzed in pulsed-voltage mode. In this mode, field evaporation was attained by a combination of a DC standing voltage and a pulsed voltage of ~20% of the standing voltage acting on a <100 nm specimen placed very close to the aperture of the local electrode, as shown in Figure 2.3. The purpose

of the standing voltage is to induce applied electric field, which reduces the threshold required for field evaporation of ions towards the remote detector. The voltage pulses on top of the standing DC voltage induce ion evaporation from the specimen.

For the GaAsNBi alloys, specimens were analyzed in laser-pulsed mode. In this mode, ion evaporation was induced by an ultrafast-pulsed (picosecond or femtosecond) laser focused on the apex of the specimen, along with the standing DC voltage. In ideal circumstances, individual atoms of all species are ionized and evaporated sequentially, enabling sequential detection at the remote detector. The main advantage of using laser-assisted mode for evaporating nonconductive materials, such as semiconductors, is that the laser enhances field evaporation without significant heating of the specimen, leading to better resolution of atomic masses.[12]

2.5 Photoluminescence

Photoluminescence (PL) measurements were used to obtain the optical signatures of specific nanostructures (i.e., wetting layers, quantum dots, and quantum-dot-rings) within GaSb/GaAs multilayers. The PL spectra were collected at 20 K in a closed-cycle helium cryostat, using a 10 mW HeNe laser operating at 633 nm. A 250 μm slit, single channel InGaAs detector was used for collection. PL measurements were performed by Dr. Stephen Clark in Professor Ganesh Balakrishnan's group at the University of New Mexico.[13]

2.6 NextNano band structure simulations

Nextnano[1,14,15] is a commercially available semiconductor device simulation software that allows us to simultaneously solve the Schrodinger and Poisson equations in order compute the electronic band structures for quantum confined heterostructures. For the simulations, the user first builds a model within the software by first specifying the geometry, materials, the contact bias, and other information needed to describe the physical system. The user defines material parameters (i.e., lattice constant, band gap energy, mobilities, piezoelectric charges, etc.) within the nextnano materials database using up-to-date values from literature reports. After the geometry and material parameters are defined, the nextnano Schrödinger-Poisson solver is used to compute the band structure.

For calculating the band energies, we used nextnano's Schrödinger-Poisson solver based on the 8-band $\mathbf{k}\cdot\mathbf{p}$ approximation.[16] First, strain was calculated in the continuum elasticity approach with elastic constants from Vurgaftman, et al.[17] Conduction and valence band edges were subsequently obtained using band offsets from model-solid theory[18] and deformation potential theory. Finally, the confined energies were determined by solving the Schrödinger and Poisson equations, self-consistently, as described elsewhere.[1,14,15]

In general, the electrostatic potential, V(r), is computed using Poisson's equation:

$$\nabla^2 V(r) = \frac{\rho_f(r)}{\varepsilon_o \varepsilon_r(r)} \tag{2.1}$$

where ρ_f is the spatially varying charge, ε_o is the permittivity of free space, and $\varepsilon_r$is the spatially varying permittivity of the semiconductor material assumed to follow the rule of mixtures. The electrostatic potential and kinetic energies are then used for calculating electron and hole energies, as described by the Schrödinger equation:

$$E\psi = \frac{\hbar}{2m}\nabla^2\psi + V(r)\psi \tag{2.2}$$

The advantage of using nextnano in our work is that experimental data can be used as input, allowing for more realistic modeling of the electronic structure. The nextnano simulations presented in this dissertation were performed by the author and Ms. Grace Fedele. The parameters, including the input text file, are presented in Appendix C.

2.7 Scanning tunneling microscopy (STM)

Scanning tunneling microscopy (STM) is an imaging technique that relies on quantum tunneling and the availability of high precision piezo electrics to scan over sub-nanometer length scales. When a metallic tip is brought very near to the surface of a material, an applied bias facilitates the tunneling of electrons through the vacuum between the tip and the surface of the sample.[19] All STM imaging was performed in constant-current mode with setpoints typically of 100-300 pA. The tip height is varied as it moves across the surface to maintain the setpoint current. Constant-current images is primarily due to variations in the electronic properties of the sample.

For these studies, we use sample holders designed for both plan-view and cross-sectional imaging.[20] Figure 2.4 illustrates the orientation of a sample and tip for plan-view and cross-sectional STM on an III-V heterostructure sample. For plan-view STM, the III-V [001] growth surface is imaged directly. For XSTM, a cross-section of the sample is prepared by cleaving it in ultra-high vacuum (UHV) to expose an atomically flat [110] surface, as also illustrated in Figure 2.4.

STM experiments presented in this dissertation were carried out using an Omicron Variable Temperature Scanning Tunneling Microscope (VT-STM) system. A detailed description of the Omicron VT-STM system can be found in Section 6.2.3 of V. Dasika's

Ph.D. thesis.[20] STM imaging of the Bi_2Te_3-Sb_2Te_3 films discussed in Chapter 5 were performed by Dr. Jenna Walrath and the author. STM images of the GaSb/GaAs QD and GaAsNBi/GaAs superlattices discussed in Chapter 6 were performed by the author.

2.7.1 Sample preparation for XSTM

To prepare samples for XSTM, sample pieces were thinned and polished using the Logitech PM5 Lapper at the Lurie Nanofabrication Facility (LNF) in the University of Michigan. Approximately ¼ of a 2" wafer was thinned to ~80 μm thick by lapping against a non-grooved glass plate, with a 3 μm Al_2O_3-water solution as an abrasive. For uniform lapping or thinning of the wafer, the sample was rotated at a speed of 25 rpm, while a constant pressure of 2 N/m^2 was applied to the rotating sample against the Al_2O_3 particles.

The thinned wafer was then removed from the lapping apparatus and cut into ~15 mm x 2 mm rectangular pieces using a diamond scriber. Finally, a small, shallow scribe mark was made on the growth surface along the [110] direction, approximately 5 to 7 mm away from one of the edges. For all cases, the scribe mark length was 1/3 of the sample width.

Scribed samples were then mounted, held by rectangular jaws, in a cross-sectional sample holder, such that the scribe marks were parallel to the edge of the jaw. The epilayer sides of the samples were loaded facing up, with the scribed end resting directly on the back of the sample holder. Schematic photos are shown in Section 6.2.3 of the Ph.D. thesis of Dr. V. Dasika.[20] Once the samples were mounted onto the sample holder, the sample was transferred to the UHV STM chamber via a load lock. The ion gauge is switched off ~12 hours before an experiment begins to reduce thermal drift of the tip. For XSTM, on

the day of the experiment, the samples are cleaved in-situ by mechanically lowering a 60° diamond tip into contact to the edge of the sample to reveal a nearly atomically flat surface. The sample surface is examined using a telescope with a magnification of 40x (Omicron STM system), and the tip is "auto-approached" to the sample. For approaching the sample with the tip, an electrical feedback loop is activated, and the biased tip approaches the sample's surface in a controlled manner until a tunneling current is detected. More details on the procedure for tip approach in the VT-STM are described in Section 2.6.5 of A.S. Chang's PhD thesis.[21]

2.7.2 STM tip preparation

All the STM and STS experiments described in this dissertation were performed with commercially available PtIr or W STM tips from Bruker.[22,23] PtIr or W tips are used due to the relatively small energy required to overcome their work functions for electron tunneling.[24] The STM tips were cleaned *in situ* by electron bombardment from a heated molybdenum filament.[25] Since this procedure increases the STM chamber pressure, tips for an experiment are cleaned *in situ* at least 12 hours before an experiment, but no longer than 24 hours prior to an experiment, to prevent tip contamination. Immediately after tip cleaning, the tungsten sublimation pump was run for 1 minute at 35.5 Amps to lower the chamber pressure. The tip cleaning procedure for the VT-STM is described in Section 2.6.4 of A.S. Chang's PhD thesis.[21]

2.8 Scanning tunneling spectroscopy (STS)

In addition to STM imaging we use scanning tunneling spectroscopy (STS) to experimentally probe the local band structure. For STS measurements, the feedback loop is deactivated while a bias voltage swept, typically from -3 V to +3 V, promoting the tunneling of electrons (with varying energies) between the tip and the sample. Figure 2.5(a) shows an example of the process of electrons tunneling from the valence band through vacuum to the metallic tip at negative voltages. At positive voltages, electrons tunnel from the tip into empty higher energy states of GaAs (i.e., the GaAs conduction band). During this voltage sweep, the current I(V) produced by the tunneling electrons is measured, as exemplified in Figure 2.5(b). In addition, a lock-in amplifier is used to modulate the applied bias and measure the differential conductance, dI(V)/dV, which is related to the local density of states, as described in Section 2.4.1 of the thesis of V. Dasika.[20] Following collection of spectra for the current, I(V), and differential conductance, dI(V)/dV, an analysis approach is used to determine the band edges and effective band gaps,[26] as described in Appendix C and is based on earlier studies.[27]

2.9 Magneto-transport measurements

To obtain information about the free carrier concentrations and mobilities in the Bi_2Te_3-Sb_2Te_3 films, low-temperature transport measurements were performed under varying magnetic fields (-14 to 14 T) using the Quantum Design DynaCool Physical Property Measurement System (PPMS) in the Physics Department at the University of Michigan. For these measurements, samples (~2 cm x 2 cm) were placed on the Electrical Transport Option (ETO) puck, a standard Quantum Design sample holder and wired in a four-terminal geometry using indium for Ohmic contacts, as shown in Figure 2.6. Typical

contact resistances ranged from 200 Ω to 1 kΩ for our films. In the four-terminal geometry (4-wire mode), two leads pass a current through the sample and two separate leads measure the potential drop across a section of the sample, as illustrated in Figure 2.6.

The ETO puck containing the sample was subsequently loaded into the PPMS and cooled to 4K for analysis. The PPMS uses liquid He-4 for cooling both the sample chamber and the superconducting magnet and a cryopump to maintain a vacuum $<10^{-4}$ Torr. A DC current of 5μA was sent through the sample using a lock-in-amplifier with a voltage output of 5 V and 1 MΩ resistor. Two Stanford SR830 lock-in amplifiers were used to simultaneously measure the longitudinal (magnetoresistance) and transverse (Hall) voltages, as shown in Figure 2.6. Each lock-in amplifier permits AC measurements of both the in-phase (resistance) and out-of-phase (capacitance) components of impedance. In all cases, the magnitude of the out-of-phase component was kept less than 1/10 the magnitude of the in-phase component, minimizing measurement noise (such as parasitic capacitance in the wires) in the measured signal.

Figure 2.7 shows an example of magnetoresistance (R_{xx}) and Hall resistance (R_{xy}) data. Data were geometrically corrected for samples where the contacts were not perfectly symmetrical. Furthermore, multicarrier conduction was examined using multicarrier fits assuming a two-channel conduction model,[28,29] as described in Appendix C. The magneto-transport measurements were performed by the author.

2.10 Figures

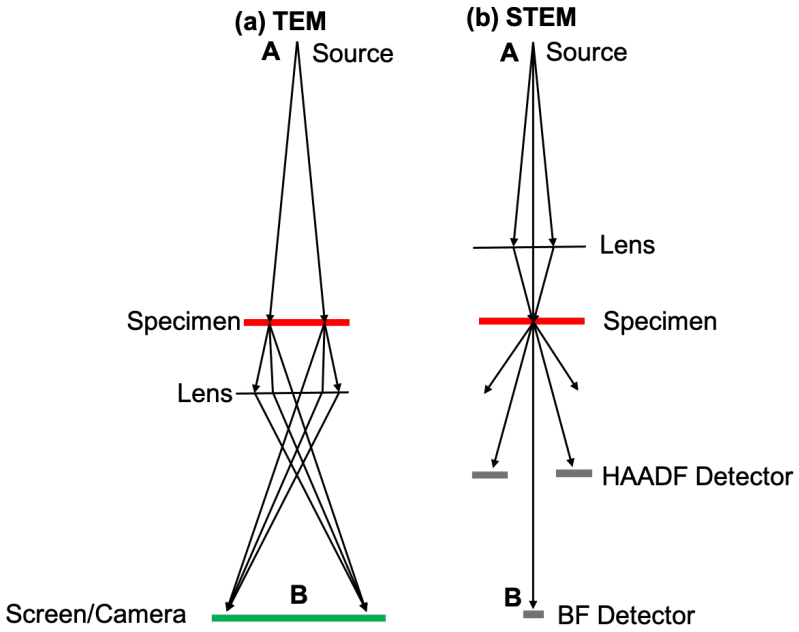

Figure 2.1 Simplified schematic of (a) TEM versus (b) STEM mode. In TEM mode, parallel electron beams are focused perpendicular to the specimen plane. In STEM mode, the beam is focused and condensed into a focal point on the specimen. While TEM uses electrons transmitted through the specimen to create an image, STEM creates an image by detecting reflected or knocked-off electrons. For STEM images, a JEOL HAADF detector was used to collect electrons that elastically scattered at large angles (59–200 milliradians).

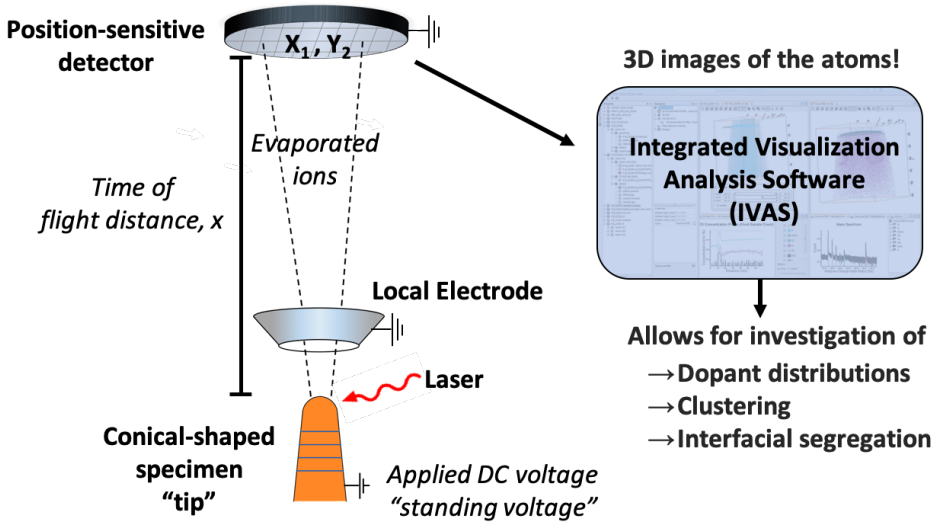

Figure 2.2 Illustration of the experimental setup and reconstruction analysis process for local electrode atom probe (LEAP) tomography. Atoms are ionized and evaporated from a conical-shaped specimen (also called "tip"). For laser-pulsed mode, an ultrafast laser is used to assist the evaporation of atoms from the specimen. For voltage-pulsed mode, a voltage pulse (at 20% of the standing DC voltage) is used to evaporate the ions. In both cases, the ion detection rate is fixed, and the DC voltage self-adjusts to maintain that detection rate. Evaporated ions are subsequently accelerated using a local electrode towards a position-sensitive detector. The time-of-flight and mass-to-charge data are used to determine the chemical identity and the original position of the evaporated ions. A reconstruction algorithm within Cameca's Integrated Visualization Analysis Software (IVAS) suite uses this information to render a surface that allows for the investigation of dopant distributions, clustering, and interfacial segregation for the specimen.

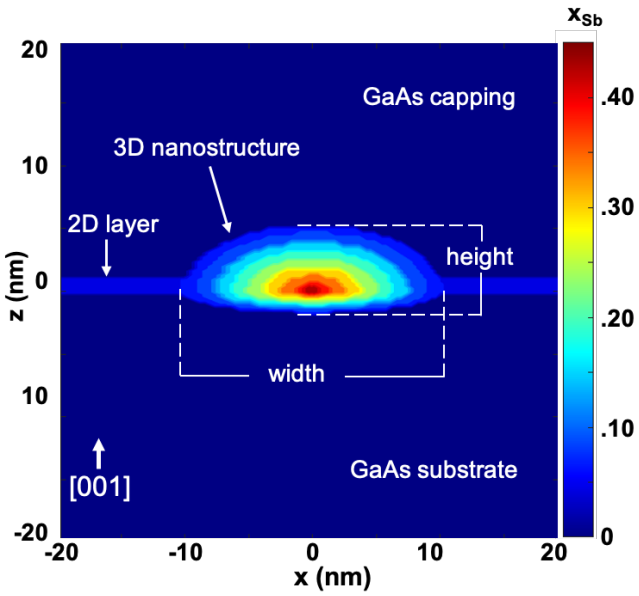

Figure 2.3 Representative x-z view of simulation region for the $GaAs_{1-x}Sb_x$ quantum dot (QD) embedded in GaAs with compositional gradient from local electrode atom probe (LEAP) and dimensions from scanning transmission electron microscopy (STEM).

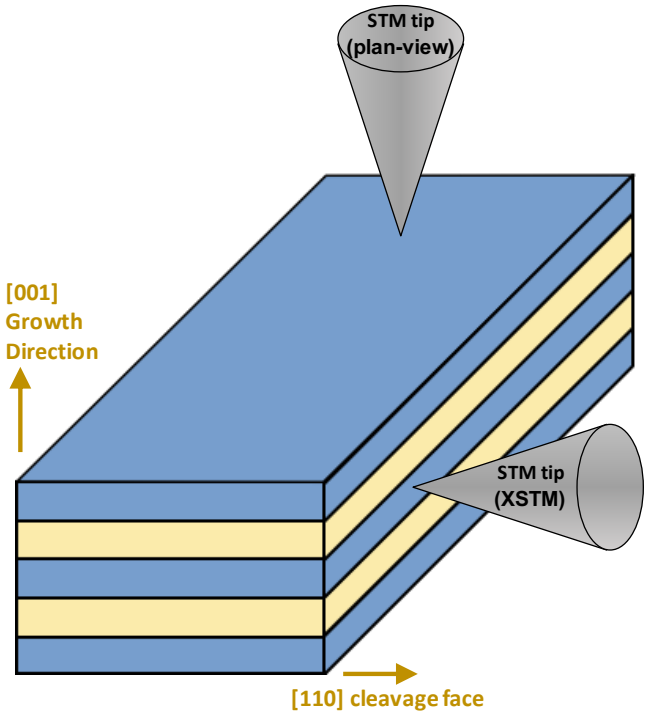

Figure 2.4 Schematic of plan-view and cross-sectional scanning tunneling microscopy (STM) applied to a III-V heterostructure. The STM tip is brought within a few angstroms of the [001] growth surface for plan-view imaging or the [110] cleaved surface for cross-sectional imaging. For flat cleaves over 100's of $(\mu m)^2$, true atomic resolution is possible over macroscopic length scales.

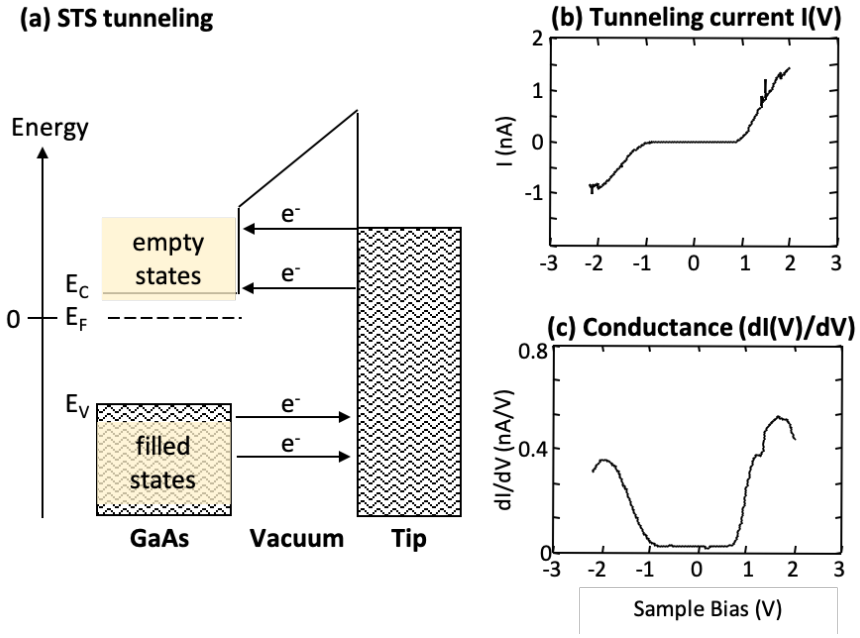

Figure 2.5 Schematic of (a) the tunneling process between energy states of a metallic tip and a GaAs sample for negative and positive applied voltages. At negative voltages, electrons tunnel from filled states in the GaAs valence band. At positive voltages, electrons tunnel from the tip to higher energy states within the GaAs conduction band. The (b) tunneling current and (c) differential conductance is measured simultaneously, allowing for determination of the local valence and conduction band edges, and thus the local effective band gap.

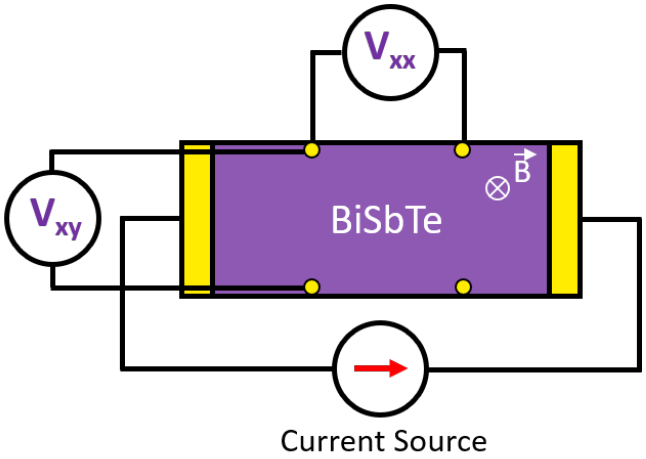

Figure 2.6 Schematic of 4-terminal setup for magnetoresistance (MR) and Hall resistance measurements. A current is passed through the sample using two leads, while two separate leads measure the potential drop parallel (V_{xx}) to the applied current for MR measurements or perpendicular (V_{xy}) to the applied current for Hall resistance measurements.

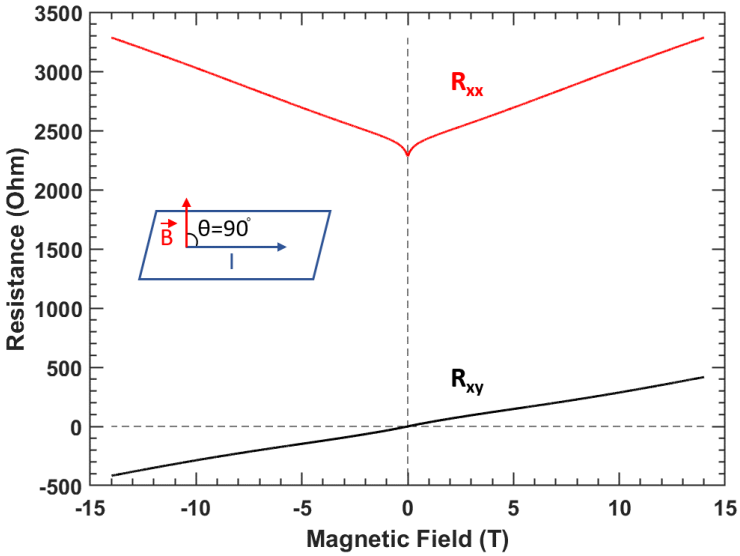

Figure 2.7 (a) Magnetoresistance (R_{xx}) and (b) Hall resistance (R_{xy}) data as a function of perpendicular magnetic field for an 18 nm $Bi_{0.64}Sb_{1.36}Te_3$ film.

2.11 References

[1] S. Birner, S. Hackenbuchner, M. Sabathil, G. Zangler, J. A. Majewski, T. Andlauer, T. Zibold, R. Morschl, A. Trellakis, and P. Vogl, "Modeling of Semiconductor Nanostructures with nextnano^3", Acta Phys. Pol. A 110, 111 (2006).

[2] A.Y. Cho and S. E. Stokowsk, "Molecular Beam Epitaxy and Optical Evaluation of $Al_xGa_{1-x}As$", Solid State Commun. 9, 565 (1971).

[3] M.A. Herman, W. Richter, and H. Sitter, "Epitaxy Physical Principles and Technical Implementation", (Springer, 2004).

[4] R.L. Field III, "Growth and Electronic Properties of GaAsN and GaAsBi Alloys", Ph.D. Thesis, University of Michigan, 2015, pp. 54, 107–108, 117.

[5] T. Jen, "Ion Beam Analysis of Solute Incorporation in GaAsN and GaAsNBi Alloys", Ph.D. Thesis, University of Michigan, 2016, p. 34.

[6] W. Liu, L. Endicott, V.A. Stoica, H. Chi, R. Clarke, and C. Uher, "High-quality Ultra-flat $BiSbTe_3$ Films Grown by MBE", J. Crys. Growth 410, 23 (2015).

[7] N. Fernández-Delgado, M. Herrera, M.F. Chisholm, M.A. Kamarudin, Q.D. Zhuang, M. Hayne, and S.I. Molina, "Atomic-column Scanning Transmission Electron Microscopy Analysis of Misfit Dislocations in GaSb/GaAs Quantum Dots", J. Mater. Sci.51, 7691 (2016).

[8] D. Blavette, F. Vurpillot, B. Deconihout, A. Menand, "Atom probe tomography: 3D Imaging at the Atomic level", in: F.A. Lasagni, A.F. Lasagni (Eds.), Fabrication and Characterization in the Micro-Nano Range: New Trends for Two and Three Dimensional Structures, Springer, Berlin, Vol. 10, 2011, pp. 201–222.

[9] D.N. Seidman, K. Stiller, "An Atom-Probe Tomography Primer", MRS Bull. 34, 717 (2009).

[10] C. Greenhill, A.S. Chang, E.S. Zech, S. Clark, G. Balakrishnan, and R.S. Goldman, "Influence of Quantum Dot Morphology on the Optical Properties of GaSb/GaAs Multilayers", Appl. Phys. Lett. 116, 252107 (2020).

[11] D.J. Larson, T.J. Prosa, R.M. Ulfig, B.P. Geiser, and Th.F. Kelly, "Local Electrode Atom Probe Tomography", Springer, New York, 2013, pp. 89–105.

[12] B. Gault, F. Vurpillot, A. Vella, M. Gilbert, A. Menand, D. Blavette, and B. Deconihout, "Design of a Femtosecond Laser Assisted Tomographic Atom Probe", Rev. Sci. Instrum. 77, 043705 (2006).

[13] G. Balakrishnan, J. Tatebayashi, A. Khoshakhlagh, S.H. Huang, A. Jallipalli, L.R. Dawson, and D.L. Huffaker, "III/V Ratio Based Selectivity Between Strained Stranki-Krastanov and Strain-free GaSb Quantum Dots on GaAs", Appl. Phys. Lett. 89, 161104 (2006).

[14] S. Birner, T. Zibold, T. Andlauer, T. Kubis, M. Sabathil, A. Trellakis, and P. Vogl, "nextnano: General Purpose 3-D Simulations", IEEE Trans. Electron Devices. 54, 2137 (2007).

[15] A. Trellakis, T. Zibold, T. Andlauer, S. Birner, R. K. Smith, R. Morschl, and P. Vogl, "The 3D Nanometer Device Project nextnano: Concepts, Methods, Results", J. Comput. Electron. 5, 285 (2006).

[16] M.J. Deen and P.K. Basu, "Silicon Photonics: Fundamentals and Devices, Appendix A: k.p Methods", John Wiley & Sons Ltd, 2012, pp. 403–420.

[17] I. Vurgaftman, J. R. Meyer, and L. R. Ram-Mohan, "Band parameters for III-V Compound Semiconductors and their Alloys," J. Appl. Phys. 89, 5815 (2001).

[18] C.G. Van de Walle, "Band Lineups and Deformation Potentials in the Model-solid Theory", Phys. Rev. B: Condens. Matter 39, 1871, (1989).

[19] G. Binnig and H. Rohrer, "Scanning Tunneling Microscopy", Surf. Sci. 126, 236 (1983).

[20] V. Dasika, "Nanometer-Scale Structural and Electronic Properties of Low Dimensional Heterostructures", Ph.D. Thesis, University of Michigan, 2010, pp. 120–124.

[21] A.S. Chang, "Nanoscale Studies of Energy Band Gaps and Band Offsets in Compound Semiconductor Heterostructures", Ph.D. Thesis, University of Michigan, 2016.

[22] Bruker Model TT10 Etched Tungsten STM Probes S/N: 120613

[23] Bruker Model PT10 Cut Platinum/Iridium STM Probes S/N: 101713

[24] A.P. Wijnheljmer, J.K. Garleff, M.A. v.d. Heijden, and P.M. Koenraad, "Influence of the Tip Work Function on Scanning Tunneling Microscopy and Spectroscopy on Zinc Doped GaAs", J. Vac. Sci. Technol. B 28, 1086 (2010).

[25] B. Lita, "Nanometer-scale Studies of Interdiffusion and Segregation in Semiconductor Structures", Ph.D. Thesis, University of Michigan, 2001, pp. 24-27.

[26] R. Timm, H. Eisle, A. Lenz, L. Ivanova, V. Vosseburger, T. Warming, D. Bimberg, I. Farrer, D.A. Ritchie, and M. Dahne, "Confined States of Individual Type-II GaSb/GaAs Quantum Rings Studied by Cross-Sectional Scanning Tunneling Spectroscopy", Nano Lett. 10, 2972 (2010).

[27] J. Walrath, "Probing the Band Structure and Local Electronic Properties of Low-Dimensional Semiconductor Structures", Ph.D. Thesis, University of Michigan, 2017, pp. 51 – 72.

[28] J. Antoszewski, D.J. Seymour, and L. Faraone, "Magneto-Transport Characterization Using Quantitative Mobility-Spectrum Analysis", J. Elect. Mat., 24, 9 (1995).

[29] J.R. Meyer, C.A. Hoffman, J. Antoszewski, and L. Faraone, "Quantitative Mobility Spectrum Analysis of Multicarrier Conduction in Semiconductors", J. Appl. Phys. 81, 2 (1992).

Chapter 3

Examining Stoichiometry and Microstructure in III-V Alloys using Local Electrode Atom Probe Tomography

3.1 Overview

In this chapter, we present our investigations of stoichiometry and microstructure of III-V nanostructure alloys using local-electrode atom-probe tomography (LEAP), in conjunction with other methods, such as Rutherford Backscattering (RBS), high-resolution x-ray diffraction (HRXRD), and nextnano simulations.[1] To establish suitable conditions for LEAP of III-V alloys, we examine the influence of pulsed-voltage vs. pulsed-laser mode, and the respective laser energies on the apparent stoichiometry of GaAs. We use Kingham's post-ionization model, which assumes that atoms and/or molecules are ionized following evaporation, to estimate effective electric fields for each LEAP experiment. We then present the effective field dependence of the apparent III-V stoichiometry in GaAs, Si-doped GaAs, and GaAsNBi alloys, analyzing the atomic fractions for assignments of the 75 (150) Da peak to As^+ or As_2^{2+} (As_2^+ or As_4^{2+}). Finally, using the LEAP conditions identified for the nearest stoichiometry for GaAs, we apply this approach to investigate local N and Bi compositions in GaAsNBi alloys and local Si concentrations in the vicinity of Si-doped InAs/GaAs QD superlattices, building upon earlier studies by T. Jen[2] and J. Walrath.[3]

3.2 Background

Local-electrode atom-probe (LEAP) tomography is a powerful tool for investigating the 3D atomic distributions in a wide variety of semiconductor materials,[4] providing the highest available spatial resolution (sub ~0.3 nm) for chemical analysis.[5,6] For epitaxially-grown III-V materials, exact stoichiometric compositions are expected under standard growth conditions.[7-9] However, in the LEAP analysis of III-V compounds, evaporation field differences of the group III and group V species often promote the detection of one atom type more readily than the other.[10-13] For example, LEAP analysis of GaN,[14-17] GaAs,[18] GaSb,[19,20] and InGaAs[21] often leads to apparent excess of Group III species, depending on the effective field during evaporation. For example, Group III excesses (Group V deficits) often occur at low effective fields and are often related to clustering effects.[22,23] The presence of As clusters suggests possible overlaps in the mass spectra at m/z = 75 Da and m/z = 150 Da, which may be attributed to As^+/As_2^{2+} and As_2^+/As_4^{2+}, respectively, resulting in inaccuracies in the apparent stoichiometry. Since multiple inter-related origins for molecular evaporation/dissociation have been identified,[24-27] including effects due to laser heating and field anisotropy across the apex,[28] the apparent stoichiometry needs to be evaluated for each material system. Ideally, the stoichiometry is also validated via other experimental methods, such as ion beam analyses (IBA).

The influence of laser energy on molecular evaporation and the apparent stoichiometry of GaAs were previously examined in the thesis of T. Jen.[3] It was found that using lower laser energies (~1 pJ) improved the III-V stoichiometries and the apparent

alloy compositional uniformity, likely due to reduced molecular evaporation/detection. likely due to reduced effects of As-clustering at these energies. In this thesis, we build upon T. Jen's work by quantifying the effective field dependence of Ga and As fractions in GaAs and Si-doped GaAs (GaAs:Si) specimens examined with LEAP. Using experimental LEAP conditions identified to lead to nearly stoichiometric GaAs, we perform LEAP experiments on a series of GaAsNBi films. We compare the LEAP-determined Bi fractions with those from Rutherford backscattering (RBS),[29,30] and discuss implications for future GaAsNBi epitaxy.

We further use LEAP and Schrödinger-Poisson calculations to examine the effects of local Si distribution on the carrier concentrations in Si-doped InAs/GaAs quantum dots (QDs). Often, introducing heterocovalent dopants into QDs provide extra electrons and improve conductivity. However, the concentration of conducting electrons is often lower than the number of introduced Si atoms.[31,32] Due to limitations of local probing techniques,[33] both the extra electrons and their "parent" dopants are difficult to locate. In an earlier study of InAs/GaAs QDs using scanning thermoelectric microscopy (STheM), fewer electrons were observed within the QD than in the surrounding substrate, presumably due to the expulsion of the dopants from the QDs.[34,35] We use LEAP to examine the distribution of Si in the vicinity of InAs QDs and in the surrounding wetting layer. The 3D distribution of In, Ga, As, and Si concentrations determined using LEAP is used as input into Schrödinger-Poisson calculations to simulate effects of local Si distribution on the carrier concentrations using nextnano.[1] This work is an extension to studies of profiling local carrier concentration in InAs QDs, which is presented in the thesis of J. Walrath.[3]

Approaches that combine LEAP and electronic structure calculations can be applied to many III-V systems, an example of which is discussed in Chapter 4 using GaSb/GaAs QDs.

3.3 Methods

3.3.1 MBE growths

Films investigated in this work were grown on GaAs (001) substrates by molecular-beam epitaxy (MBE) using solid Ga, In, As, and/or Bi sources and a radio frequency nitrogen plasma source. Figure 3.1 shows the sample structures for the (a) GaAs, (b) GaAsNBi, and (c) Si-doped InAs/GaAs QD superlattice films. For the GaAs films, 1000 nm GaAs was grown at 580 ºC with an As/Ga beam equivalent pressure (BEP) ratio of ~ 20 and growth rate of 1 μm/hr. For the GaAsNBi and InAs QD films, as shown in Figure 3.1(a) and 1(b) respectively, an initial 500 nm thick GaAs buffer was grown at 580 ºC followed by a 3–5 minute anneal.[36] A range of 400 nm thick $GaAs_{1-x-y}N_xBi_y$ films were grown at 510 ± 15 ºC with As_4/Ga beam equivalent pressure (BEP) ratios of ~ 20 and growth rates of 1 μm/hr.[2] For the InAs/GaAs QD multilayers, five layers of 3 ML InAs were deposited at a rate of 0.1 ML/s, separated by 30 nm GaAs spacing layers and followed by a 50 nm GaAs capping layer. For all InAs layers, a constant Si cell temperature of 1250 ºC was maintained with a targeted free carrier concentration $n = 6.8 \times 10^{18}$ cm^{-3}.[37]

3.3.2 LEAP experimental procedures

In preparation for LEAP experiments, needle-shaped specimens were prepared via *in situ* lift-out, as described in Appendix A. LEAP experiments were subsequently

performed in pulsed-voltage or pulsed-laser mode at cryogenic temperatures (<25K) under ultra-high vacuum conditions (3.0 x 10^{-11} Torr). For the GaAs specimens, laser energies ranging from 0.25 to 25 pJ were used. For the GaAsNBi and GaAs:Si-containing specimens, LEAP was performed at constant laser energies of 0.25 and 1 pJ, respectively. We note that the GaAs:Si regions consist of the interlayers of the Si-doped InAs/GaAs QD superlattices. In all experiments, the ion detection rate is fixed at 0.5 ions/pulse, and the standing DC voltage (V_{DC}) self-adjusts to maintain that detection rate. Pulse frequencies ranged from 100 to 200 kHz. The raw data were reconstructed into 3D atomic maps using Cameca's IVAS™ commercial data reconstruction and analysis software, as described in Appendix B. For our voltage-mode analyses, Ga and As peaks were consistently labeled such that the widths are similar to those of the laser-pulsed measurements, excluding the tail regions of the peaks, as discussed in Appendix K of J. Walrath's thesis.[3]

For the GaAsNBi films, Bi fractions were determined using a combination of LEAP, HRXRC, and RBS measurements. For HRXRC measurements, a series of Δω scans were collected near the GaAs (004) reflections using $CuK_{\alpha 1}$ radiation. RBS was performed using a NEC tandem accelerator with a 4.46 MeV He^+ beam with the detector placed at 167º with respect to the incident beam. RBS was performed in non-channeling conditions achieved by fixing the sample at $\theta = 5º$ with respect to the [001] channeling direction and rocking $\varphi_x = \pm 4º$ during collection, as illustrated in Figure 2.11 of T. Jen's thesis.[2] RBS was analyzed using the simulation of nuclear reaction analysis (SIMNRA) code.[38] More details about HRXRC and RBS measurements are presented in the thesis of T. Jen.[2]

3.3.3 Estimating effective fields

In initial studies of GaAs, we varied the laser energies (0.25 – 25 pJ) to examine their effects on *apparent* Ga:As stoichiometry. As the laser energies decrease, a higher applied voltage (V_{DC}) is required to overcome the field threshold for LEAP evaporation, as indicated in the mass spectra plots in Figure 3.2. Therefore, it is not possible to discriminate between the role of the applied voltage and the laser energy without performing experiments where the applied voltage is kept constant while the detection rate is varied. For these experiments, the detection rates are kept constant at 0.5 ions/pulse.

Therefore, to map compositional trends among our LEAP runs, we use effective field estimations derived from charge-state metrics by Kingham's post-ionization model.[39] In short, Kingham's model uses the ratio of species at different charge states to estimate the effective surface field near the specimen's apex. The post-ionization model assumes that ions are evaporated only as singly-charged ions (X^+). Further ionization can occur within a few Angstroms of the tips surface, where additional electrons can tunnel back to the specimen's surface through quantum effects to produce multiply-charged states (X^{2+}, X^{3+}, etc.).

For GaAs, we consider fields derived from Ga^{2+}/Ga^+ (Ga-CSR) and As^{2+}/As^+ (As-CSR), as depicted in Figure 3.3. The method used for deriving effective fields is described in Appendix C. Our data in Figure 3.3 reveal that effective fields estimated by the Ga-CSR metric (17 to 23 V/nm) are lower than those derived by the As-CSR (20 to 22 V/nm) in GaAs, similar that of Di Russo, et al.[18] As shown in Table 3.1, unequal field estimations are common for semiconductor alloys, which confirms that effective fields should not be considered as the *actual* surface field but only as an estimate to facilitate comparisons of III-V evaporation behavior.

	III-V Compound(s)	E_{laser} (pJ)	E_{eff} (V/nm)
Diercks et al.[14]	GaN	0.01 – 10	--
Morris et al.[15]	GaN, AlGaN	0.01 – 10	Ga: 20–26
Our work	**GaAs, GaAsNBi**	**0.25 – 25**	**Ga: 18–23, As: 20–22**
Müller et al.[19]	GaSb	10 – 100	Ga: 16–20
Mancini[17]	GaN, InN, InAlN, etc.	700 – 2,000	Ga: 23–26, Al: 23–25
Di Russo et al.[40]	AlGaN	--	Ga: 25–27, Al: 24–25
Di Russo et al.[40]	InGaN	--	Ga: 23–25, In: 21–23
Di Russo et al.[18]	GaAs	30 – 63,300	Ga: 20–24, As: 21–24

Table 3.1 Laser energies and estimated fields (E_{eff}) from LEAP evaporations of some common III-V binary and ternary semiconductor alloys. The charge-state metrics from each experiment result in unequal field estimations when considering the different ions within the alloy. E_{eff} are derived using Kingham's post-ionization model.[39] We note that this is not an exhaustive list of LEAP experiments involving III-V's.

In general, effective field estimations can be done with any ion species. The charge-state metric chosen depends on characteristics of the dataset(s) and the specimen under investigation. For example, Müller et al.[20] used the Ga-CSR because no Ga-cluster ions were present in their LEAP evaporation of GaSb. Russo et al.[18] used the As-CSR because of the relatively large counting errors from the low detection of Ga^{2+}. On the other hand, the Ga-CSR is often used for Al-containing alloys (e.g., AlN, AlGaAs, AlGaN) because Al^{3+} is usually detected, and the simultaneous presence of Al^{3+} with other charge states, such as Al^{+} and Al^{2+}, is not compatible with Kingham statistics.[15,17,40] For our approach in analyzing LEAP datasets of GaAs, we find that increasing the laser energy results in significant reductions of both the 37.5 and 75 Da As peaks, as shown in the mass spectra in Figure 3.2. Both the 37.5 and 75 Da peaks are used in calculating the As-CSR. These reductions are most likely related to effects of clustering, which to date have not been

quantified for LEAP data. On the other hand, there is little to no laser energy dependence on the 69 and 71 Da Ga^+ peaks. Therefore, changes in Ga-CSR are primarily due to changes in Ga^{2+} counts, while changes in the As-CSR can be due to changes in counts at 37.5 Da, 75 Da, or both. Furthermore, using the As-CSR can be subject to error owing to the possibility of overlap between the As^+ and As_2^{2+} peaks at 75 Da. For these reasons, we estimate the effective field considering only the Ga-CSR. Using the Ga-CSR further allows for comparisons with many other III-V LEAP investigations that include Ga. More insight on representations of LEAP data as function of CSR metrics can be found in Section 2.8 of Mancini et al.[17] Figure 3.3 shows that the laser energy bears an inverse relationship with effective field. From henceforth, the terms "high energy" and "low field" may be interpreted as interchangeable.

3.4 Results and discussion

3.4.1 Apparent stoichiometry in GaAs

M/z overlaps may occur between As^+ and As_2^{2+} (75 Da) and As_2^+ and As_4^{2+} (150 Da), as indicated in Figure 3.2. Such overlap cannot be resolved since current detectors are not sensitive to kinetic energy of the impinging ions. Deconvolution methods involving the relative isotope abundances are often used for Sb- and In-containing alloys[20,41] when there are m/z overlaps, however, such methods cannot be applied here. Therefore, estimated compositions are assumed to consist of only the singly charged clusters (As^+/As^{2+}) by convention.[18,21] We examine the possible assignments of As vs. As_2^+ (As_2^{2+} vs. As_4^{2+}) for m/z = 75 (150) Da on the apparent stoichiometry in GaAs, GaAs:Si, and GaAsNBi.

We first assign m/z = 75 (150) Da to As^+ (As_2^{2+}), which associates each count in the peak to one (two) As atoms, resulting in the lowest As fractions as shown by the black-filled markers in Figure 3.4. With such assignment the As fractions are always underestimated (below 50 at. %) for laser-pulsed evaporation and overestimated (above 50 at. %) for voltage-pulsed evaporations. Underestimations of As fractions correlate with overestimations of Ga fractions and vice versa. For voltage-pulsed GaAs:Si, depicted by the black filled triangles in Figure 3.4, the As fractions are always above 50 at. %. The As overestimation could be related to preferential Ga evaporation at higher effective fields,[18] influences of Si-dopants, and/or the chosen mode of evaporation (i.e. laser vs. voltage).

For voltage-pulsed GaAs:Si, As overestimations are observed at effective fields in the range of 20.2 to 22.0 V/nm. However, As underestimations are also observed consistently within this field range, suggesting that the observed As overestimation in GaAs:Si is not be solely dependent on field. Experiments with As underestimations in this range include laser-pulsed GaAs:Si also suggests that the overestimation may not solely related to the Si dopants. More laser-pulsed GaAs:Si are needed to better understand influences of Si dopants. We conclude that the As fraction overestimations for GaAs:Si in our dataset are primarily related to the mode used for evaporation.[12]

We consider the second assignment of m/z = 75 (150) Da as As_2^{2+} (As_4^{2+}) on apparent stoichiometry, which are represented by open markers in Figure 3.4. For GaAs, such assignment consistently results in underestimations of the As fraction, as indicated by the black open squares. At $E_{eff} \approx 18$ V/nm (Ga-CSR = 0.2), the As (Ga) fractions are underestimated (overestimated) by roughly 26%. Both the determined Ga and As fractions approach 50 at. % with increasing field, which is in agreement with the trends observed in

GaAs[18] and InGaAs.[21] Near-stoichiometry for Ga:As (51.4:48.6 for the first assignment and 50.3:49.7 for the latter assignment) is reached at $E_{eff\text{-}Ga}$ ~ 20.5 V/nm, similar to a previous report.[18]

On the other hand, for laser-pulsed GaAs:Si and GaAsNBi, the Group V fractions are consistently overestimated, as shown by the black open diamonds and circles, respectively. Average variances (σ_{av}) for the atomic fractions between the two assignments are shown in Table 3.2. Variances are lower for laser-pulsed GaAs (~1 at. %), showing no significant difference in peak assignment on apparent stoichiometry. Variances in the Ga and Group V fractions are slightly larger for GaAsNBi tips (~7 at. %). Variances are much higher for GaAs:Si (~12 at. %) in both pulsed laser and voltage mode. This reveals that when assigning the 75 and 150 Da peaks to the doubly-charged clusters, As_2^{2+} and As_4^{2+}, respectively, the apparent stoichiometry is certainly influenced by the presence of dilutes species, such as N and Bi, and also, to a greater effect, Si dopants. As mentioned previously, the 75 and 150 Da peaks are conventionally assigned to the singly-charged species, As^+ and As_2^+, respectively. Such is often the case also when As-containing ternaries and quaternaries are being investigated by LEAP.[21] Our results show that for proper assignment of related m/z overlaps, critical evaluations of experimental parameters on apparent stoichiometries are necessary for each material system involved.

	Mode	$\sigma_{av\text{-}Ga}$	$\sigma_{av\text{-}V}$
GaAs	laser	1.2 ± 0.4 at. %	1.4 ± 0.5 at. %,
GaAsNBi	laser	6.9 ± 1.1%	7.4 ± 1.8 at. %
GaAs:Si	laser	12.0 ± 3.8 at. %	12.2 ± 3.8 at. %
GaAs:Si	voltage	11.71 ± 4.7 at. %	12.0 ± 4.6 at. %

Table 3.2 Average variances (σ_{av}) for the atomic fractions between the two assignments.

3.4.2 Determining Bi compositions

The Bi flux series films were achieved by independently varying the Bi beam-equivalent pressure (BEP) from 2E-08 to 8E-08 Torr. LEAP evaporation was performed at 0.25 pJ and 0.5 atoms/pulse detections rate. These conditions provided the nearest-stoichiometric fractions for GaAs. We, therefore, assign m/z = 75 (150) to As^+ (As_2^+) for determining N and Bi compositions. LEAP-determined N fractions determined were all < 0.5 at. % N for all GaAsNBi specimens.

LEAP-measured Bi fractions (open triangles) for the GaAsNBi samples are presented in Figure 3.5, along with measured Bi fractions from RBS (open squares). LEAP-measured Bi fractions ranged from 1.1 to 5.0 at. % and are in agreement with those from the RBS measurements in Figure 3.6. Due to the apparent non-uniformity in the film with highest Bi content (black curve), 4 layers with different 4 Bi compositions are assumed, resulting in the best SIMNRA fit. Resultant Bi compositions from the layers of this fit (6.61, 5.45, 5.10, and 4.42 at. %) are averaged and represented as 5.39 at. %. We note that for lighter elements, such as N, the RBS cross-section is too low to be detected with reliable accuracy.[42,43] In all cases, the N composition detected by LEAP was <0.5 at. %.

We examine the relative influence of N and Bi incorporation using HRXRC, similar to methods described in related studies.[29,30] HRXRC of the Bi flux series is presented in Figure 3.7. Due to their compressive and tensile misfit with respect to GaAs, GaAsBi and GaAsN diffraction peaks appear on the low-angle and high-angle sides of the GaAs substrate peak, respectively. In this case, the GaAsNBi peak is shifted from the high-angle side with negligible Bi incorporation to the low-angle side as the Bi incorporation is increased. For the measurement where the highest Bi is expected (BEP_{Bi} = 8E-8), no

GaAsNBi peak is observed, likely due to nonuniform Bi incorporation of Bi, mentioned previously. Nonuniform Bi incorporation is further supported by the absence of the Pendellosung fringes, which are indicators of smooth epilayer interfaces.[44] Due to misfit strain, higher Bi compositions may promote roughening of surfaces and interfaces[45] and the formation of Bi clusters.[46]

3.4.3 Investigating Si dopants in InAs/GaAs QD superlattices

For LEAP analysis of Si-doped InAs/GaAs QDs, ions were collected from prepared sample specimens using laser energies of 1 pJ. An example 3D LEAP reconstruction is presented in Figure 3.8(a), showing well-defined QD wetting layers in purple. Figure 3.8(b) displays a superimposed contour plot of the bottom layer, revealing an InAs QD with a maximum In composition of ~17 at. % and smaller clusters of Si dopants or "particles" with a maximum Si composition of ~1 at. %.

For calculating the carrier distribution, we model the InAs QD, wetting layer, and Si particles within nextnano using compositions, relative shapes, and sizes from LEAP. Figure 3.9 presents two example configurations for the InAs QDs and Si clusters: one with the Si particles positioned outside of the QD, as shown in Figures 3.9(a)-(f)) and one with the Si particles positioned both inside and outside of the QD, as shown in Figures 3.9(g)-(l)**.** For the first configuration on the left, the InAs QD is modeled as three conjoined ellipsoids with an In compositional gradient taken from LEAP. The maximum composition at the center of the QD is ~17 at. % In within an InAs wetting layer that has an averaged In composition of ~2.3 at. %, as shown in the x-y and x-z views in Figures 3.9(a) and 9(b), respectively. We note that the three conjoined ellipsoids are not the actual shape of the QD

but are similar to the shape in LEAP and are modeled as such for simplicity. Detailed information about the nextnano model is presented in Appendix C.

In the first model, the Si particle is positioned above of the QD displayed in Figure 3.9(a). The Si particle is represented by its dopant profile in Figure 3.9(c). It is assumed that the Si dopants are fully ionized; each Si atom donates one free electron to serve as a charge carrier. The In compositional profile from Figure 3.9(a)-(b) and the targeted dopant profile from Figure 3.9(c) is used to calculate the carrier concentration using the Poisson-Schrödinger solver.[1] Further details of this calculations, including the materials parameters and nextnano script, are located in Appendix C.

The resulting position-dependent carrier concentrations are plotted Figures 3.9(e) and (k). In the first model, carrier concentrations are localized within the QD (3.9 x 10^{17} cm^{-3}) and near the Si particle (1.6 x 10^{17} cm^{-3}), with nominal concentrations within the nearby wetting layer (<1 x 10^{17} cm^{-3}). Similar values are observed in the second model; the carrier concentration due to the dopants positioned outside of the QD is ~2.0 x 10^{17} cm^{-3} as indicated by the rectangular box in Figure 3.9(k). When the dopants are located within the QD, carrier concentrations are much higher (1.0 x 10^{18}), as shown in Figure 3.9(k).

The carrier concentration is higher at the QD center than in the wetting layer. Preliminary SThEM-1D Poisson studies suggest a reduced carrier concentration in the QD center in comparison to that of the 2D alloy layer.[3] However, current results show maximum carrier concentrations localized near Si particles and within the QD. Differences are likely related due to our observed inhomogeneity in the distribution of the dopants from LEAP. Previous studies assumed uniformly doped QDs. Further investigation of the calculated band structure profiles between the two methods are needed.

3.5 Summary and conclusions

We presented our investigations of stoichiometry and microstructure of III-V nanostructure alloys using LEAP, in conjunction with other methods including RBS, HRXRC, and nextnano. For laser-pulsed GaAs, non-stoichiometry is more pronounced at low fields and becomes less pronounced at high fields with Ga and As fractions nearing 50 at. % (effective field ~20.5 V/nm). We evaluated the apparent stoichiometry in GaAs, GaAs:Si, and GaAsNBi for both cases when assigning the m/z = 75 (150) Da to As^+ and As_2^{2+} (As^{2+} and As_4^{2+}). In general, LEAP determined Ga and Group V fractions are non-stoichiometric in both cases, but the variations between the assignments are small for laser-pulsed GaAs. Variations increase when considering GaAs:Si and GaAsNBi, suggesting field-induced influences on stoichiometry due to the presence of dilute species.

Stoichiometry is improved for GaAs when using low laser energies (0.25 pJ), thus similar conditions were used to determine N and Bi fractions. LEAP-determined Bi fractions in GaAsNBi are in good agreement with RBS measurements. N fractions determined from LEAP were all < 0.5 at. % N. The relative presence of N and Bi is observed in HRXRC measurements. Furthermore, for laser-pulsed GaAs, non-stoichiometry is more pronounced at low fields and becomes less pronounced at high fields with Ga and As fractions nearing 50 at. % (effective field ~20.5 V/nm). The apparent stoichiometry in GaAsNBi may follow a similar trend; results hint that the atomic fractions may approach to 50 at. %, though this may happen at a higher effective field (~22 V/nm). In Section 6.2.2, we discuss the implications this comparison to using this approach to

determining stoichiometry, and thus local compositions, to range of GaAs-related ternary and quaternary alloys.

Finally, we presented a combined experimental-computational approach to studying local carrier properties in Si-doped InAs/GaAs QDs. Results show maximum carrier concentrations localized near Si particles and within the QD. Preliminary SThEM-1D Poisson studies suggested a reduced carrier concentration in the QD center in comparison to that of the 2D alloy layer.[3] Differences are likely related due to our observed inhomogeneity in the distribution of the dopants from LEAP. Further investigation of the calculated band structure profiles between the two methods are needed. Approaches that combine LEAP and nextnano device simulations can be applied to many III-V systems, an example of which is discussed in Chapter 4 using GaSb/GaAs QDs.

The ability to accurately determine local compositions in III-V semiconductors is critical for using 3D information from LEAP as input into electronic structure calculations for QD nanostructures. Dopant concentrations and distributions, especially at QD interfaces, affect carrier scattering, recombination, and ultimately device efficiencies. Due to the practical and fundamental limitations of existing local probe techniques,[47] understanding and manipulating the local electronic properties of QDs, such as the carrier concentration (n), remains challenging. Si-doped InAs/GaAs QDs are modeled within nextnano using structural information from LEAP. The approach has valuable implications for nanoscale characterization of devices structures.[48,49]

3.6 Figures

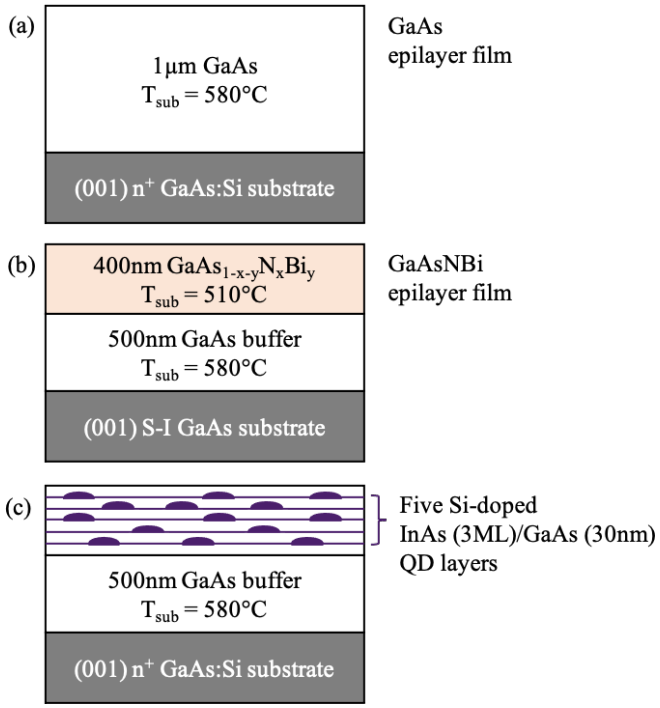

Figure 3.1 Sample structures for the MBE-grown (a) GaAs, (b) GaAsNBi, and (c) multi-layered InAs/GaAs QD films. For the growths, 500 nm GaAs was grown on a (001) n+ Si-doped or semi-insulating GaAs substrate followed by (a) 500 nm of GaAs, (b) 400 nm of GaAsNBi and (c) five layers of 3ML InAs quantum dots (QDs) with 30 nm GaAs spacers, followed by a 50 nm GaAs capping layer. For the InAs QD superlattice, both InAs and spacer regions were doped with silicon.

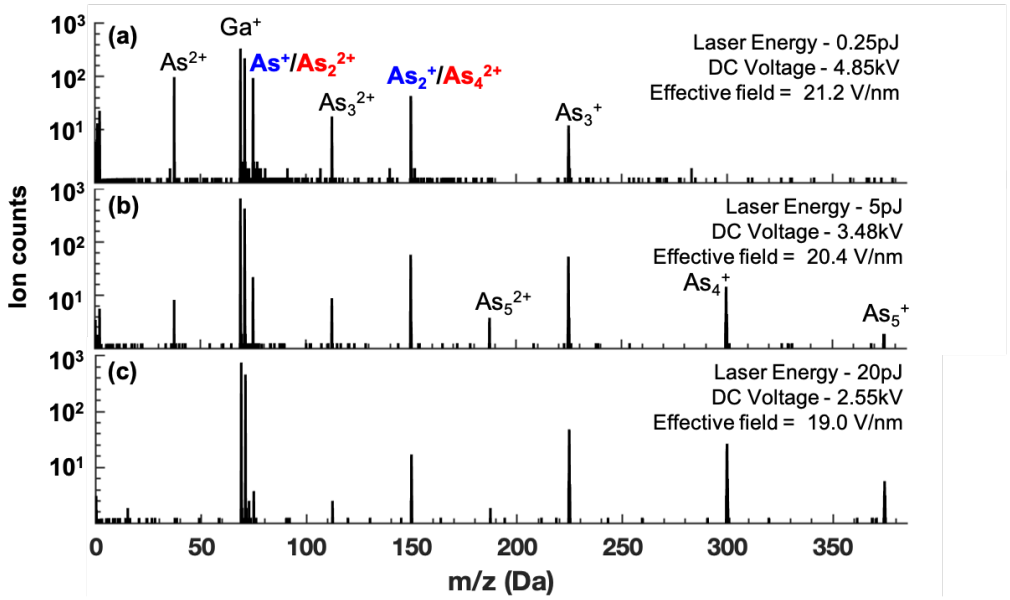

Figure 3.2 Selected mass spectra collected from GaAs measured by LEAP with laser pulse energies of (a) 0.25 pJ, (b) 5 pJ, and 20 pJ, plotted along with their respective voltages (V_{DC}) and estimated effective fields. Due to possible overlaps in the mass-to-charge ratio (m/z), the 75 Da (150 Da) peaks are labeled as As^+/As_2^{2+} (As_2^+/As_4^{2+}). Tip base temperature: 20K. Detection rate: $\varphi \approx 0.5$ events/pulse. Each dataset contains ~3 x 10^5 ions.

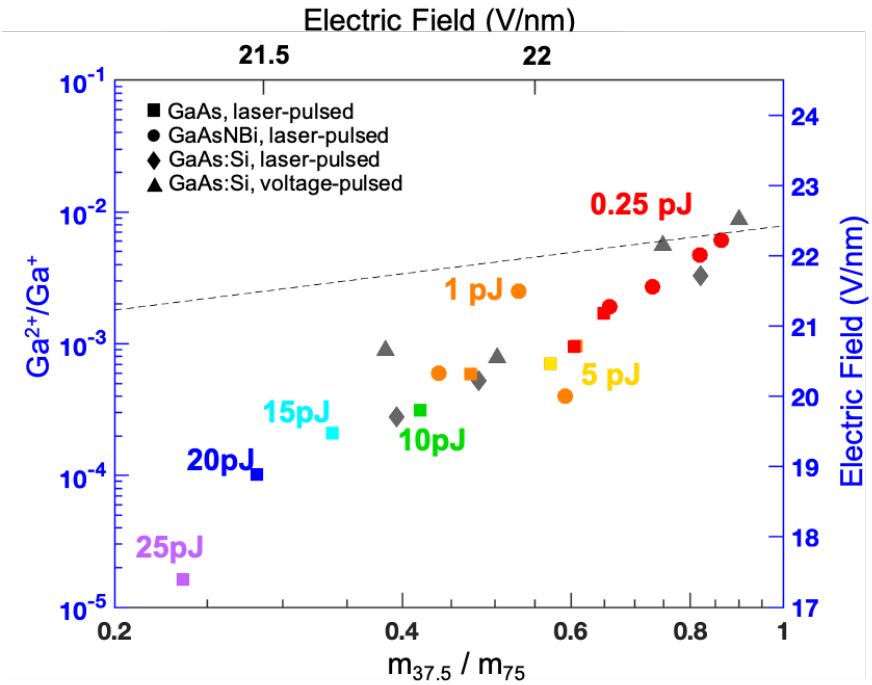

Figure 3.3 Plot showing the relationship between the experimental As^{2+}/As^{+} (As-CSR) and Ga^{2+}/Ga^{+} (Ga-CSR) observed in GaAs at laser energies ranging from 25 pJ to 0.25 pJ (filled squares) and GaAsNBi at 1 pJ and 0.25 pJ (filled circles). The effective fields derived from As-CSR (top axis) and Ga-CSR (right axis) were calculated according the Kingham's post-ionization theory.[39] The black dashed line indicates where fields based on the As-CSR and the Ga-CSR are equal. Detection rate: $\varphi \approx 0.5$ events/pulse.

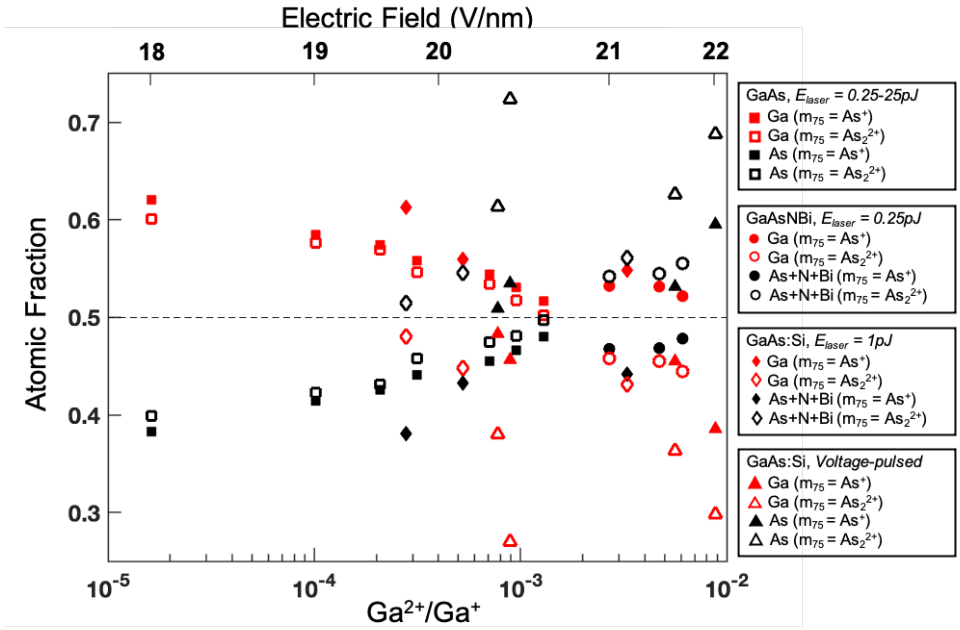

Figure 3.4 Plot showing correlation between estimated field and the Ga fractions (red) and As or Group V fractions (black) from the reconstructed datasets for laser-pulsed GaAs (squares), laser-pulsed GaAsNBi (circles), laser-pulsed GaAs:Si (diamonds), and voltage-pulsed GaAs:Si (triangles) specimens. Filled (open) markers represent Ga and As fractions determined by assigning the 75 and 150 Da peaks as As^+ and As_2^+ (As_2^{2+} and As_4^{2+}), respectively. Detection rate: $\varphi \approx 0.5$ events/pulse.

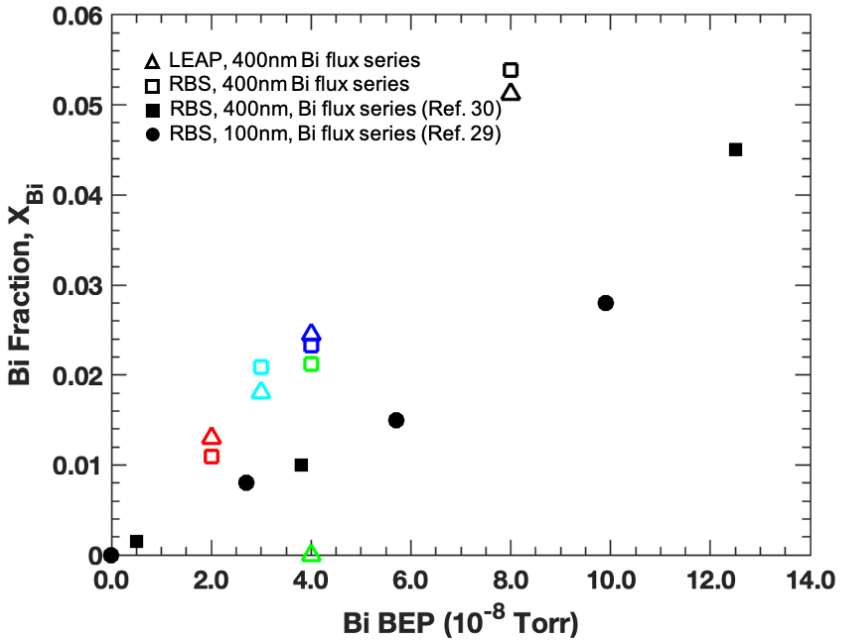

Figure 3.5 Bi fraction for GaAsNBi films determined by Rutherford Backscattering (RBS) for three sets of "Bi flux series" samples (open squares, closed squares, and closed circles) and LEAP (open triangles) as a function of Bi beam equivalent pressure (BEP). Colors correlated with RBS counts presented in Figure 3.6. Bi fractions from GaAsNBi are compared with those determined by RBS in previous studies.[29,30] Bi fraction, X_{Bi}, corresponds to the number of Bi atoms detected out of the total number of atoms (Ga + As + N + Bi).

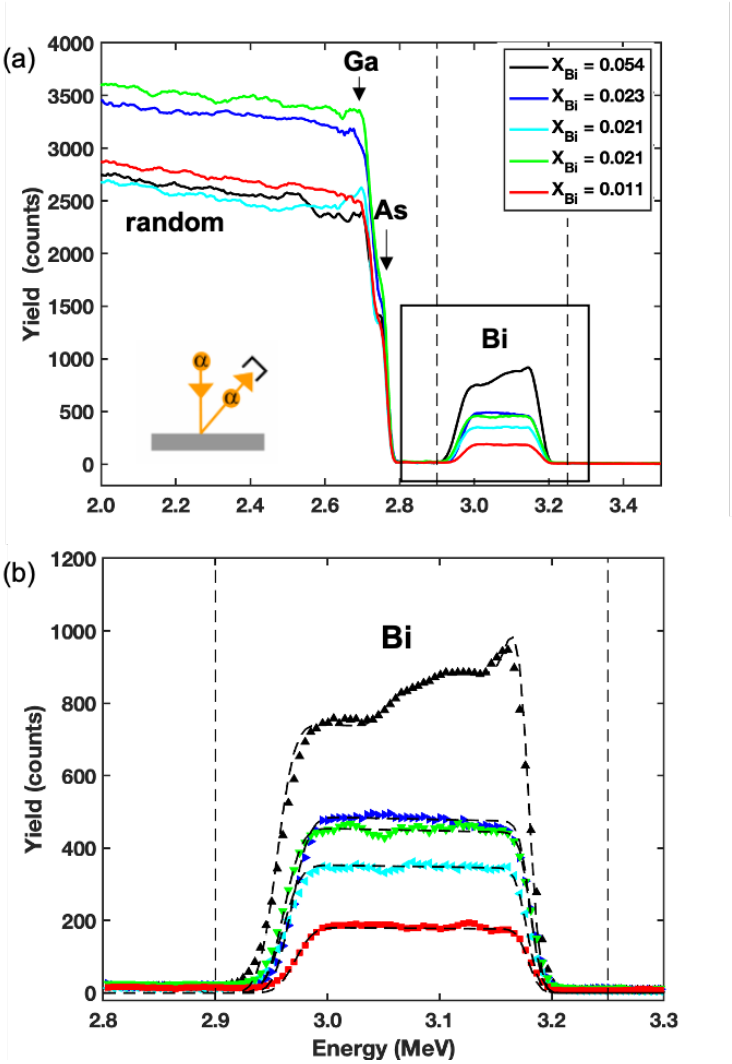

Figure 3.6 (a) Measured RBS yield versus backscattered particle energy for the Bi flux series. The vertical dashed lines indicated the energy window of ions backscattered from Bi atoms. As the Bi flux increases, the resulting Bi signal increases. The portions of the RBS spectra enclosed in the box in (a) are shown in (b). Non-channeling RBS data overlaid with fitted SIMNRA spectra assuming a uniform Bi depth profile. Bi fraction, X_{Bi}, corresponds to the number of Bi atoms detected out of the total number of atoms (Ga + As + N + Bi). Due to the non-uniformity in the RBS data for the black curve, 4 layers with different 4 Bi compositions are assumed, resulting in the best SIMNRA fit. Resultant Bi compositions (0.066, 0.055, 0.051, and 0.044) are averaged, represented as 0.054.

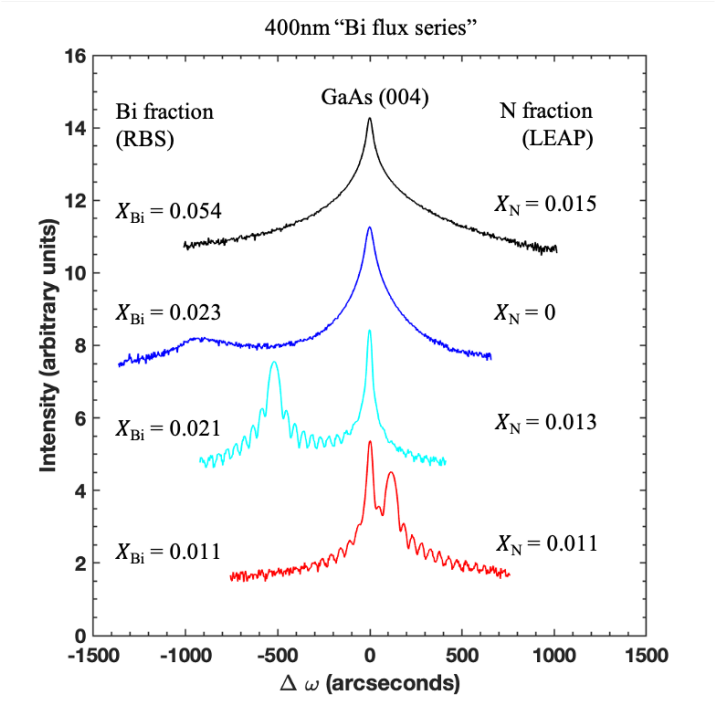

Figure 3.7 (004) high-resolution x-ray rocking curves for GaAsNBi samples with LEAP-measured Bi fractions ranging from 0.11 to 0.054. For all plots, the GaAs substrate peak is set to Δω = 0 arcseconds, thereby facilitating comparison of Δω between the GaAs substrate and the GaAsNBi epilayers. The N_{BEP} remains fixed, while Bi_{BEP} is increased from bottom (red) to top (black). Counts associated with GaAsNBi epilayer was not observed in this measurement, likely due to ununiform Bi distribution within the layer, as shown in RBS. Bi (N) fraction, X_{Bi}, (X_N) corresponds to the number of Bi (N) atoms detected out of the total number of atoms (Ga + As + N + Bi).*X_{Bi} = 0.054 represents averaged Bi fraction from SIMNRA.

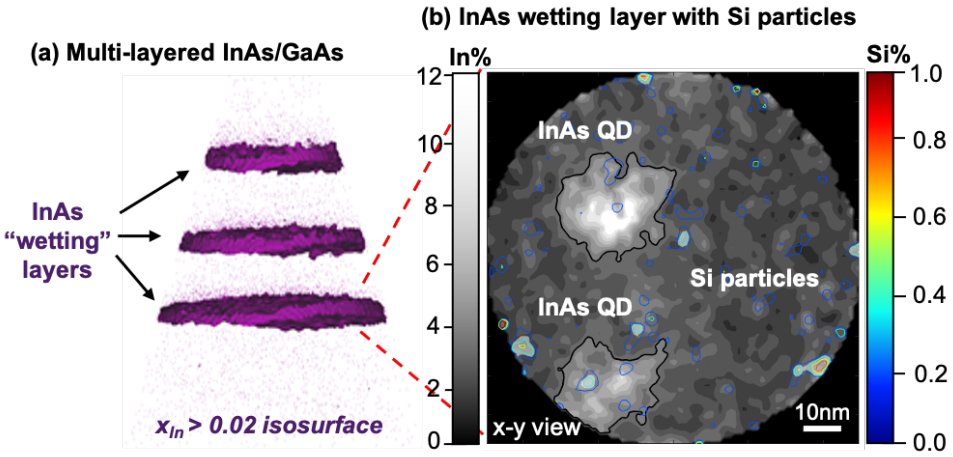

Figure 3.8 (a) LEAP reconstruction for multi-layered InAs/GaAs QDs revealing well-defined QD wetting layers, defined by a 2 at. % indium iso-surface (purple). (b) Superimposed contour plots of the fraction of In atoms (gray-scale) and the fraction of Si atoms (RGB color-scale) within the reconstructed volume. In concentrations are displayed in gray from darker (lower %In) to lighter (higher %In), while Si concentrations are displayed in color from blue (lower %Si) to red (higher %Si).

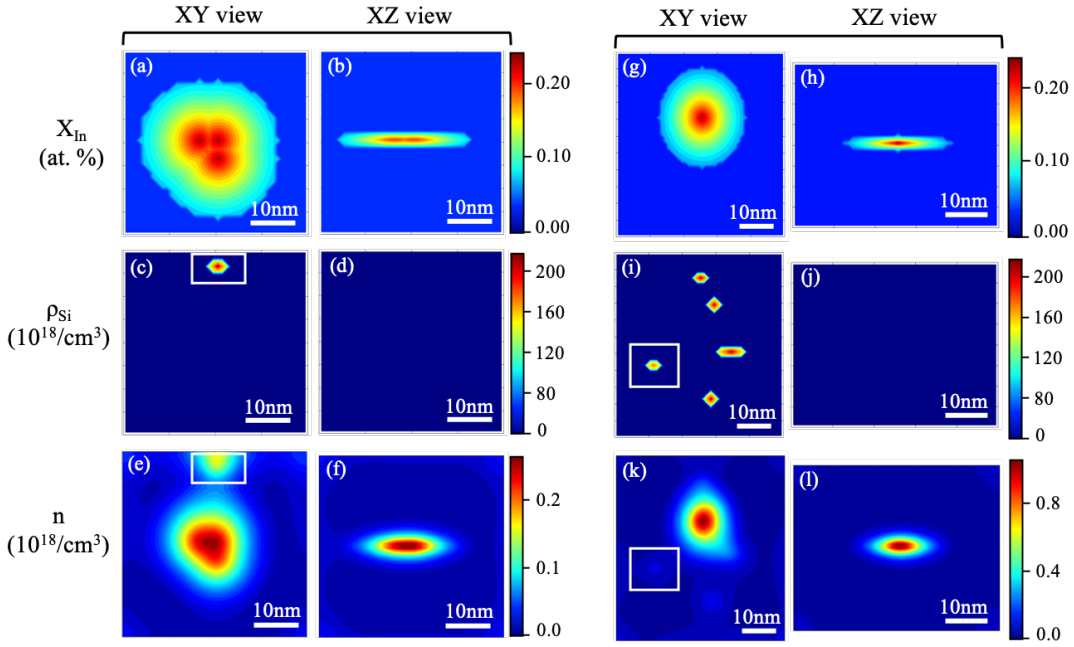

Figure 3.9 Nextnano: x-y and x-z view of the of the QD modeled as (a)-(b) three $In_xGa_{1-x}As$ ellipsoids and (g)-(h) one $In_xGa_{1-x}As$ ellipsoid immersed within an $In_xGa_{1-x}As$ quantum well. In compositional gradients (X_{In}) and relative sizes are taken from LEAP. X-y and x-z views of the donor densities, ρ_{Si}, from the Si clusters positioned (c)-(d) outside of and (i)-(j) both within and outside of the $In_xGa_{1-x}As$ QD. Si clusters positioned outside of the QDs are enclosed by a rectangular box for clarity. (e)-(f) and (k)-(l) Position-dependence of the local carrier density calculated using the respective X_{In}, Si dopant profiles, $m^*_{InAs} = 0.023m_e$, and $m^*_{GaAs} = 0.067m_e$.

3.7 References

[1] S. Birner, S. Hackenbuchner, M. Sabathil, G. Zangler, J. A. Majewski, T. Andlauer, T. Zibold, R. Morschl, A. Trellakis, and P. Vogl, "Modeling of Semiconductor Nanostructures with nextnano^3", Acta Phys. Pol. A 110, 111 (2006).

[2] T. Jen, "Ion Beam Analysis of Solute Incorporation in GaAsN and GaAsNBi Alloys", Ph.D. Thesis, University of Michigan, 2016, pp. 106 – 112.

[3] J. Walrath, "Probing the Band Structure and Local Electronic Properties of Low-Dimensional Semiconductor Structures", Ph.D. Thesis, University of Michigan, 2017, pp. 51 – 72.

[4] D. Blavette and S. Duguay, "Investigation of Dopant Clustering and Segregation to Defects in Semiconductors using Atom Probe Tomography", J. App. Phys. 119, 181502 (2016).

[5] T.F. Kelley and M.K. Miller, "Invited Review Article: Atom Probe Tomography", Rev. Sci. Instrum. 78, 031101 (2007).

[6] D.N. Seidman, "Three-Dimensional Atom-Probe Tomography: Advances and Applications", Ann. Rev. Mater. Res. 37, 127, (2007).

[7] A. Madhukar and S.V. Ghaisas, "Implications of the Configuration-dependent Reactive Incorporation Growth Process for the Group V Pressure and Substrate Temperature Dependence of III-V Molecular Beam Epitaxial Growth and the Dynamics of the Reflection High-energy Electron Diffraction Intensity", Appl. Phys. Lett. 47, 247 (1985).

[8] B.A. Joyce, "Molecular-beam Epitaxy", Rep. Prog. Phys. 48, 1637 (1985).

[9] A. Rockett, "The Materials Science of Semiconductors", Springer (2008).

[10] T. Sakurai, T. Hashizume, A. Jimbo, and T. Sakata, "An Atom-Probe Study of III-V Compound Semiconductors", J. Phys. Colloques. 45, 453 (1984).

[11] A. Cerezo, C.R.M. Grovenor, and G.D.W. Smith, "Pulsed Laser Atom Probe Analysis of GaAs and InAs", Appl. Phys. Lett. 46, 567–569 (1985).

[12] T. Hashizume, Y. Hasegawa, A. Kobayashi, T. Sakurai, "Atom-Probe Investigation of IIIV Semiconductors: Comparison of Voltage-Pulse and Laser-Pulse Modes", Rev. Sci. Instrum. 57, 1378 (1986).

[13] M. Yamamoto, D.N. Seidman, and S. Nakamura, "A Study of the Composition of the {111} Planes of GaP on an Atomic Scale", Surf. Sci. 118, 555–571 (1982).

[14] D.R. Diercks, B.P. Gorman, R. Kirchhofer, N. Sanford, K. Bertness, and M. Brubaker, "Atom Probe Tomography Evaporation Behavior of C-axis GaN nanowires: Crystallographic, Stoichiometric, and Detection Efficiency Aspects", J. Appl. Phys. 114, 184903 (2013).

[15] R.J.H. Morris, R. Cuduvally, D. Melkonyan, C. Fleischmann, M. Zhao, L. Arnoldi, P. vander Heide, and W. Vandervo, "Toward Accurate Composition Analysis of GaN and AlGaN Using Atom Probe Tomography", J. Vac. Sci. Technol. B 36, 03F130 (2018).

[16] J.R. Riley, R.A. Bernal, Q. Li, H.D. Espinosa, G.T. Wang, and L.J. Lauhon, "Atom Probe Tomography of *a*-Axis GaN Nanowires: Analysis of Nonstoichiometric Evaporation Behavior", AC Nano, 6, 3898 (2012).

[17] L. Mancini, N. Amirifar, D. Shinde, I. Blum, M. Gilbert, A. Vella, F. Vurpillot, W. Lefebvre, R. Lardé, E. Talbot, P. Pareige, X. Portier, A. Ziania, C. Davesnne, C. Durand, J. Eymery, R. Butté, J.-F. Carlin, N. Grandjean, and L. Rigutti, "Composition of Wide Bandgap Semiconductor Materials and Nanostructures Measured by Atom Probe Tomography and its Dependence on the Surface Electric Field", J. Phys. Chem. C. 118, 24136 (2014).

[18] E. Di Russo, I. Blum, J. Houard, G. Da Costa, D. Blayette, and L. Rigut, "Field-Dependent Measurement of GaAs Composition by Atom Probe Tomography", Microsc. Microanal. 23, 1067 (2017).

[19] A.M. Beltrán, E.A. Marquis, A.G. Taboadad, J.M. Ripaldad, J.M. García, S.I. Molina, "Three-dimensional Atom Probe Imaging of GaAsSb Quantum Rings", Ultramicroscopy, 111, 1073 (2011).

[20] M. Müller, D.W. Saxey, G.D.W. Smith, and B. Gault, "Some Aspects of the Field Evaporation Behaviour of GaSb", Ultramicroscopy 111, 487 (2011).

[21] R. Cuduvally, R.J.H. Morris, P. Ferrari, J. Bogdanowicz, C. Fleischmann, D. Melkonyan, and W. Vandervorst, "Potential Sources of Compositional Inaccuracy in the Atom Probe Tomography of $In_xGa_{1-x}As$", Ultramicroscopy, 210, 112918 (2020).

[22] J.A. Liddle, A. Norman, A. Cerezo, and C.R.M. Grovenor, "Pulsed Laser Atom Probe Analysis of Ternary and Quaternary III-V Epitaxial Layers", J. Phys. Colloques 49, 509 (1988).

[23] B.P. Gorman, H. Guthrey, A. Norman, M. Al-Jassim, D. Lawrence, and T.J. Prosa, "Atomic Scale Characterization of Compound Semiconductors using Atom Probe Tomography", IEEE Photovoltaic Specialists Conference, Seattle, WA, p.13 (2011).

[24] D.W. Saxey, "Correlated Ion Analysis and the Interpretation of Atom Probe Mass Spectra", Ultramicroscopy, 111, 473 (2011).

[25] C. Brechignac, P. Cahuzac, F. Carlier, M. Defrutos, J. Leygnier, and J.P. Roux, "Gas-phase Dissociation Pathways of Multiply Charged Peptide Clusters", J. Chem. Phys. 102, 763 (1995).

[26] B. Gault, D.W. Saxey, M.W. Ashton, S.B. Sinnott, A.N. Chiaramonti, M.P. Moody, and D.K. Schreiber, "Behavior of Molecules and Molecular Ions Near a Field Emitter", New J Phys 18, 033031 (2016).

[27] G. Da Costa, H. Wang, S. Duguay, A. Bostel, D. Blavette, B. Deconihout, Advance in Multi-hit Detection and Quantization in Atom Probe Tomography, Rev. Sci. Instrum. 12, 83 (2012).

[28] M. Müller, G.D.W. Smith, B. Gault, and C.R.M. Grovenor, "Compositional Nonuniformities in Pulsed Laser Atom Probe Tomography Analysis of Compound Semiconductors", J. Appl. Phys. 111, 064908 (2012).

[29] J. Occena, T. Jen, E.E. Rizzi, T.M. Johnson, J. Horwath, Y.Q. Wang, and R.S. Goldman, "Bi-enhanced N Incorporation in GaAsNBi Alloys", Appl. Phys. Lett. 110, 242102 (2017).

[30] J. Occena, T. Jen, H. Lu, B.A. Carter, T.S. Jimson, A.G. Norman, and R.S. Goldman, "Surfactant-induced Chemical Ordering of GaAsN:Bi", Appl. Phys. Lett. 113, 211602 (2018).

[31] J. Maguire, R. Murray, and R.C. Newman, "Mechanism of Compensation in Heavily Silicon-doped Gallium Arsenide Grown by Molecular Beam Epitaxy", Appl. Phys. Lett. 50, 516 (1987).

[32] G. Beainy, R. Alcotte, F. Bassani, M. Martin, A. Grenier, T. Baron, and J.P. Barnes, "Direct Examinations of Si Atoms in Spatial Distribution and Clustering in GaAs Thin Films with Atom Probe Tomography", Script. Mat. 153, 109 (2018).

[33] P. De Wolf, R. Stephenson, T. Trenkler, T. Clarysse, T. Hantschel, and W. Vandervorst, "Status and Review of Two-dimensional Carrier and Dopant Profiling using Scanning Probe Microscopy," J. Vac. Sci. Technol. B. 18, 361 (2004).

[34] G.M. Dalpian and J.R. Chelikowsky, "Self-Purification in Semiconductor Nanocrystals", PRL, 96, 226802 (2006).

[35] V. D. Dasika, A. V. Semichaevsky, J. P. Petropoulos, J. C. Dibbern, A. M. Dangelewicz, M. Holub, P. K. Bhattacharya, J. M. O. Zide, H. T. Johnson, and R. S. Goldman, *Appl. Phys. Lett.* **98**, 141907 (2011).

[36] M. Reason, H.A. McKay, W. Ye, S. Hanson, R.S. Goldman, and V. Rotberg, "Mechanisms of Nitrogen Incorporation in GaAsN Alloys", Appl. Phys. Lett. 85, 1692 (2004).

[37] Simon Huang, "Formation, Structure, and Properties of InAs/GaAs Quantum Dots", Ph.D. Thesis, University of Michigan, 2015, p. 47 – 61.

[38] M. Mayer, W. Eckstein, H. Langhuth, F. Schiettekatte, and U. von Toussaint, "Computer Simulation of Ion Beam Analysis: Possibilities and Limitations", Nucl. Instrum. Meth. B 269, 3006 (2011)

[39] D.R. Kingham, "The Post-ionization of Field Evaporated Ions: A Theoretical Explanation of Multiple Charge States", Surf. Sci. 116, 273 (1982).

[40] E. Di Russo, N. Cherkashin, M. Korytov, A. E. Nikolaev, A. V. Sakharov, A. F. Tsatsulnikov, B. Bonef, I. Blum, J. Houard, G. Da Costa, D. Blavette, and L. Rigutti, "Compositional Accuracy in Atom Probe Tomography Analyses Performed on III-N Light Emitting Diodes", J. Appl. Phys. 126, 124307 (2019).

[41] T. Grieb, K. Müller, E. Cadel, A. Beyer, M. Schowalter, E. Talbot, K. Volz, and A. Rosenauer, "Simultaneous Quantification of Indium and Nitrogen Concentration in InGaNAs Using HAADF-STEM", Microsc. Microanal. 20, 1740 (2014).

[42] L.C. Feldman and J.W. Mayer, *Fundamentals of Surface and Thin Film Analysis*, (Elsevier Science Publishing, The Netherlands, 1986).

[43] J.R. Tesmer and M.A. Nastasi, *Handbook of Modern Ion Beam Materials Analysis* (Materials Research Society, Pittsburgh, 1995).

[44] W.K. Cheah, W.J. Fan, S.F. Yoon, S.Z. Wang, and W.K. Loke, "X-ray Reciprocal Space Mapping of Strain Relaxation in $GaAs_{1-x}N_x$ on GaAs [100] by Molecular-beam Epitaxy", J. Appl. Phys. 94, 3828 (2003).

[45] S. Spruytte, M. Larson, W. Wampler, C. Coldren, H. Petersen, and J. Harris, "Nitrogen Incorporation in Group III–nitride–arsenide Materials Grown by Elemental Source Molecular Beam Epitaxy", J. Cryst. Growth, 227-228, 506 (2001).

[46] M.V. Warren, J.C. Canniff, H. Chi, F. Naab, V.A. Stoica, R. Clarke, C. Uher, and R.S. Goldman, "Influence of Bi on Embedded Nanocrystal Formation and Thermoelectric Properties of GaAs", J. App. Phys. 117, 065101 (2015).

[47] P. De Wolf, R. Stephenson, T. Trenkler, T. Clarysse, T. Hantschel, and W. Vandervorst, "Status and Review of Two-dimensional Carrier and Dopant Profiling using Scanning Probe Microscopy", J. Vac. Sci. Technol. B 18, 361 (2000).

[48] B.P. Gorman, A.G. Norman, and Y. Yan "Atom Probe Analysis of III–V and Si-Based Semiconductor Photovoltaic Structures", Microsc. Microanal. 13, 493 (2007).

[49] A.S. Chang and L.J. Lauhon, "Atom Probe Tomography of Nanoscale Architectures in Functional Materials for Electronic and Photonic Applications", 22, 171 (2018).

Chapter 4

Influence of Quantum Dot Morphology on the Optical Properties of GaSb/GaAs Multilayers

4.1 Overview

We examine the influence of quantum dot (QD) morphology on the optical properties of two-dimensional (2D) GaSb/GaAs multilayers, with and without 3D nanostructures. Using nanostructure sizes from scanning transmission electron microscopy (STEM) and local Sb compositions from local electrode atom probe (LEAP) tomography as input into self-consistent Schrödinger-Poisson simulations based on 8 x 8 **k·p** theory, we compute confinement energies for quantum dots (QDs), circular arrangements of smaller QDs, termed QD-rings, and 2D layers on GaAs substrates. The computed confinement energies and the measured photoluminescence emission energies increase from QDs to QD-rings to 2D layers, enabling direct association of nanostructure morphologies with the optical properties of the GaSb/GaAs multilayers. This work opens opportunities for tailoring near to far infrared optoelectronic devices by varying the QD morphology. This work was supported by the National Science Foundation (NSF) through the Graduate Research Fellowship Program (No. DGE 1256260) and (Grant No. ECCS-1610362). We also acknowledge the assistance of the staff at the Michigan Center for Materials

Characterization at the University of Michigan. This work has been published in *Applied Physics Letters*.[1]

4.2 Background

Due to the predicted strain and composition dependence of nested (type-I) versus staggered (type-II) band alignments,[2] GaSb/GaAs QDs are promising for a variety of optoelectronic applications, including solar-cells,[3] photodetectors,[4] charged-based memory[5,6] and light-emitters.[7] Typically, the nucleation of three-dimensional (3D) nanostructures from two-dimensional (2D) GaSb "wetting" layers shifts photoluminescence (PL) emissions further into the infrared range. In addition, within GaSb/GaAs multilayers, atomic structures ranging from QDs to quantum rings (QRs) and clusters have been observed.[8-10] However, the association of emission energies with specific nanostructure types (i.e., QDs vs. QRs vs. clusters) remains elusive. For example, PL energies at 0.92 eV[11], 1.01–1.05 eV[12], 1.1eV,[13,14] 1.13–1.18 eV,[15] and 1.2 eV[16] have been attributed to capped GaSb QDs with heights ranging from 6 to 10 nm, with no apparent correlation between QD size and emission energy. On the other hand, similar PL energies of 0.9-1.08 eV,[17] 0.95 eV,[18] 1.02 eV, and 1.06 eV[19] have been attributed to GaSb QRs. In some cases, multiple-peak emissions for GaSb QDs are attributed to bimodal size distributions.[20] Indeed, the nanoscale morphology is seldomly discussed in reports on multi-layered GaSb/GaAs devices. To date, there is a lack of consensus on the origins of various emission energies for GaSb/GaAs multilayers.

Here, we report on the morphology and optical properties of GaSb/GaAs multilayers, with and without 3D nanostructures. Using cross-sectional scanning

transmission electron microscopy (XSTEM), local electrode atom-probe tomography (LEAP), and PL spectroscopy, in conjunction with Schrödinger-Poisson simulations based on 8 x 8 **k·p** theory, we identify the influences of nanostructure height and core composition on PL emissions. We associate emissions, in order of increasing energy: QDs, circular arrangements of smaller QDs, termed QD-rings (QDRs), and 2D layers (or wetting layers [WLs]). This work opens up opportunities for tailoring PL emission energies by varying QD morphology, as needed for optimizing near-to-far-infrared optoelectronic devices.

4.3 Methods

4.3.1 MBE growth of GaSb/GaAs QDs

For these investigations, GaSb layers were deposited on p-type GaAs (001) substrates by molecular-beam epitaxy using solid Ga, As_2, and Sb_2 sources. Following oxide desorption and growth of an initial 400-nm thick GaAs buffer layer at 580 °C, the substrate temperature was lowered to 510 °C for the growth of five periods of GaSb/GaAs superlattices (SLs) consisting of alternating layers of GaSb (3 or 4 MLs thick) and 25 nm p-GaAs spacers, with a 20 nm p-GaAs capping layer. The targeted thicknesses were determined using growth rate calibrations based upon reflection high-energy electron diffraction (RHEED) oscillations, similar to the method described by Bennett et al.[21] Assuming that each RHEED oscillation period corresponds to the growth of one monolayer of GaSb,[22] we obtain a GaSb growth rate for each specific Sb/Ga beam-equivalent pressure ratio. Then, the time for flux exposure is adjusted to target the requisite number of

monolayers (MLs). The 3ML and 4ML GaSb layers were grown at a rate of 0.4 μm/hr with Sb/Ga beam-equivalent pressure (BEP) ratios of 1 and 7, respectively. To reduce Sb/As exchange during deposition, Sb soaking steps were avoided.[23,24]

4.3.2 XSTEM and LEAP experimental procedures

Following growth, thin foils for XSTEM were prepared using mechanical grinding to <20 μm, followed by argon-ion milling, using a Gatan Precision Ion Polishing system.[25] Bright (BF) STEM was carried out at 300 kV using the JEOL 3100. For LEAP studies, conical-shaped specimens were prepared by a standard lift-out procedure and loaded into the Cameca LEAP 4000X, which was maintained at cryogenic temperatures (<25 K) under ultra-high vacuum conditions (3.0×10^{-11} Torr), similar to earlier studies of GaAsSb.[26] LEAP experiments were performed in voltage-pulsing mode at 200 kHz with a 20% pulse fraction and constant detection rate of 37%. 3D reconstructions of LEAP datasets were performed using Cameca's Integrated Visualization and Analysis Software. PL measurements (T=20 K) were collected in a helium flow cryostat using a 250 μm slit, single channel InGaAs detector, and 10 mW HeNe laser operating at 633 nm. Finally, using nanostructures size and Sb composition gradients from STEM and LEAP, hole confinement energies in $GaAs_{1-x}Sb_x$/GaAs were calculated using nextnano.[27]

4.4 Results and Discussion

4.4.1 Structural properties of GaSb/GaAs nanostructures (XSTEM)

Large-scale XSTEM images of the 3ML and 4ML GaSb/GaAs superlattices, shown in Figure 4.1(a) and (b), reveal isolated WLs and WLs with 3D nanostructures, respectively. Henceforth, we refer to the 3ML (4ML) superlattice as "2DLs" ("2DLs+3DNSs"). We note the presence of clustering in the first (bottom) GaSb layer, as indicated by yellow arrows in Figure 4.1(b). Since the volume of deposited GaSb in each layer is constant, the 3D nanostructures in subsequent layers are likely due to enhanced island nucleation at strain energy minima above buried islands.[28] Although dislocations are not apparent in the vicinity of the nanostructures, strain-induced Sb out-diffusion into the GaAs spacers may have occurred, as depicted by the black arrows in Figure 4.1(b).

To identify and quantify the nanostructure types within 2DLs+3DNSs, we apply the following criteria. For GaSb QDs, as shown in Figure 4.1(c), Sb atoms form a "lens" shape, similar to earlier studies of GaSb/GaAs and InAs/GaAs.[2,25] In addition, nanostructures with distinct lobes of Sb are apparent, as depicted by white dotted lines in Figure 4.1(d) and (e). We denote nanostructures with two and three (or more) distinct Sb lobes as (d) QRs and (e) clusters, respectively. Due to their similar structures, the formation mechanisms of the QRs/clusters are expected to be similar.[8,10,29] Finally, the average heights for the QDs (QRs/clusters) are 7 ± 4 nm (4 ± 2 nm). In a region of ~200 μm^2, 114 GaSb nanostructures were observed, with 64% QDs, 17% QRs, and 18% clusters.

4.4.2 Structural properties of GaSb/GaAs nanostructures (LEAP)

To determine Sb incorporation into the GaSb layers, we consider x-z views of LEAP reconstructions for 2DLs and 2DLs+3DNSs in Figures 4.2(a) and 4.2(b), along with representative 1D profiles of the fraction of Sb atoms, x_{Sb}, in blue. Due to premature tip

fracturing at ~7kV during the LEAP experiment, data for two (three) of the five layers were collected for 2DLs (2DLs+3DNSs). For 2DLs and 2DLs+3DNSs, the average x_{Sb} values are 0.08 and 0.12 within the 2D layers, with x_{Sb}< ~0.01 within the GaAs spacer regions.

To determine local x_{Sb}, we consider isosurfaces at various x_{Sb} thresholds. Figure 4.3(a) shows the x_{Sb} > 0.20 isosurface of 2DLs, with x-y views of the top layer at x_{Sb} > 0.04, 0.08, 0.10 and 0.16 in Figure 4.3(b), (c), (d), and (e), respectively. As the x_{Sb} threshold increases from 0.04 in Figure 4.3(b) to 0.16 in Figure 4.3(e), spatial variations in x_{Sb} are observed. For 2DLs, the maximum x_{Sb} is approximately 0.18, and 3D nanostructures are not apparent, consistent with the XSTEM images in Figure 4.1(a).

For 2DLS+3DNS, the x_{Sb} > 0.24 isosurface is shown in Figure 4.4(a), with x-y views of the top layer at x_{Sb} > 0.24 in Figure 4.4(b) and the bottom layer at x_{Sb} > 0.28 in Figure 4.4(c). Maximum core values of x_{Sb} = 0.90 (0.42) for a QD (QR) are presented in Figure 4.4(b). It is interesting to note that as the x_{Sb} threshold increases from > 0.24 to 0.28, the apparent "QR" in the bottom layer of Figure 4.4(a) consist of a circular arrangement of QDs with smaller Sb-rich cores as shown Figure 4.4(c), which we term quantum dot ring (QDR). At the centers of the individual cores of the QDR, the maximum values of x_{Sb} are 0.36, 0.38, 0.40, and 0.42, as indicated in Figure 4.4(c). We note that the QDR structures are similar to the GaSb clusters defined in Figure 4.1(e). Variations in the Sb composition amongst the WLs, QDs, and QDRs are likely due to differences in their formation mechanisms. In particular, the lower Sb composition within the QDRs in comparison to that of the QDs might be due to strain relief via Sb out-diffusion, as suggested by earlier reports.[8,10,30,31] Furthermore, the lower composition in the WL in comparison to that of the

3D nanostructures may be due to Sb adatoms that cluster together during growth but then disintegrate if the critical thickness for QD formation is not reached.[32]

4.4.3 Optical properties of GaSb/GaAs nanostructures (PL)

We now discuss the influence of QD morphology on PL emissions. Figure 4.5 shows contour plots of x_{Sb} within a (a) GaSb QD and (b) GaSb QDR, along with (c) PL spectra for 2DLs (orange) and 2DLs+3DNSs (blue) normalized to the GaAs peak at 1.48 eV. For both cases, PL emissions at 1.33 and 1.48 eV are attributed to the WLs and the GaAs donor-acceptor transition, respectively. A similar trend is observed for the computed values of the WL transition energy (1.29 eV) and the GaAs bandgap energy (1.52 eV), as described in supplementary materials. Broadening of the WL peak in 2DLs likely arises from the local variations in the Sb composition, as presented in Figures 4.3(b)-(d).

For the 2DLs + 3DNSs, additional PL emissions are observed at 1.08 and 1.20 eV. We note from XSTEM that most (~64%) of the nanostructures are QDs, with average height = 7nm and maximum $x_{Sb} = 0.90$, and the remainder are QDRs/clusters with lower average height 4nm and lower maximum $x_{Sb} = 0.48$. Since the effective band gap of GaAs is inversely proportional to x_{Sb} and emission energies are inversely proportional to QD size,[33] we tentatively attribute the 1.20 and 1.08 eV emissions to QDRs/clusters and QDs, respectively.

4.4.4 Band structure of GaSb/GaAs nanostructures (nextnano)

Confined hole energies were calculated using an 8 x 8 $\mathbf{k}\cdot\mathbf{p}$ approximation within the nextnano commercial software package.[27] Strain was calculated in the continuum

elasticity approach with elastic constants from Vurgaftman et al.[34] Values for band offsets[35] within model-solid theory[36] and deformation potentials[37] were subsequently used to calculate the conduction and valence bands, assuming a 1.43 eV[34] bowing parameter for GaSb-GaAs. Finally, the confined energy levels were determined by solving the Schrödinger and Poisson equations, self-consistently, as described elsewhere.[27,38,39]

For our calculations, three configurations of nanostructures in a GaAs matrix were utilized: a quantum dot (QD) with a 2D "wetting" layer (WL), a quantum dot ring (QDR) with a WL, and a WL only. Because the WL thickness exceeds the critical thickness for strain relaxation for GaSb/GaAs (1.2ML),[40] we assume the layers are partially strain-relaxed, with a lattice parameter halfway between bulk GaSb (0.609 nm) and its GaAs barrier (0.565 nm)[41] The QD model consisted of a $GaAs_{1-x}Sb_x$ ellipsoid with Sb compositional gradients from LEAP and dimensions from XSTEM, as shown in Figure 4.6. A similar model is used for the quantum-dot-ring (QDR) with dimensions and local Sb compositions presented in Table 4.1 Finally, the computed band edge energies (CB, HH, LH, and SO), confined hole energies (hh1 and hh2), ground-state energies (E_0), and excited-state energies (E_1) for (a) QD, (b) QDR, and (c) 2D WL are presented in Figure 4.7 For the QDs, the first and second hole-confinement energies (hh1 and hh2) are 0.60 and 0.48 eV, leading to a 120 meV energy difference between ground and first excited states. For the QDRs, hh1 and hh2 are calculated to be 0.34 and 0.20 eV, corresponding to a 140 meV energy difference, as shown in Figure 4.7.

$GaAs_{1-x}Sb_x$	QD	QDR	2D Layer
height (nm)	7	4	--
width (nm)	21	10	--
2D layer thickness (nm)	2	2	2
maximum Sb composition (x_{Sb})	0.90	0.42	0.20

Table 4.1 Average dimensions from cross-sectional scanning tunneling microscopy and local compositions from local electrode atom probe used in Schrödinger-Poisson calculations.

4.5 Summary and conclusions

Schrödinger-Poisson calculations reveal hole confinement energies of 0.34 and 0.60 eV, corresponding to 1.18 and 0.92 eV transition energies for the QDRs and QDs. Similar trends for the computed transition energies and measured PL energies confirm our assignment of the QDR/clusters and QD emissions. Since the energy difference between the ground and excited states is important for light-emitting device and solar cell applications, we report the calculated excited state energies in 0. Furthermore, the diminished intensity of the WL emission for 2DLs+3DNSs is likely due to preferential carrier confinement within the 3D nanostructures. Similar intensities of the QDR and QD emissions suggest non-preferential carrier confinement within both nanostructure types.

We also discussed a detailed analysis of structural properties of the Ga(As)Sb QDs, QD-rings, and clusters. Large-scale STEM images reveal Sb segregation for some of the nanostructures, as denoted by the arrows in Figure 4.1. This segregation of Sb is likely a part of a strain relief mechanism, where Sb diffuses into the GaAs spacer regions and in some cases in the layers above. Furthermore, defects or dislocations may present in the structure, which are common in GaSb QD systems. In this case, Sb may along the path of the dislocations to relieve the compressive strain of being confined to the nanostructures.

While STEM images hint at the possibility of 60˚ misfit dislocations, the dark contrast resulting from the high-angle annular dark field detector used may be a result of multiple features, including artifacts of heavy elements and film thickness. In Chapter 6, we propose a method for quantifying strain fields around the nanostructures, which can give more information about their formation mechanisms. Strain tensors can further be used as experimental input into band structure calculations to allow for more realistic determination of electronic properties.

Finally, we have examined the influence of QD morphology on the optical properties of GaAsSb/GaAs multilayers. We used the nanostructure sizes from STEM and local Sb composition from LEAP tomography as input into Schrödinger-Poisson simulations of confinement energies for QDs, QD-rings, and 2D layers. Due to the similar trends in computed transition energies and measured PL emission energies, we associate the emissions, in order of increasing energy, to QDs, QDRs, and 2D layers. This work opens opportunities for tailoring PL emission energies for near to far-infrared optoelectronics by varying the QD morphology.

4.6 Figures

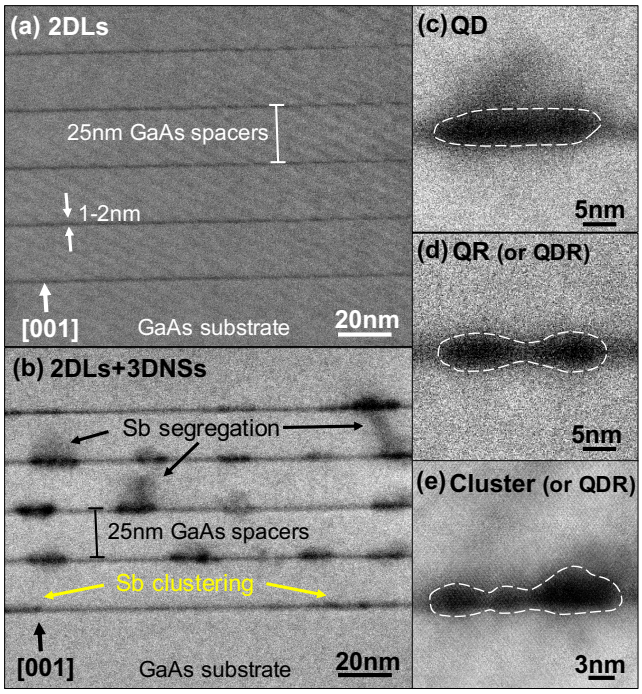

Figure 4.1 Cross-sectional scanning transmission electron micrographs of GaSb/GaAs multilayers containing (a) two-dimensional layers (2DLs) and (b) GaSb 2D layers with 3D nanostructures (2DLs+3DNSs), with arrows depicting possible locations of Sb out-diffusion. Close-up views for the nanostructures are also shown: (c) GaSb QD, (d) GaSb QR/QDR, and (e) GaSb cluster/QDR. Reprinted with permission from Ref. 1 (Copyright 2020, AIP Publishing).

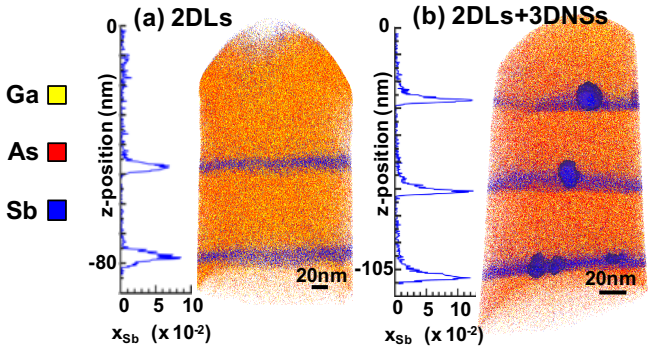

Figure 4.2 Three-dimensional reconstructions of local-electrode atom probe (LEAP) data from GaSb/GaAs multi-layers containing (a) two-dimensional layers (2DLs) and (b) GaSb 2D layers with 3D nanostructures (2DLs+3DNSs). Within the LEAP reconstructions, Sb, Ga, and As atoms are shown in blue, red, and yellow, respectively. 1D profiles of the Sb compositions within the reconstructed volume, x_{Sb}, are shown to the left of each 3D reconstruction. Reprinted with permission from Ref. 1 (Copyright 2020, AIP Publishing).

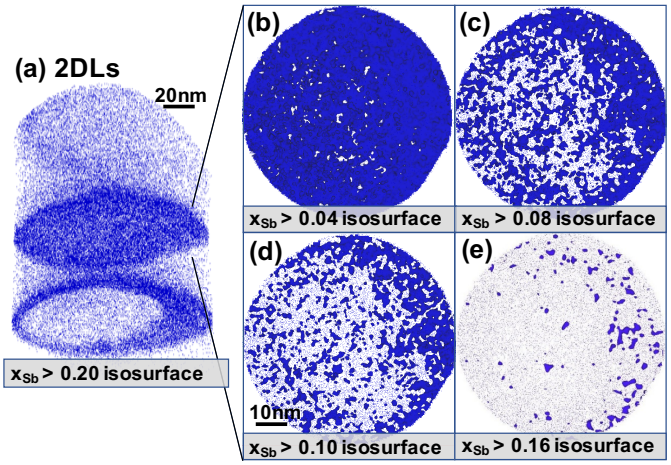

Figure 4.3 (a) Local electrode atom probe iso-surfaces for GaSb/GaAs two-dimensional layers (2DLS): Sb iso-surface for (a) the entire conical specimen with $x_{Sb} > 0.20$ and x-y views of the top layer with (b) $x_{Sb} > 0.04$, (c) $x_{Sb} > 0.08$, (d) $x_{Sb} > 0.10$, and (e) $x_{Sb} > 0.16$. Lateral variations of x_{Sb} are apparent within GaAsSb 2DLs. Reprinted with permission from Ref. 1 (Copyright 2020, AIP Publishing).

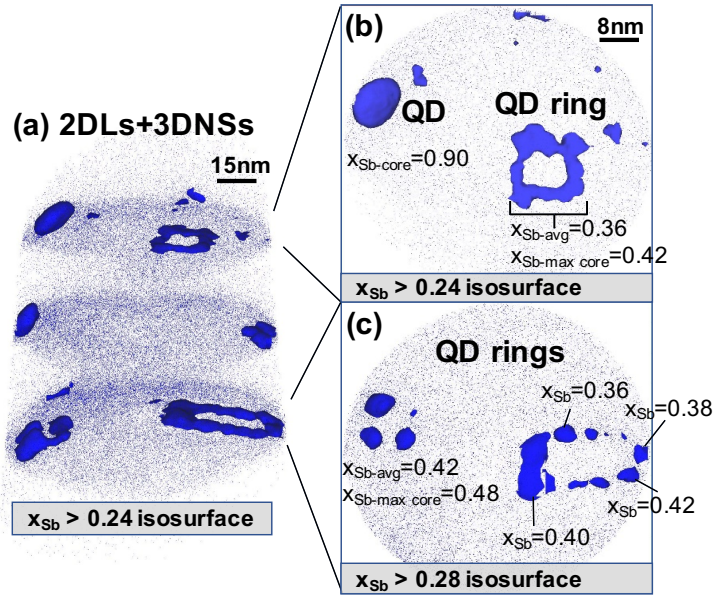

Figure 4.4 Local electrode atom probe iso-surfaces for two-dimensional layers with three-dimensional nanostructures (2DLS+3DNSs): Sb iso-surface for (a) the entire conical specimen with $x_{Sb} > 0.24$ and x-y views of (b) the top layer with $x_{S\ b} > 0.24$, and (c) the bottom layer with $x_{Sb} > 0.28$ for the 2DLs+3DNSs. Increasing the x_{Sb} of the iso-surfaces of the bottom layer reveal that the quantum rings consist of circular arrangements of quantum dots with Sb-rich cores, termed quantum dot rings. Reprinted with permission from Ref. 1 (Copyright 2020, AIP Publishing).

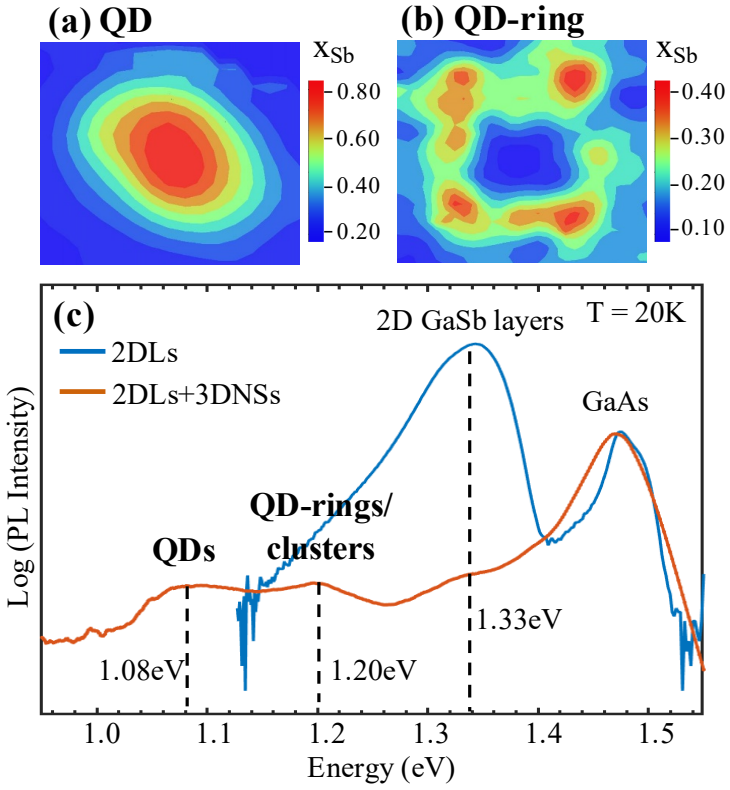

Figure 4.5 Comparison of quantum dot (QD) morphologies with photoluminescence (PL) emissions: contour plots of the fraction of Sb atoms within the reconstructed volume, x_{Sb}, for (a) a GaSb QD and (b) a quantum dot ring (QDR), with colors ranging from blue to red for low to high values. (c) Normalized photoluminescence spectra collected at 20K from 2DLs (in blue) and 2DLs+3DNSs (in orange). Features at 1.48 eV and 1.33 eV are associated with GaAs donor-acceptor and the GaSb wetting layers transitions, respectively. Features at 1.2 and 1.08 eV are associated with emissions from the QDRs/clusters and QDs, respectively. Similar trends are computed for the transition energies of the QDs (0.92 eV), QDRs (1.18 eV), and WLs (1.29 eV), as well as for the GaAs bandgap energy (1.52 eV. Reprinted with permission from Ref. 1 (Copyright 2020, AIP Publishing).

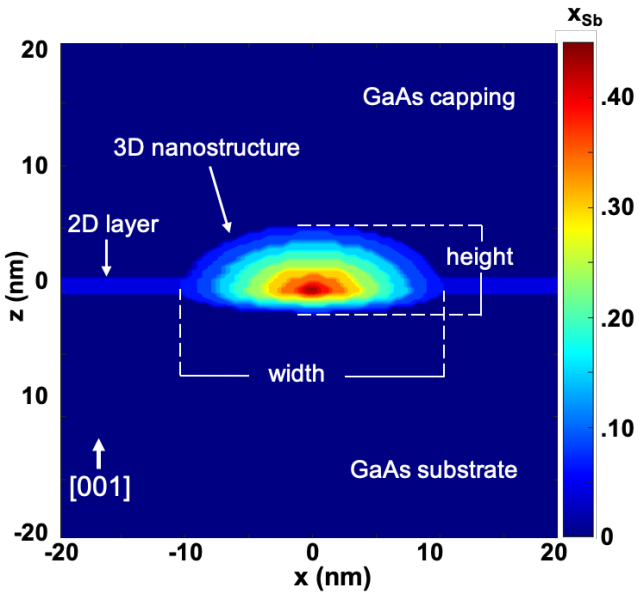

Figure 4.6 Representative x-z view of simulation region for the $GaAs_{1-x}Sb_x$ quantum dot (QD) embedded in GaAs with compositional gradient from local electrode atom probe (LEAP) and dimensions from scanning transmission electron microscopy (STEM). Reprinted with permission from Ref. 1 (Copyright 2020, AIP Publishing).

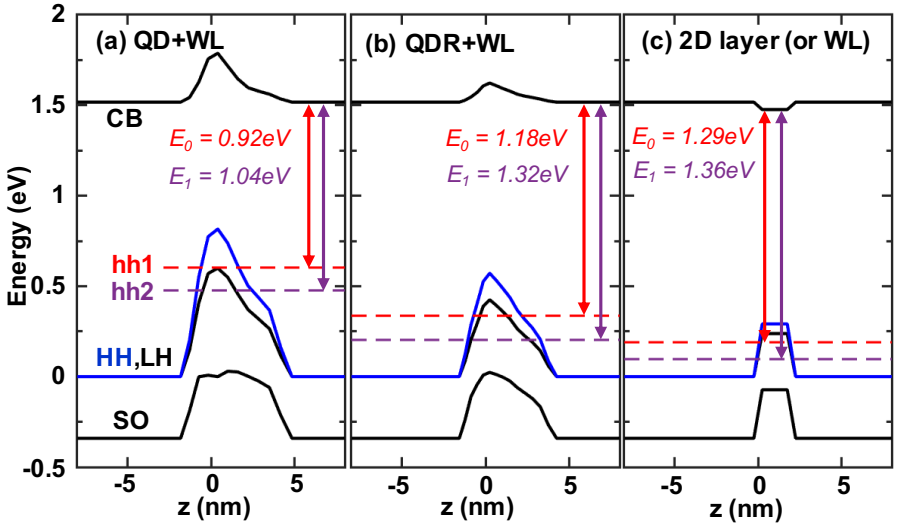

Figure 4.7 Plots of conduction and valence band edge energies as a function of distance for the (a) quantum dot (QD), (b) the quantum dot ring (QDR), and (c) the 2D layer, all defined with respect to the GaAs valence-band edge (VBE). The conduction-band-edge (CB), light-hole (LH) and split-off (SO) VBEs are denoted by black solid lines, while the heavy-hole (HH) VBE are denoted by blue solid lines. In addition, the first confined hole energy state (hh1) and second confined hole energy state (hh2) within the VBE is illustrated by dashed red and purple lines, respectively. Transition energies (E_0) and first excited state energies (E_1) are defined as the energy separation between the GaAs CBE and hh1 and the GaAs CBE and hh2, respectively. Reprinted with permission from Ref. 1 (Copyright 2020, AIP Publishing).

4.7 References

[1] C. Greenhill, A.S. Chang, E.S. Zech, S. Clark, G. Balakrishnan, and R.S. Goldman, "Influence of Quantum Dot Morphology on the Optical Properties of GaSb/GaAs Multilayers", Appl. Phys. Lett. 116, 252107 (2020).

[2] M. Hayne, J. Maes, S. Bersier, V. V. Moshchalkov, A. Schliwa, L. Müller-Kirsch, C. Kapteyn, R. Heitz, and D. Bimberg, "Electron Localization by Self-Assembled GaSb/GaAs Quantum Dots", Appl. Phys. Lett. 82, 4355 (2003).

[3] Y. Shoji, R. Tamaki, and Y. Okada, "Multi-stacked GaSb/GaAs Type-II Quanutm Nanostructures for Application to Intermediate Band Solar Cells", AIP Adv. 7, 65305 (2017).

[4] W.H. Lin, C.C. Tseng, K.P. Chao, S.C. Mai, S.Y. Kung, S.Y. Wu, S.Y. Lin, and M.C. Wu, "High-temperature Operation GaSb/GaAs Quantum-dot Infrared Photodetectors", IEEE Photonics Technol. Lett. 23, 106 (2011).

[5] M. Geller, C. Kapteyn, L. Müller-Kirsch, R. Heitz, and D. Bimberg, "450 meV Hole Localization in GaSb/GaAs Quantum Dots", Appl. Phys. Lett. 82, 2706 (2003).

[6] M. Hayne, R.J. Young, E.P. Smakman, T. Nowozin, P. Hodgson, J.K. Garleff, P. Rambabu, P.M. Koenraad, A. Marent, L. Bonato, A. Schliwa, and D. Bimberg, "The Structural, Electronic and Optical Properties of GaSb/GaAs Nanostructures for Charge-based Memory", J. Phys. D. 46, 264001 (2013).

[7] S.-Y. Lin, C.-C. Tseng, W.-H. Lin, S.-C. Mai, S.-Y. Wu, S.-H. Chen, and J.-I. Chyi, "Room-temperature Operation Type-II GaSb/GaAs Quantum-dot Infrared Light-emitting Diode", Appl. Phys. Lett. 96, 123503 (2010).

[8] R. Timm, A. Lenz, H. Eisele, L. Ivanova, M. Dähne, G. Balakrishnan, D.L. Huffaker, I. Farrer, and D.A. Ritchie, "Quantum Ring Formation and Antimony Segregation in GaSb/GaAs Nanostructures", J. Vac. Sci. Technol. B 26, 1492 (2008).

[9] A.J. Martin, J. Hwang, E.A. Marquis, E. Smakman, T.W. Saucer, G. V. Rodriguez, A.H. Hunter, V. Sih, P.M. Koenraad, J.D. Phillips, and J. Millunchick, "The Disintegration of GaSb/GaAs Nanostructures upon Capping", Appl. Phys. Lett. 102, 113103 (2013).

[10] E.P. Smakman, J.K. Garleff, R.J. Young, M. Hayne, P. Rambabu, and P.M. Koenraad, "GaSb/GaAs Quantum Dot Formation and Demolition Studied with Cross-sectional Scanning Tunneling Microscopy", Appl. Phys. Lett. 100, 142116 (2012).

[11] J. Tatebayashi, A. Khoshakhlagh, S.H. Huang, L.R. Dawson, G. Balakrishnan, and D.L. Huffaker, "Formation and Optical Characteristics of Strain-relieved and Densely Stacked GaSb/GaAs Quantum Dots", Appl. Phys. Lett. 89, 203116 (2006).

[12] M.A. Kamarudin, M. Hayne, Q.D. Zhuang, O. Kolosov, T. Nuytten, V. V. Moshchalkov, and F. Dinelli, "GaSb Quantum Dot Morphology for Different Growth Temperatures and the Dissolution Effect of the GaAs Capping Layer", J. Phys. D. 43, 065402 (2010).

[13] Motlan, K.S.A. Butcher, E.M. Goldys, and T.L. Tansley, "Multilayer GaSb/GaAs Self-Assembled Quantum Dots Grown by Metalorganic Chemical Vapor Deposition", Mater. Chem. Phys. 81, 8 (2003).

[14] C. Tseng, S. Mai, W. Lin, S.-Y. Wu, B.-Y. Yu, S.-H. Chen, S.-Y. Lin, J.-J. Shyue, and M.-C. Wu, "Influence of As on the Morphologies and Optical Characteristics of GaSb/GaAs Quantum Dots", IEEE J. Quantum Electron. 47, 335 (2011).

[15] A.J. Martin, T.W. Saucer, K. Sun, S. Joo Kim, G. Ran, G. V. Rodriguez, X. Pan, V. Sih, and J. Millunchick, "Analysis of Defect-free GaSb/GaAs (001) Quantum Dots Grown on the Sb-terminated (2x8) Surface", Vac. Sci. Technol. B 30, 02B112 (2012).

[16] M. DeJarld, L. Yan, M. Luengo-Kovac, V. Sih, and J. Millunchick, "Structural Differences Between Capped GaSb nanostructures Grown by Stranski-Krastanov and Droplet Epitaxy Growth Modes", J. Appl. Phys. 121, 034301 (2017).

[17] R.J. Young, E.P. Smakman, A.M. Sanchez, P. Hodgson, P.M. Koenraad, and M. Hayne, "Optical Observation of Single-carrier Charging in Type-II Quantum Ring Ensembles", Appl. Phys. Lett. 100, 082104 (2012).

[18] P.J. Carrington, R.J. Young, P.D. Hodgson, A.M. Sanchez, M. Hayne, and A. Krier, "Long-wavelength Photoluminescence from Stacked Layers of High-Quality Type -II GaSb/GaAs Quantum Rings", Cryst. Growth Des. 13, 1226 (2013).

[19] M.A. Kamarudin, M. Hayne, R.J. Young, Q.D. Zhuang, T. Ben, and S.I. Molina, "Tuning the Properties of Exciton Complexes in Self-assembled GaSb/GaAs Quantum Rings", Phys. Rev. B 83, 115311 (2011).

[20] M. Kunrugsa, S. Panyakeow, and S. Ratanathammaphan, "GaSb/GaAs Quantum-ring-with-dot Structures Grown by Droplet Epitaxy", J. Crys. Growth. 416, 73, (2015).

[21] B.R. Bennett and B.V. Shanabrook, "Molecular Beam Epitaxy of Sb-based Semiconductor Thin Films: Heteroepitaxial Systems, Singapore, World Scientific, pp. 401 – 452 (1999).

[22] J. Sudijono, M.D. Johnson, M.B. Elowitz, C.W. Snyder, and B.G. Orr, "An STM Study of Molecular-beam Epitaxy Growth of GaAs", Surf. Sci. 280, 247 (1993).

[23] R. Timm, A. Lenz, H. Eisele, L. Ivanova, and M. Dähne. "Quantum Ring Formation and Antimony Segregation in GaSb/GaAs Nanostructures", J. Vac. Sci. Technol. B 26, 4 (2008).

[24] H-A. Chen, T-C. Shih, S-F. Tang, P.K. Weng, Y-T. Gau, and S-Y. Lin. "GaSb/GaAs Quantum Dots and Rings Grown Under Periodical Growth Mode by Using Molecular Beam Epitaxy", J. Cryst. Growth. 425, 283, (2015).

[25] N. Fernández-Delgado, M. Herrera, M.F. Chisholm, M.A. Kamarudin, Q.D. Zhuang, M. Hayne, and S.I. Molina, "Atomic-column Scanning Transmission Electron Microscopy Analysis of Misfit Dislocations in GaSb/GaAs Quantum Dots", J. Mater. Sci. 51, 7691 (2016).

[26] A.M. Beltrán, E.A. Marquis, A.G. Taboada, J.M. Ripalda, J.M. García, and S.I. Molina, "Three-Dimensional Atom Probe Imaging of GaAsSb Quantum Rings", Ultramicroscopy 111, 1073 (2011).

[27] S. Birner, S. Hackenbuchner, M. Sabathil, G. Zangler, J. A. Majewski, T. Andlauer, T. Zibold, R. Morschl, A. Trellakis, and P. Vogl, "Modeling of Semiconductor Nanostructures with nextnano^3", Acta Phys. Pol. A 110, 111 (2006).

[28] J. Tersoff, C. Teichert, and M. G. Lagally, "Self-organizatin in Growth of Quantum Dot Superlattices", Phys. Rev. Lett. 76, 1675 (1996).

[29] R. Blossey and A. Lorke, "Wetting Droplet Instability and Quantum Ring Formation", Phys. Rev. E 65, 21603 (2002).

[30] A. Lorke, R.J. Luyken, J.M. Garcia, and P.M. Petroff. "Growth and Electronic Properties of Self-Organized Quantum Rings", Jpn. J. Appl. Phys. 40, 1857 (2001).

[31] S. Kobayashi, C. Jiang, T. Takuya, and H. Sakai. "Self-assembled Growth of GaSb Type II Quantum Ring Structure", Jpn. J. Appl. Phys. 43, 662, (2004).

[32] B.R. Bennett, P.M. Thibado, M.E. Twigg, E.R. Glaser, R. Magno, B. V. Shanabrook, and L.J. Whitman, "Self-assembled InSb and GaSb Quantum Dots on GaAs(001)", J. Vac. Sci. Technol. B Microelectron. Nanom. Struct. 14, 2195 (1996).

[33] N.N. Ledentsov, J. Böhrer, M. Beer, F. Heinrichsdorff, M. Grundmann, D. Bimberg, S. V. Ivanov, B.Y. Meltser, S. V. Shaposhnikov, I.N. Yassievich, N.N. Faleev, P.S. Kop'Ev, and Z.I. Alferov. "Radiative States in Type-II GaSb/GaAs Quantum Wells", Appl. Phys. Lett. 67, 656 (1995).

[34] I. Vurgaftman, J. R. Meyer, and L. R. Ram-Mohan, "Band parameters for III-V Compound Semiconductors and Their Alloys," J. Appl. Phys. 89, 5815 (2001).

[35] S.-H. Wei and Zunger, "Calculated Natural Band Offsets of All II-VI and III-V Semiconductors: Chemical Trends and the Role of Cation d Orbitals", Appl. Phys. Lett. 72, 2011 (1998).

[36] C.G. Van de Walle, “Band Lineups and Deformation Potentials in the Model-solid Theory”, Phys. Rev. B: Condens. Matter 39, 1871, (1989).

[37] S.-H. Wei and Zunger, “Predicted Band-gap Pressure Coefficients of All Diamond and Zinc-blende Semiconductors: Chemical Trends”, Phys. Rev. B: Condens. Matter Mater. Phys. 60, 5404 (1999).

[38] S. Birner, T. Zibold, T. Andlauer, T. Kubis, M. Sabathil, A. Trellakis, and P. Vogl, “nextnano: General Purpose 3-D Simulations”, IEEE Trans. Electron Devices. 54, 2137 (2007).

[39] A. Trellakis, T. Zibold, T. Andlauer, S. Birner, R. K. Smith, R. Morschl, and P. Vogl, “The 3D Nanometer Device Project nextnano: Concepts, Methods, Results”, J. Comput. Electron. 5, 285 (2006).

[40] H. Eisele and M. Dähne, “Critical Thickness of the 2-dimensional to 3-dimensional Transition in GaSb/GaAs(001) Quantum Got Growth”, J. Cryst. Growth. 338, 103 (2012).

[41] C. Jones and E. Kioupakis, “Effect of Strain on Band Alignment of GaAsSb/GaAs Quantum Wells”, J. Appl. Phys. 122, 045703 (2017).

Chapter 5

Probing Topological Surface States and Bulk Conduction in $(Bi_{1-x}Sb_x)_2Te_3$ Films

5.1 Overview

This chapter presents our investigations of the local band structure and carrier transport in topologically insulating $(Bi_{1-x}Sb_x)_2Te_3$ thin films using scanning tunneling microscopy/spectroscopy (STM/S) and magneto-transport measurements. STS reveals both the Fermi level and the Dirac point located inside the bulk band gap, indicating bulk-like insulating behavior with accessible topological surface states (TSSs). For the $(Bi_{1-x}Sb_x)_2Te_3$ films, the Fermi level shifts from the valence band towards the conduction band with increasing thickness and decreasing x composition, with a p-type to n-type crossover near $x \approx 0.6$. A two-channel conduction model is used to determine the density and mobility of n-type and p-type carriers, which are attributed to surface and bulk states.

BiSbTe thin films described in this chapter were grown by molecular-beam epitaxy (MBE) by Dr. V.A. Stoica, Dr. W. Liu, and Dr. L. Endicott in the laboratory of Professor Ctirad Uher at the University of Michigan. STM/S data were taken by the Goldman STM lab, including Dr. Jenna Walrath, the author, and Dr. Alexander Chang. Magneto-transport measurements, described in Section 2.8, were conducted by the author. This work is being prepared for publication.

5.2 Background

Topological insulators (TIs), such as BiSe-, BiTe- and SbTe-based materials, are an exciting class of quantum materials possessing a bulk band gap and gapless topological surfaces states (TSSs). The linear dispersion of the TSSs near the Fermi level (E_F) give rise to Dirac fermion behavior of the TSSs.[1,2] Such band structure enables spin-momentum locking of surface electrons[3] and prohibits backscattering,[4] making them of great interest for spintronics and quantum computing.[5-7] Bi_2Te_3 and Sb_2Te_3 are of particular interest for spintronics, due to observations that Te anti-site (Te_{Bi}) defects (Bi_2Te_3), Sb vacancies (V_{Sb}) and Sb anti-site (Sb_{Te}) defects (Sb_2Te_3) lead to n-type and p-type conduction, respectively.[8-14] Two major drawbacks for Bi_2Te_3 and Sb_2Te_3, due to their native defects, is that the Fermi level is pinned within the bulk conduction band (BCB) and bulk valence band (BVB), respectively, as shown in Figures 5.1(a) and 5.1(c). Furthermore, the Dirac point (DP) is pinned within the BVB for Bi_2Te_3. As illustrated in Figure 5.1(b), alloys of Bi_2Te_3-Sb_2Te_3 may contain combinations of Te_{Bi}, V_{Sb}, and Sb_{Te}, leading to carrier compensation with the Fermi level inside the gap[15-17] forming an insulating bulk. It is of current interest to bring the Dirac point to a position within the insulating gap, effectively reducing bulk conduction while making surface electrons accessible for transport. In this work, we use scanning tunneling microscopy/spectroscopy (STM/S) to directly probe local band structure of $(Bi_{1-x}Sb_x)_2Te_3$ films with Sb compositions $0.58 \leq x \leq 0.68$ and thicknesses ranging from 6 nm to 30 nm. The Fermi level and Dirac point are detected inside the gap at room temperature using STS, revealing a cross-over regime from n-type to p-type conduction[18,19] at $x \approx 0.6$ for $(Bi_{1-x}Sb_x)_2Te_3$ films.

Furthermore, an n/p anomaly has been previously observed, where room-temperature Hall/Seebeck data show opposite signs, indicating n-type/p-type conduction for $(Bi_{1-x}Sb_x)_2Te_3$ films, $x \approx 0.6 - 0.7$.[19,20] It was proposed that n-type surface states dominate magnetoelectric transport (Hall), whereas p-type bulk states dominate the thermoelectric transport (Seebeck).[19] However, Hall measurements at a single magnetic field values provide average values of carrier properties, which may not be representative of the individual species in a mixed conduction system. To examine surface versus bulk carrier transport, we perform magneto-transport measurements at magnetic fields ranging from 0 to 14T. We then use a two-channel conduction model[21] for conduction is employed to extract the mobilities and densities for each carrier species, enabling separation of conductivity contributions from bulk majority carriers and surface carriers. We discuss the alloy composition and film thickness dependence of the band structure and transport properties.

5.3 MBE growth procedures

For these investigations, Bi_2Te_3-Sb_2Te_3 alloy films were grown by molecular beam epitaxy (MBE) on sapphire (0001) substrates, followed by annealing in a tellurium flux for 3.5 hours to control the Te:Bi-Sb ratio and to promote smooth surface morphology.[22] The Bi:Sb ratio was controlled by the temperatures of the Bi and Sb Knudsen-type cells. The growth conditions were monitored in-situ by reflection high-energy electron diffraction (RHEED KSA 400). RHEED oscillations as a function of time are shown in Figure 5.2(a), and the streak spacing as function of time is shown in Figure 5.2(b). The increase in streak spacing around 275 s corresponds to a decrease in the lattice constant, which could indicate

the presence of an interface layer[23-26] before establishment of the standard tetradymite structure later in growth.

Film thickness (nm)	x	VBE (eV)	CBE (eV)	E_g (eV)	Carrier Type
6	0.68	0.011	0.176	0.17 ± 0.10	p-type
18	0.64	0.002	0.198	0.20 ± 0.10	p-type
30	0.64	-0.077	0.139	0.22 ± 0.10	pn*
30	0.58	-0.155	-0.007	0.15 ± 0.10	n-type

*carrier-compensated

Table 5.1 $(Bi_{1-x}Sb_x)_2Te_3$ sample composition, thickness, valence band edge (VBE), conduction band edge (CBE), effective band gap (E_g), and carrier type. VBE, CBE, and E_g were determined using room-temperature scanning tunneling spectroscopy (STS).

STM/S was used to image and probe the local band structure of the films at room-temperature using procedures described in Section 2.7. Magneto-transport measurements performed at magnetic fields ranging from 0 to 14T using 4-terminal resistance measurements described in Section 2.8. To analyze the conductivity, we convert magnetoresistance and Hall measurements to their respective conductivities, σ_{xx} and σ_{xy}, as described in Appendix C.

5.4 STM/S of $(Bi_{1-x}Sb_x)_2Te_3$ films

Figure 5.3 shows large-scale STM images of the surface topography for the (a) 6 nm, (b) 18 nm, and (c) 30 nm $(Bi_{1-x}Sb_x)_2Te_3$ films. Line cuts across the images reveal terraces with step heights of ~1 nm, as expected for quintuple layer structures in high-quality layer-by-layer growth of the van der Waals bonded layers.[27] STM images reveal a diverse morphology for the terraces, with roughly circular terraces and sizes ranging from

50 – 100nm. The number of steps around each terrace varies from 1 – 2 in the 6 nm film to 3 – 5 terraces in the 18 nm and 30 nm films.

The differential conductance (dI/dV) for each of the films is presented in Figure 5.4. For all samples, the effective band gaps range from 0.15 to 0.22 ± 0.10 eV, consistent with previous studies of $(Bi_{1-x}Sb_x)_2Te_3$ alloys,[15,25] as shown in Table 5.1. For the 6 nm film (highest Sb composition, x = 0.68), the Fermi level (E_F) is positioned near valence band edge (VBE), suggesting that p-type carriers are dominant. As the film thickness increases from 6 to 30nm, the Fermi level shifts away from the valence band and towards the middle of energy gap. We also consider the effect of compositions on the carrier type, as shown in Figure 5.5. The $(Bi_{1-x}Sb_x)_2Te_3$ film with x = 0.58 is distinctly n-type, with E_F located at the CBE. As the film composition increases from x = 0.58 to 0.68, the Fermi level shifts away from the CBE for the x = 0.58 film to the VBE for the x = 0.68 film, indicating an increase in p-type defects due to the increasing Sb.[15,28] For the 30 nm, x = 0.64 film, the Fermi level is closest to the middle of the energy band gap, suggesting compensation between n-type and p-type carriers. The effective E_g for this film is also larger, suggesting more insulating behavior. Thus, the Fermi level is tuned across the gap, with an n- to p-type transition occurring at $x \approx 0.6$, similar to previous studies using resistance measurements.[18] The conduction type of BiSbTe alloys is known to shift from n-type to p-type (or vice versa) with composition differences of less than 0.1, consistent with our STS observations.[15]

5.5 STS of bulk and topological surface states

To probe TSSs within the films, we adjust the tip-sample separation to reveal two distinct states of surface (red) and bulk conduction (black), as shown in Figures 5.6(a) and

(b). In the energy range of the bulk gap, TSSs show V-shaped spectra with the zero-conductance point corresponding to the Dirac point (E_D).[29] In Figure 5.6(a), STS spectra taken on the 30 nm $(Bi_{1-x}Sb_x)_2Te_3$ film with x = 0.58 film reveal a V-shaped spectrum with E_D near -50 meV. For the 30 nm film with x = 0.64, E_D is near 50 meV, which is similar to STS studies of Sb_2Te_3 thin films.[13,25] The approximate positions of E_D are marked by arrows on Figures 5.6(a) and 5.6(b). The shift in E_D from below to above E_F indicates a change in carrier-type dominance from electrons to holes.[15,30] For the 30 nm films, both E_F and E_D are located within the bulk band gap, indicating bulk insulating behavior with distinguishable and accessible TSSs. For the 18 nm, E_D is located within the valence band. No distinct surface state spectra were observed for the 6 nm film.

5.6 Hall and magnetoresistance measurements

To examine surface versus bulk carrier transport, magneto-transport measurements were performed as a function of magnetic fields between 0 and 14 T. We assume two-carrier transport where both bulk conduction (σ_b) and surface conduction (σ_s) contribute partially to the total conduction (σ_T),[21,31,32] as shown in Equation 5.1. The film thickness, t, is considered to extract the bulk conductivity. We assume that the carriers behave as a free electron gas. Thus, in the presence of a magnetic and an electric field, the conductivity can be represented by Equation 5.2.[33]

$$\sigma_T = (\sigma_{bulk} \times t) + \sigma_S \tag{5.1}$$

$$\sigma_T(B) = \frac{e\, n_b\, \mu_b}{1+ (\mu_b B)^2} + \frac{e\, n\, \mu_s}{1+ (\mu_s B)^2} \tag{5.2}$$

where n_b (n_s) is the concentration of and μ_b (μ_s) is the mobility of bulk (surface) carriers. B is the magnetic field applied in the z-direction and e is Coulomb's charge (1.6×10^{-19} C). For a layer containing more than one type of carrier, the conductivity-tensor components can be expressed as a sum over the m species present within the multicarrier system:[21,32]

$$\sigma_{xx}(B) = \sum_{i=1}^{m} \frac{e\, n_i\, \mu_i}{1+ (\mu_i B)^2} \tag{5.3}$$

$$\sigma_{xy}(B) = \sum_{i=1}^{m} S_i \frac{e\, n_i\, \mu_i^2 B}{1+ (\mu_i B)^2} \tag{5.4}$$

where n_i and μ_i are the concentration and mobility of the i-th carrier species, respectively. In this case, we adopt the convention that S_i is +1 for electrons and -1 for holes, as shown by the positive values of σ_{xy} in Figure 5.7. Figure 5.7 shows the measured conductivities (solid line) as a function of magnetic field for the (a) 30 nm, x = 0.58, (b) 30nm, x = 0.64, and (c) 18nm, x = 0.64 $(Bi_{1-x}Sb_x)_2Te_3$ films. Magneto-transport measurements on the 6 nm film were not successful; however, transport measurements, presented in an earlier report[18] showed the Hall/Seebeck n/p anomaly. While good agreement is apparent between the measurement (solid lines) and the iterative fit (dashed lines) for σ_{xy}, the simulated σ_{xx} is slightly overestimated as shown in Figure 5.7. The extracted carrier densities and mobilities from the iterative fit are presented in Table 5.2.

Film thickness (nm)	**x**	μ_e ($cm^2/V*s$)	n_e (cm^{-2})	μ_p ($cm^2/V*s$)	n_p (cm^{-2})
6	0.68	--	--	--	--
18	0.64	723	$4.2x10^{13}$	752	$3.1x10^{13}$
30	0.64	552	$2.7x10^{12}$	358	$3.3x10^{12}$
30	0.58	1241	$7.6x10^{12}$	746	$8.4x10^{12}$

Table 5.2 Extracted carrier densities and mobilities assuming a two-carrier transport system.

5.7 Discussion

For all $(Bi_{1-x}Sb_x)_2Te_3$ films, $0.58 \leq x \leq 0.68$, Hall measurements reveals a negative Hall coefficient (n-type conduction), similar to previous studies.[18] However, STS reveals p-type conduction for $(Bi_{1-x}Sb_x)_2Te_3$ films with $x > 0.6$. This n/p anomaly has been previously observed, where room-temperature Hall/Seebeck data indicated n-type/p-type conduction for $(Bi_{1-x}Sb_x)_2Te_3$ films with $x > 0.6$.[19,20] It was proposed that n-type TSSs dominate magnetoelectric transport (Hall), whereas p-type bulk states dominate the thermoelectric transport (Seebeck).[19] Our data suggests that there are at least two channels of conduction, which may contribute to the n/p discrepancy between Hall/Seebeck or Hall/STS measurements. As the x composition (film thickness) increase (decrease) from x = 0.58 to 0.68 (30 nm to 18 nm), the mobility difference between the two channels decreases, making the channels less resolvable. For the 18 nm thick film, due to the similar mobilities and carrier densities for the two channels, determining the dominant carrier type is challenging.

Equation 5.4 carries the information about the carrier type, as represented by S_i in the equation. We initially adopted the convention that $S_i = +1$, as shown by the positive values of σ_{xy} in Figure 5.7. After substituting the extracted values in Table 5.2 into Equation 5.4 for m = 2, we find that the fitted value for σ_{xy} at B = 14 T equals that of the experimental value when the higher mobility channel (i.e., $i = 1$) is positive, and the lower mobility channel (i.e., $i = 2$) is negative, enabling a clear separation of two conduction channels. Thus, the positive higher mobility channel (i.e., $i = 1$) is electron-dominated, and the negative lower mobility channel (i.e., $i = 2$) is hole-dominated. Assuming that the higher

mobility channel is dominated by TSSs, we conclude that surface transport is dominated by electrons and bulk transport is dominated by holes.

For the 30 nm (x = 0.58) film, STS shows n-type conduction, in good agreement with the higher mobility channel from the two-band model. For the 18 nm (x = 0.64) film, STS shows p-type conduction, in good agreement with the higher mobility hole channel from the two-band model. For the 30 nm (x = 0.64) film, STS show slightly p-type conduction, while the two-band model suggests a higher mobility electron channel. The discrepancy is likely due to effects of carrier compensation where the 30 nm (x = 0.64) film may contain combinations of Te_{Bi}, V_{Sb}, and Sb_{Te}.[15]

Furthermore, the shift in E_D from below to above E_F, shown in Figure 5.6 for the 30 nm (x = 0.58) (green) and 30 nm (x = 0.64) (blue) $(Bi_{1-x}Sb_x)_2Te_3$ films, respectively, indicates a change in carrier type from electrons to holes, with the crossover at $x \approx 0.6$. Our results suggest that increasing the Sb composition in $(Bi_{1-x}Sb_x)_2Te_3$ films shifts E_D in n-type *Bi-rich* films away from VBE towards the middle of the band gap. This trend is in agreement with ARPES and STS measurements.[15,25] Both E_F and E_D are located within the bulk band gap, indicating bulk insulating behavior with accessible TSSs. No distinct surface state spectra were observed for 6 nm and 18 nm films.

5.8 Summary and conclusions

In summary, we use STM and STS of $(Bi_{1-x}Sb_x)_2Te_3$ alloys to probe both the Fermi level, E_F, and Dirac point, E_D, located inside the bulk bandgap, indicating bulk-like insulating behavior with accessible TSSs. An increase in film thickness reveals a shift of the E_F from VBE towards the middle of the energy band gap, suggesting the introduction

n-type defects with increasing film thickness. For the n-type *Bi-rich* film (30 nm, x = 0.58), E_D is below E_F, while for the insulating *pn compensated* film (30 nm, x = 0.64), E_D is above E_F. The shift in E_D from below to above E_F indicates a change in carrier-type dominance from electrons to holes, with a n-type to p-type cross-over at $x \approx 0.6$. We interpret two-channel conduction in order to differentiate the charge carrier types for surface and bulk transport. Assuming that the higher mobility channel is dominated by TSSs, we conclude that surface transport is dominated by electrons and bulk transport is dominated by holes.

5.9 Figures

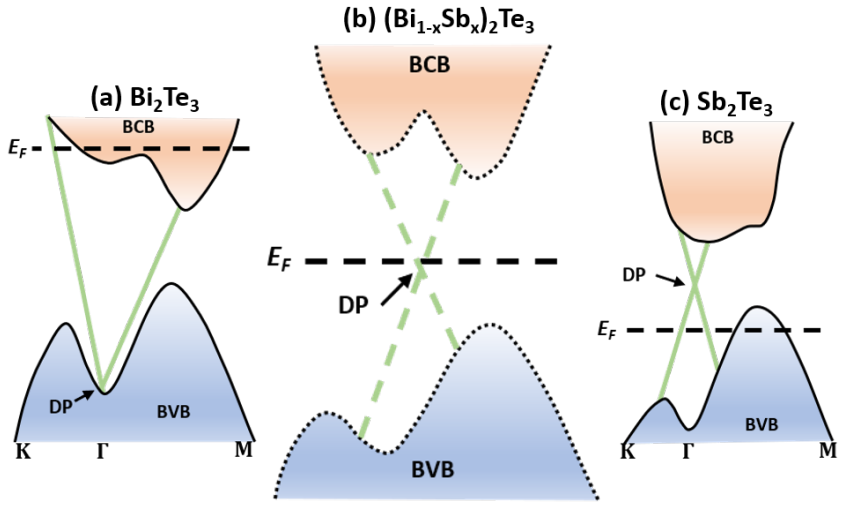

Figure 5.1 Schematic of electronic band structure for (a) Bi_2Te_3 and (c) Sb_2Te_3. For Bi_2Te_3, Te anti-site (Te_{Bi}) defects lead to n-type conduction and the Fermi level (E_F) is pinned with the bulk conduction band (BCB). For Sb_2Te_3, Sb vacancies (V_{Sb}) and Sb anti-site (Sb_{Te}) defects lead to p-type conduction and the Fermi level (E_F) is pinned with the bulk valence band (BVB). (b) Bi_2Te_3-Sb_2Te_3 alloys may allow for the shifting of E_F and Dirac point (DP) inside of the gap. Adapted from Refs. 13-16.

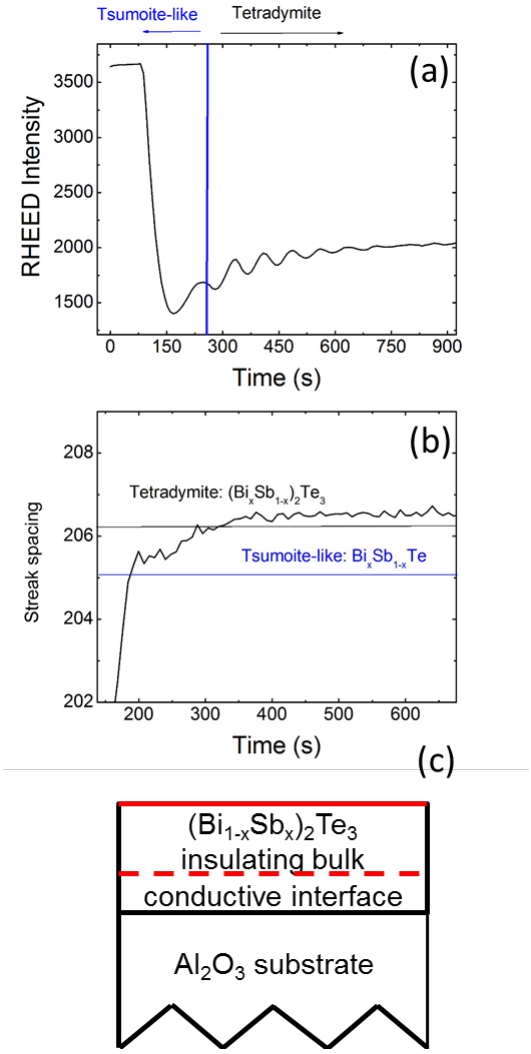

Figure 5.2 (a) RHEED intensity oscillations as a function of time and (b) an analysis of the streak spacing as a function of time. There is an increase in streak spacing around 275 s, corresponding to a decrease in the lattice constant which could indicate the presence of Bi intercalation resulting in a tsuomoite structure, giving way to the standard tetradymide structure later in the growth. (c) Cross-sectional view of the sample with the structure suggested by the electrical resistance and RHEED results. At the substrate/growth layer interface is a conductive layer, followed by an insulating layer of BiSbTe. The red lines indicate the topological surface states.

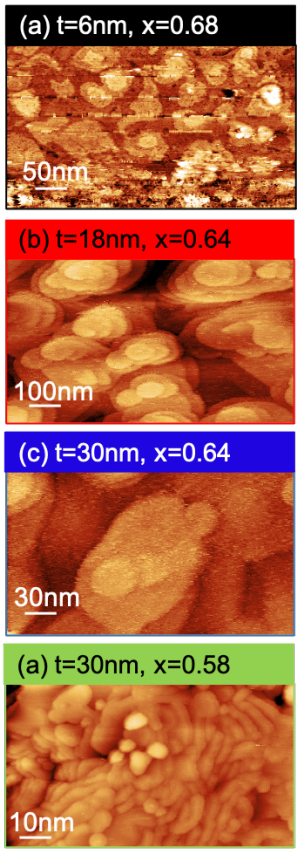

Figure 5.3 Large-scale STM images of the surface topography for (a) 6 nm (Δz = 15.5 nm) (b) 18 nm (Δz = 9.5 nm), (c) 30 nm (Δz = 9.8 nm), and (d) 30 nm (Δz = 15.8 nm) $(Bi_{1-x}Sb_x)_2Te_3$ films. For all samples, large terraces with 1 quintuple layer steps are observed, indicating high quality layer-by-layer growth of the Van der Waals bonded layers. (a) has been adapted and reprinted with permission from Ref. 20 (Copyright 2016, AIP).

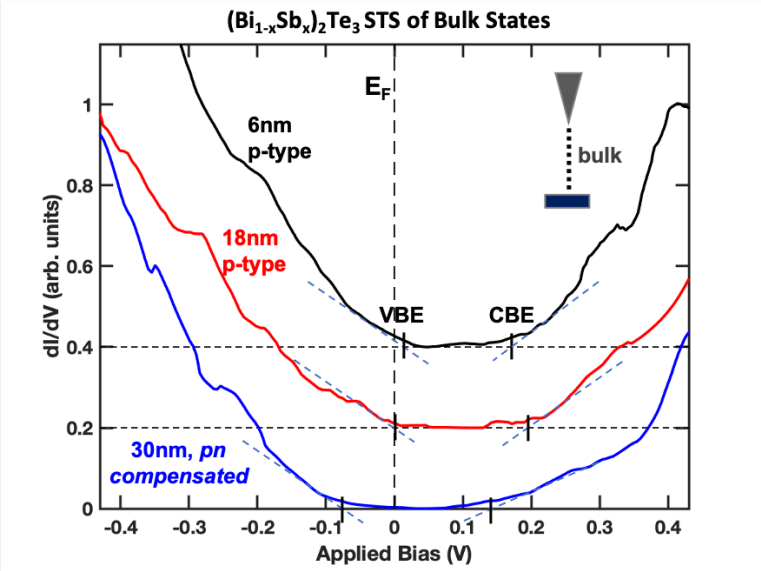

Figure 5.4 STS of bulk states: dI/dV as a function of bias voltage, corresponding to the energy relative to the Fermi level for the 6 nm, x = 0.68 (black), 18 nm, x = 0.64 (red), and 30 nm, x = 0.64 (blue) $(Bi_{1-x}Sb_x)_2Te_3$ films. As film thickness increases from 6 nm, the Fermi level shifts from the valence band edge (VBE) towards the conduction band edge (CBE), likely due to the introduction of n-type defects through the growth of additional monolayers.

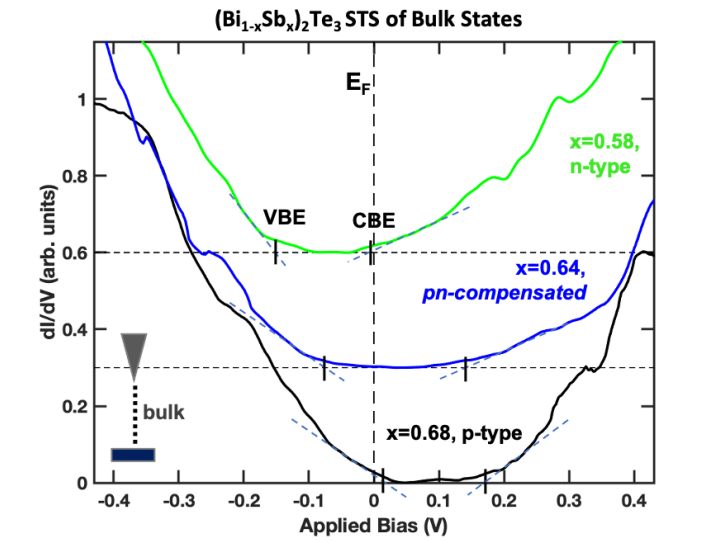

Figure 5.5 STS of bulk states: dI/dV as function of bias voltage for 30 nm, x = 0.58 (green) 30 nm, x = 0.64 (blue), and 6nm, x = 0.68 (black) $(Bi_{1-x}Sb_x)_2Te_3$ films, x = 0.58 (green), x = 0.64 (blue), and x = 0.68 (black) corresponding to the energy relative to the Fermi level. As the composition increases, the Fermi level shifts from the conduction band edge (CBE) in the x = 0.58 film towards the valence band edge (VBE) of the x = 0.64 film, revealing a transition from n-type to pn carrier compensated to p-type.

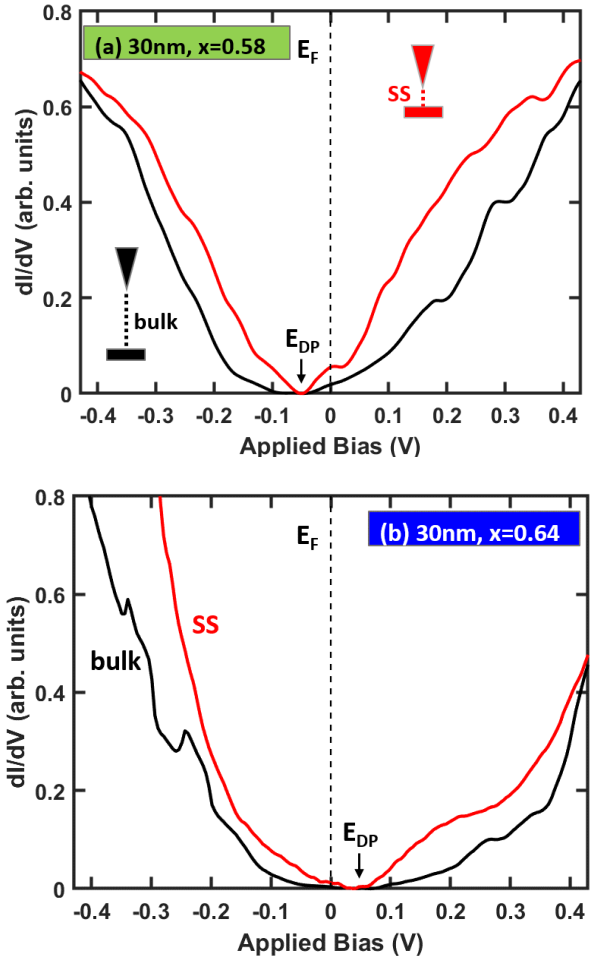

Figure 5.6 dI/dV of 30nm $(Bi_{1-x}Sb_x)_2Te_3$ films for (a) x = 0.58 and (b) x = 0.64 as a function of bias voltage, corresponding to the energy relative to the Fermi level, E_F, revealing two distinct states of surface and bulk conduction. The bulk conduction (black) reveals an effective band gap of 0.19 (0.21) ± 0.10 eV for x = 0.58 (x = 0.64). The surface state curves (red) were taken with a lower tunneling impedance, with the Dirac point, E_{DP}, located between E_F and the valence band edge for $(Bi_{1-x}Sb_x)_2Te_3$ films, x = 0.58 and between E_F and the conduction band edge for $(Bi_{1-x}Sb_x)_2Te_3$ films, x = 0.64.

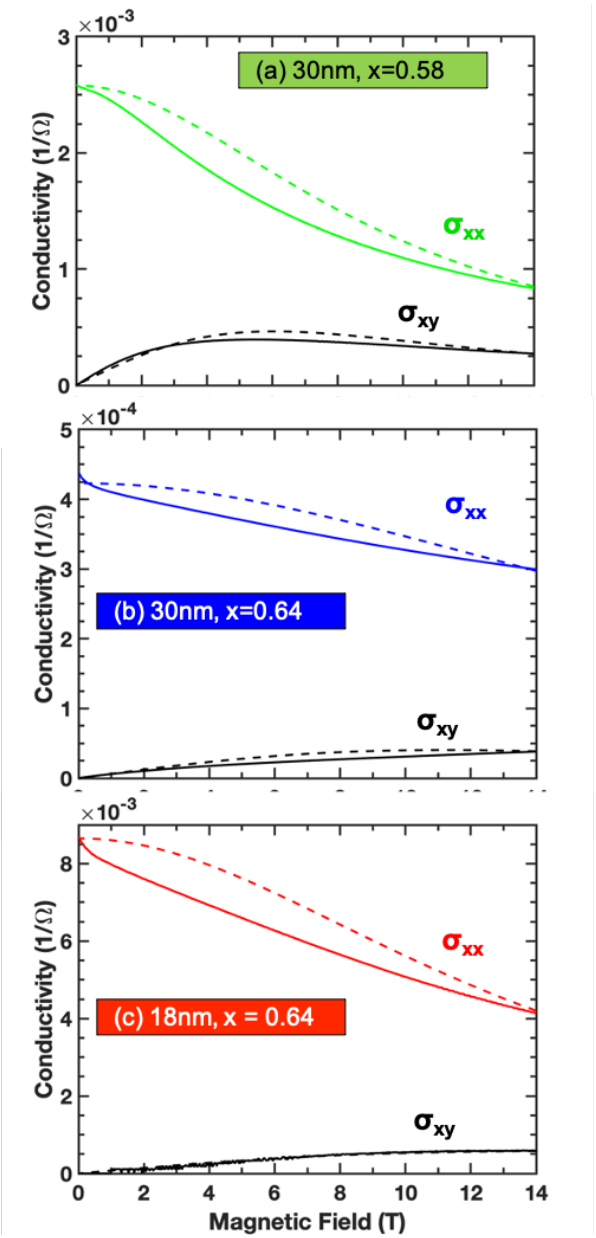

Figure 5.7 Measured conductivities (solid line) as a function of magnetic field for the (a) 30 nm (x = 0.58), (b) 30nm (x = 0.64), and (c) 18nm (x = 0.64) $(Bi_{1-x}Sb_x)_2Te_3$ films. The dashed lines represent the simulated conductivities, assuming the conductivity consist of two carrier types.

5.10 References

[1] H. Zhang, C.-X. Liu, X.-L. Qi, X. Dai, Z. Fang, and S.-C. Zhang, "Topological Insulators in Bi_2Se_3, Bi_2Te_3 and $Sb_2Te_3$with a Single Dirac Cone on the Surface", Nature Phys. 5, 438 (2009).

[2] Y. Xia, D. Qian, D. Hsieh, L. Wray, A. Pal, H. Lin, A. Bansil, D. Grauer, Y.S. Hor, R.J. Cava, and M.Z. Hasan, "Observation of a Large-gap Topological-insulator Class with a Single Dirac Cone on the Surface", Nature Physics, 5, 398 (2009).

[3] D. Hsieh, Y. Xia, D. Qian, L. Wray, J. H. Dil, F. Meier, J. Osterwalder, L. Patthey, J. G. Checkelsky, N. P. Ong, A. V. Fedorov, H. Lin, A. Bansil, D. Grauer, Y. S. Hor, R. J. Cava and M. Z. Hasan, "A Tunable Topological Insulator in the Spin Helical Dirac Transport Regime", Nature, 460, 1101 (2009).

[4] J. Maciejko, T.L. Hughes, and S.C. Zhang, "The Quantum Spin Hall Effect", Annu. Rev. Condens. Matter Phys. 2, 31 (2011).

[5] P. Roushan, J. Seo, C.V. Parker, Y.S. Hor, D. Hsieh, D. Qian, A. Richardella, M.Z. Hasan, R.J. Cava, and A. Yazdani, "Topological Surface States Protected from Backscattering by Chiral Spin Texture", Nature (London) 460, 1106 (2009).

[6] T. Zhang, P. Cheng, X. Chen, J.-F. Jia, X. Ma, K. He, L. Wang, H. Zhang, X. Dai, Z. Fang, X. Xie, and Q.-K. Xue, "Experimental Demonstration of Topological Surface States Protected by Time-Reversal Symmetry", Phys. Rev. Lett. 103, 266803 (2009).

[7] J.E. Moore, "The Birth of Topological Insulators", Nature, 464, 194 (2010).

[8] G.R. Miller and C.Y. Li, "Evidence for the Existence of Anti-structure Defects in Bismuth Telluride by Density Measurements", J. Phys. Chem. Solids, 26, 173 (1965).

[9] D. West, Y. Y. Sun, H. Wang, J. Bang, and S.B. Zhang, "Native Defects in Second-generation Topological Insulators: Effect of Spin-orbit Interaction on Bi_2Se_3", Phys. Rev. B 86, 121201(R) (2012).

[10] P. Lošták, S. Karamazov, and J. Horák, "Antisite Defects in $BiSbTe_3$ Crystals Doped with Indium Atoms", Phys. Stat. Sol. (a) 143, 271 (1994).

[11] J. Horák, K. Čermák, and L. Koudelka, "Energy Formation of Antisite Defects in Doped Sb_2Te_3 and Bi_2Te_3 Crystals", J. Phys. Chem. Solids 47, 805 (1986).

[12] D.O. Scanlon, P.D.C. King, R.P. Singh, A.D.L. Torre, S.M. Walker, G. Balakrishnan, F. Baumberger, and C.R.A. Catlow, "Controlling Bulk Conductivity in Topological Insulators: Key Role of Anti-Site Defects", Adv. Mater. 24, 2154 (2012).

[13] Y.P. Jiang, Y.Y. Sun, M. Chen, Y.L. Wang, Z. Li, C.L. Song, K. He, L.L. Wang, X. Chen, Q.K. Xue, X.C. Ma, and S.B. Zhang, "Fermi-Level Tuning of Epitaxial Sb_2Te_3 Thin Films on Graphene by Regulating Intrinsic Defects and Substrate Transfer Doping", Phys. Rev. Lett. 108, 066809 (2012).

[14] N. Peranio, M. Winkler, M. Dürrschnabel, J. König, O. Eibl, "Assessing Antisite Defect and Impurity Concentrations in Bi_2Te_3 Based Thin Films by High-Accuracy Chemical Analysis", Adv. Funct. Mater. 23, 4969 (2013).

[15] J. Zhang, C.Z. Chang, Z. Zhang, J. Wen, X. Feng, K. Li, M. Liu, K. He, L. Wang, X. Chen, Q.K. Xue, X. Ma, and Y. Wang, "Band structure Engineering in $(Bi_{1-x}Sb_x)_2Te_3$ Ternary Topological Insulators", Nat. Commun. 2, 574 (2011).

[16] Y.L. Chen, J. G. Analytis, J.-H. Chu, Z.K. Liu, S.-K. Mo, X L. Qi, H.J. Zhang, D.H. Lu, X. Dai, Z. Fang, S.C. Zhang, I.R. Fisher, Z. Hussain, Z.-X. Shen, "Experimental Realization of a Three-Dimensional Topological Insulator, Bi_2Te_3", Science, 325, 178, (2009).

[17] D. Hsieh, Y. Xia, D. Qian, L. Wray, F. Meier, J.H. Dil, J. Osterwalder, L. Patthey, A.V. Fedorov, H. Lin, A. Bansil, D. Grauer, Y.S. Hor, R.J. Cava, and M.Z. Hasan, "Observation of Time-Reversal-Protected Single-Dirac-Cone Topological-Insulator States in Bi_2Te_3 and Sb_2Te_3", PRL, 103, 146401 (2009).

[18] W. Liu, V. Stoica, H. Chi, L. Endicott, and C. Uher, "Epitaxial Growth and Improved Electronic Properties of $(Bi_{1-x}Sb_x)_2Te_3$ Thin Films on Sapphire (0001) Substrates: The Influence of Sb Content and Annealing", J. Alloys and Comp, 647, 50 (2015).

[19] J. Zhang, X. Feng, Y. Xu, M. Guo, Z. Zhang, Y. Ou, Y. Feng, "Disentangling the Magnetoelectric and Thermoelectric Transport in Topological Insulator Thin Films", Phys. Rev. B. 91, 075431 (2015).

[20] W. Liu, H. Chi, J. C. Walrath, A.S. Chang, V. A. Stoica, L. Endicott, X. Tang, R.S. Goldman, and C. Uher, "Origins of Enhanced Thermoelectric Power Factor in Topologically Insulating $Bi_{0.64}Sb_{1.36}Te_3$ Thin Films", Appl. Phys. Lett. 108, 043902 (2016).

[21] J. Antoszewski, D.J. Seymour, and L. Faraone, "Magneto-Transport Characterization Using Quantitative Mobility-Spectrum Analysis", J. Elect. Mat., 24, 9 (1995).

[22] W. Liu, L. Endicott, V.A. Stoica, H. Chi, R. Clarke, and C. Uher, "High-quality Ultra-flat $BiSbTe_3$ Films Grown by MBE", J. Crys. Growth 410, 23 (2015).

[23] Y. Ando, "Topological Insulator Materials", J. Phys. Soc. Jpn. 82, 102001 (2013).

[24] S.V. Eremeev, M.M. Otrokov, and E.V. Chulkov, "New Universal Type of Interface in the Magnetic Insulator/Topological Insulator Heterostructures", Nano. Lett. 18, 6521 (2018).

[25] T. Zhang, J. Ha, N. Levy, Y. Kuk, and J. Stroscio, "Electric-Field Tuning of the Surface Band Structure of Topological Insulator Sb_2Te_3 Thin Films", PRL 111, 056803 (2013).

[26] Z. Chen, L. Zhao, K. Park, T.A. Garcia, M.C. Tamargo, and L. Krusin-Elbaum, "Robust Topological Interfaces and Charge Transfer in Epitaxial Bi2Se3/II-VI Semiconductor Superlattices", Nano Lett. 15, 6365 (2015).

[27] L. He, X. Kou, M. Lang, E.S. Choi, Y. Jiang, T. Nie, W. Jiang, Y. Fan, Y. Wang, F. Xiu, and K.L. Wang, "Evidence of the Two Surface States of $(Bi_{0.53}Sb_{0.47})_2Te_3$ Films Grown by Van der Waals Epitaxy", Sci. Rep. 3, 3406 (2013).

[28] D. West, Y.Y. Sun, H. Wang, J. Bang, and S.B. Zhang, "Native defects in second-generation topological insulators- Effect of spin-orbit interaction on Bi_2Se_3", Phys. Rev. B 86, 121201(R) (2012).

[29] Y. Jiang, Y. Wang, M. Chen, Z. Li, C. Song, K. He, L. Wang, X. Chen, X. Ma, and Q.K. Xue, "Landau Quantization and the Thickness Limit of Topological Insulator Thin Films of Sb_2Te_3", Phys. Rev. Lett.108, 016401 (2012).

[30] X. He, H. Li, L. Chen, and K. Wu, "Substitution-induced Spin-splitted Surface States in Topological Insulator $(Bi_{1-x}Sb_x)_2Te_3$", Sci. Rep. 5, 8830 (2015).

[31] Z. Dziuba and M. Górska, "Analysis of the Electrical Conduction using an Iterative Method", J. Phys. III France 2, 2, 99 (1992).

[32] W.A. Beck and J.R. Anderson, "Determination of Electrical Transport Properties using a Novel Magnetic Field-dependent Hall Technique", J. App. Phys. 62, 541 (1987).

[33] Y. Murayama, "Mesoscopic Systems: Fundamentals and Applications, Appendix H Calculation of Conductivity Tensor in a Magnetic Field", Wiley Berlin, 2001, pp.217-221.

Chapter 6

Summary and Suggestions for Future Work

6.1 Summary

This dissertation presents investigations of local nanoscale morphologies and electronic properties in semiconductor (2D) thin films and heterostructures, combining both experimental and computational approaches including local electrode atom probe (LEAP) tomography, electron microscopy, photoluminescence (PL), scanning tunneling microscopy/spectroscopy (STM/S), magneto-transport measurements, and Poisson-Schrödinger band structure calculations. In this chapter, a summary of the results is presented, followed by suggestions for future work.

6.1.1 Examining stoichiometry and microstructure in III-V alloys with LEAP

In Chapter 3, we demonstrated an approach to examine apparent stoichiometry in GaAs-based alloys and nanostructures using local electrode atom probe (LEAP) tomography, in conjunction with Rutherford Backscattering Spectrometry (RBS) and high-resolution x-ray diffraction (HRXRC). Using the LEAP conditions identified for achievement of near-stoichiometry in GaAs, we investigate local N and Bi compositions in GaAsNBi alloys and local Si concentrations in the vicinity of Si-doped InAs/GaAs QD superlattices. For the GaAsNBi alloys, LEAP-determined average Bi compositions

correlate with those determined using RBS. These are the first known studies that use LEAP to directly measure N and Bi compositions for GaAsNBi films. For Si-doped InAs/GaAs QD superlattices, 3D LEAP data reveals laterally and vertically inhomogeneous Si incorporation, with clusters of Si throughout the layers. Using the local In, Ga, As, and Si compositions from 3D LEAP data as input into Schrodinger-Poisson simulations,[1] we find that electrons are predicted to be localized near both the QDs and the Si clusters. This study presents a wholistic view of evaporation behaviors present in a range of III-V materials that have been investigated in the Goldman group using LEAP, including extensions of work previously presented by T. Jen[2] and J. Walrath.[3] This work has valuable implications for nanoscale characterization for device structures and for electronic structure calculations.

6.1.2 GaSb QDs and QD-rings

In Chapter 4, we determined the distribution of compositions within Ga(As)Sb quantum dots (QDs), clusters, and circular arrangements of smaller QDs, termed QD-rings (QDRs) using LEAP. Sizes, shapes, and compositional gradients are used as input into self-consistent Schrödinger-Poisson simulations to compute confinement energies for individual nanostructure types. The computed confinement energies and the measured photoluminescence emission energies increase from QDs to QD-rings to 2D layers, enabling direct association of nanostructure morphologies with the optical properties of the GaSb/GaAs multilayers. This is the first known work that uses measured compositional gradients as input into 8 x 8 $\mathbf{k}\cdot\mathbf{p}$ calculations for Ga(As)Sb/GaAs nanostructures, opening

opportunities for tailoring emission energies for near to far-infrared optoelectronics by varying the QD morphology.

6.1.3 Identification of topological surface states in $(Bi_{1-x}Sb_x)_2Te_3$ alloy films

In Chapter 5, we investigated the bulk and local electronic states in $(Bi_{1-x}Sb_x)_2Te_3$ alloys using scanning tunneling spectroscopy (STS) and magneto-transport measurements. STS of $(Bi_{1-x}Sb_x)_2Te_3$ revealed both the Fermi level, E_F, and Dirac point, E_D, located inside the bulk bandgap, indicating bulk-like insulating behavior with accessible topological surface states (TSSs). E_D is below E_F for the n-type *Bi-rich* film (30 nm, x = 0.58) and is above E_F in insulating, *pn compensated* films (30 nm, x = 0.64), revealing a transition from n-type to p-type conduction at $x \approx 0.6$. We use a two-channel analysis of MR data to differentiate the charge carrier types for surface and bulk transport; we conclude that surface transport is dominated by electrons and bulk transport is dominated by holes. Prior to this work, direct detection of topological surface states in BiSbTe systems has been achieved only for T<10 K. However, for device applications, room-temperature identification of TSSs is needed. This work demonstrates the first direct measurement of TSSs using STS at room temperature for any material.[3]

6.2 Suggestions for future work

Suggestions for future work, including preliminary data, are presented in the following sections. These projects include investigations of the local band alignment in GaAsNBi/GaAs QWs using XSTM/S, combined with LEAP and nextnano; XSTM/S

investigations of band alignments in IMF and SK GaSb QDs; and the study of strain in Ga(As)Sb/GaAs QDs versus QDRs using XSTEM and Geometric Phase Analysis (GPA).

6.2.1 Local band alignment in GaAsNBi/GaAs QWs (XSTM, LEAP, nextnano)

As discussed in Section 1.2, a promising feature predicted for GaAsNBi alloys is the opportunity to independently tune the conduction band offset (CBO) and valence band offset (VBO) over a wide range in semiconductor heterostructures.[4] According to the (valence) band anti-crossing model, N (Bi) primarily lowers (raises) the conduction (valence) band edge,[5,6] forming a type-I band alignment at a GaAs/GaAsNBi interface. This suggests that the CBO is primarily controlled by the N fraction and the VBO by the Bi fraction. Consequently, GaAsNBi is predicted to enable confinement of electrons and holes in GaAs-based double-heterostructure laser diodes.[7] Furthermore, a strain-balanced type-II GaAsN/GaAsBi superlattice structure has been proposed to extend the accessible wavelength range for solar cells and infrared photodetectors.[8,9] Two methods for investigating the band offsets in GaAsNBi are suggested: 1) A local investigation of the band alignment at the GaAsNBi/GaAs interface using XSTM/S, combined with using self-consistent Schrödinger-Poisson simulations to calculate the expected quantized energy levels for each QW. 2) An investigation of the band offsets using capacitance-voltage (C-V) measurements, along with Schrödinger-Poisson simulations to model C-V measurements.

Figure 6.1 shows examples of the sample structures used for XSTM: (a) GaAs/GaAsNBi/GaAs multiple quantum well (MQW) and (b) a single GaAs/GaAsNBi/GaAs quantum well (QW) The goal is to measure the energies of the

conduction band edge (CBE) and valence band edge (VBE) in the GaAsNBi using STS, as described in Section 2.7. Such measurement will reveal which band, E_c or E_v, dominates in shifting the band alignment.[10] XSTM experiments were performed by the author for GaAsNBi samples presented in Appendix D. GaAsNBi layers were observed using XSTM (not shown), however STS measurements have not yet been successfully performed. Therefore, we suggest future investigations of the GaAsNBi/GaAs band alignment using XSTS.

Furthermore, self-consistent Schrödinger-Poisson simulations can be used to calculate the expected quantized energy levels for each GaAsNBi/GaAs QW. Results can be correlated with STS results to deduce strain and compositional influences on the band alignment. A model was presented in Chapter 4 to calculate the expected quantized energy levels in GaSb/GaAs QDs using nextnano.[11] This model can be modified for GaAsNBi/GaAs QWs. We present a possible limitation for such simulations using nextnano and provide two approaches to overcome this limitation. To date, material database within nextnano does not include parameters for ternary and quaternary alloys based upon GaBi, such as $GaAs_{1-x}Bi_x$ and $GaAs_{1-x-y}N_xBi_y$. This limitation may be circumvented by defining a new material, "$GaAs_{1-x}Bi_x$", using theoretically- and experimentally-determined properties that are currently present in the literature.[12-15] Figure 6.2 presents the energies versus Bi composition for a GaAs/GaAsBi (10nm) /GaAs quantum well using newly defined $GaAs_{1-x}Bi_x$ material within nextnano. Here, we assumed a 0.632 nm[16] lattice constant for GaBi. While the transition energy for the spin orbital (SO) band agrees well with photoreflectance measurements,[13] further parameter modifications within nextnano are needed for calculations of the heavy hole (HH) and light hole (LH)

transition energies. It is clear that the effective mass for the SO band differs from that of the HH and LH due the different slopes. For this, we suggest modifying parameters for the GaAs/$GaAs_{1-x}Bi_x$ valence band offset and effective masses within nextnano.

After the band structure of $GaAs_{1-x}Bi_x$ is verified using photoreflectance measurements from literature,[12-15] a new material "$GaAs_{1-x-y}N_xBi_y$", can subsequently be created within nextnano, using both pre-defined $GaAs_{1-x}N_x$ and "$GaAs_{1-x}Bi_x$" materials as constituents. Furthermore, N and Bi compositions from LEAP, RBS, and/or XRD/RADs can be into input into 8 x 8 Schrödinger Poisson simulations to directly calculate effective CBEs, VBEs, and quantized energy levels for varying N and Bi compositions. Calculations can be compared with local probe measurements from XSTM to provide a more detailed understanding of the influence of strain and composition on the local band alignments in GaAsNBi/GaAs QWs. Furthermore, the successful development of the "$GaAs_{1-x-y}N_xBi_y$" material opens opportunity for modeling a range of GaAsNBi-related heterostructures, an example of which is presented in the following section.

6.2.2 Band alignment in IMF/SK GaSb QDs

We investigated the influence of strain and on the band alignment in GaSb/GaAs QDs systems. Conventional Model Solid Theory,[17] which relates the average atomic electrostatic potential to the vacuum level, predicts a type-I band alignment for unstrained GaSb/GaAs heterostructures (7% misfit). Band edge calculations predicts type I (type II) offsets for unstrained (strained) GaSb/GaAs quantum dots (QDs).[18] However, there is no experimental proof for these predictions. Our goal is to use advantages of XSTM/S to locally measure the band edge energies near GaSb/GaAs QD interfaces. For this study, we

modeled "strain" using two growth modes for GaSb/GaAs QDs – Stranki-Krastanow (SK) and Interfacial misfit (IMF). We assume that SK GaSb QDs are highly strained and that IMF GaSb QDs are strain-relaxed due to their respective formation mechanisms.[19] For example, SK QDs are typically smaller, hemispherical-shaped, and without dislocations. SK GaSb QDs can be grown using low III/V BEP ratio (~1). On the other hand, IMF QDs are typically larger and elongated and can be grown using a higher III/V BEP (~10). IMF GaSb QDs are typically accompanied by misfit dislocations and quantum dot rings, both which are results of strain-relief mechanisms. Thus, we consider IMF GaSb QDs to be a strain-relaxed or strain-free system.

We designed a heterostructure that consisted of both IMF and SK GaSb/GaAs QDs to improve the chances of imaging and performing STS of both QD types in one experiment. These samples were recently grown by Balakrishnan's group at the University of New Mexico and are listed in Appendix D. XSTM images of 3ML and 4ML SK QDs and IMF QDs are shown in Figure 6.5(a) and (b), respectively. Finally, STS was used to perform direct measurements of the local band edges at the core and near the edges of SK and IMF QDs to determine the local band alignments (not shown) for each QD type. This work provides a method of experimentally testing band-edge predictions for strain vs. strain-relaxed GaSb/GaAs QDs.

6.2.3 Quantifying strain in GaSb QDs and QD-rings

We discussed a detailed analysis of structural properties of the GaSb QDs, QD-rings, and clusters in Chapter 4. Large-scale STEM images reveal Sb segregation for some of the nanostructures,[11] as denoted by the arrows in Figure 6.4. This segregation of Sb is

likely a part of a strain relief mechanism, where Sb diffuses into the GaAs spacer regions and in some cases in the layers above. Furthermore, defects or dislocations may be present in the structure, which are common in GaSb QD systems: Sb may along the path of the dislocations to relieve the compressive strain of being confined to the nanostructures. While STEM images hint at the possibility of 60˚ misfit dislocations, the dark contrast in HAADF images in Figure 6.4 might be due to local variations in Z values. For future work, we suggest using Geometric Phase Analysis (GPA)[20] to quantify the strain fields around each of the QDs, QD-rings, and clusters, as shown in Figure 6.5 for an InAs QD.[21] GPA uses Fast Fourier transform algorithms to calculate lattice distortions on the order ~0.5nm. Differences in strain fields around the individual nanostructure types may give further insight into their formation mechanisms, which have been proposed to be strain-induced.[22-24] Furthermore, components of the strain tensors (e_{xx}, e_{xy}, e_{yx}, e_{yy}) can be used as experimental input into band structure calculations to allow for more realistic determination of electronic properties.

6.3 Figures

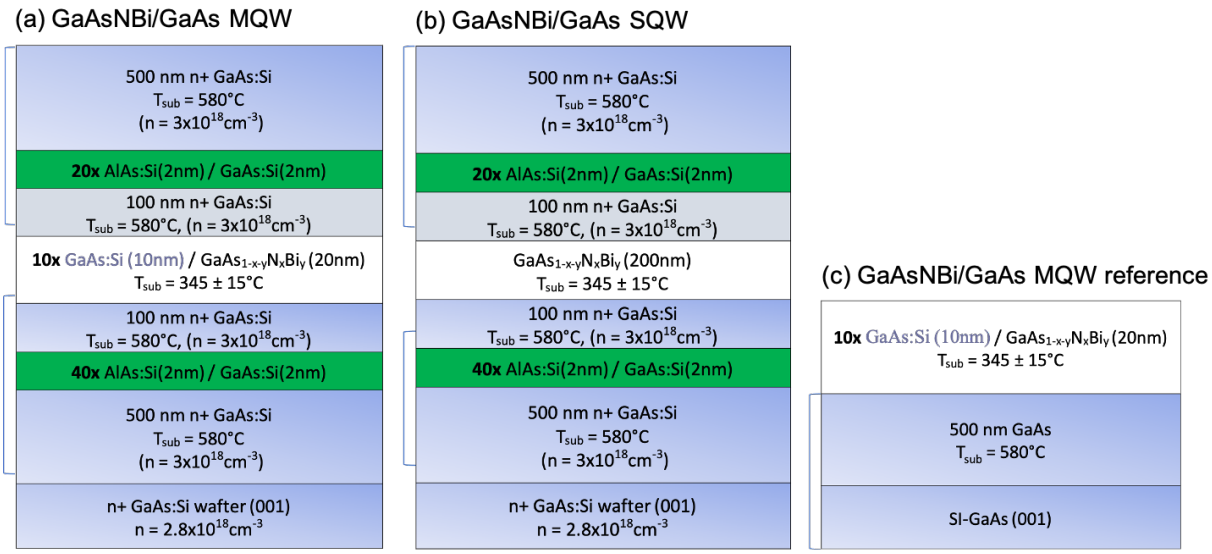

Figure 6.1 Schematics of the structures for (a) GaAsNBi/GaAs multiple quantum well (MQW), (b) GaAs/GaAsNBi/GaAs single quantum well (SQW) used in cross-sectional scanning tunneling microscopy/spectroscopy (STM/STS) measurements, along with (b) GaAsNBi/GaAs MQW reference, commonly used for x-ray diffraction (XRD). Layers in green indicated Si-doped AlAs/GaAs marker layers for STM.

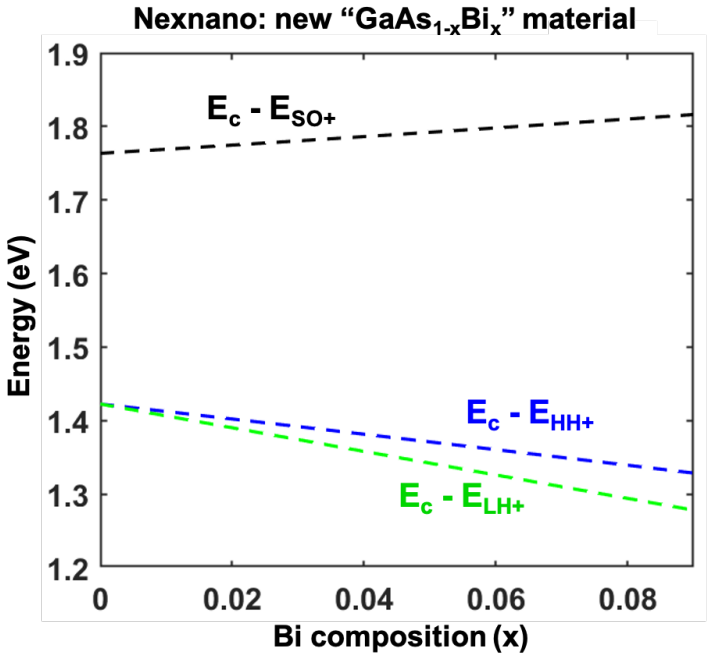

Figure 6.2 Transition energy values for the heavy hole (E_g^{HH+}), light hole (E_g^{LH+}), and spin-orbital splitting (E_g^{SO+}) bands in the newly defined $GaAs_{1-x}Bi_x$ material within nextnano for $0.0 < x < 0.09$. Transition energies are represented as the difference between the conduction band and the respective valence bands obtained using 8 x 8 band Schrödinger-Poisson calculations within nextnano. While the transition energy for the spin orbital (SO) band agrees well with photoreflectance measurements,[13] further parameter modifications (i.e., valence band offset and effective mass values) within nextnano are needed for calculations of the heavy hole (HH) and light hole (LH) transition energies.

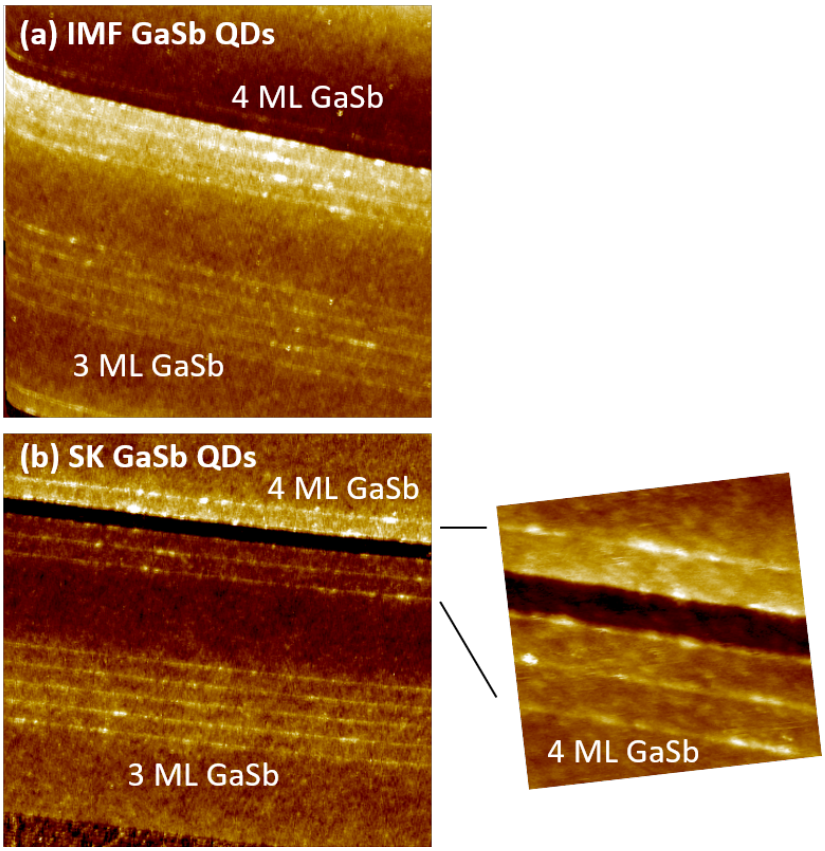

Figure 6.3 Constant-current XSTM topography images of (a) interfacial misfit (IMF) and (b) Stanski-Kranstanow (SK) GaSb/GaAs QDs. Images were obtained with a sample bias of ±2 V, tunneling setpoint current of 80 pA, and tip height (Δz) < 1nm. Bright and dark regions correspond to the GaSb QD and GaAs matrix, respectively.

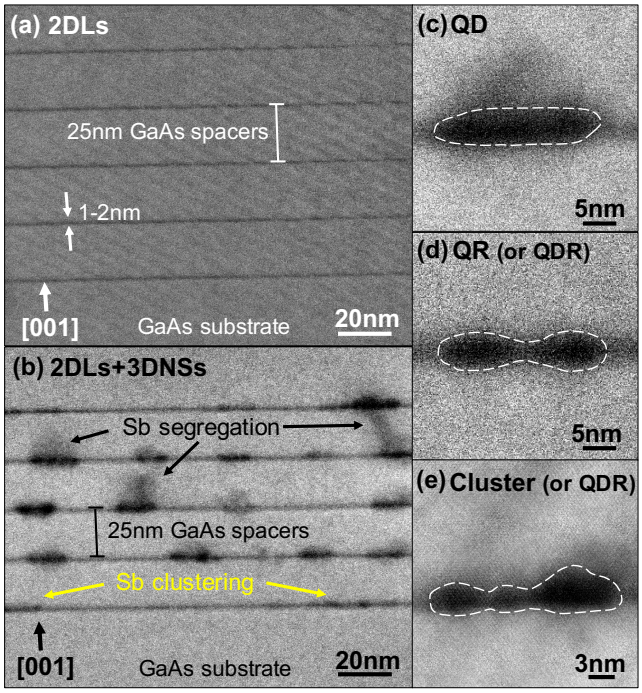

Figure 6.4 Cross-sectional scanning transmission electron micrographs of GaSb/GaAs multilayers containing (a) two-dimensional layers (2DLs) and (b) GaSb 2D layers with 3D nanostructures (2DLs+3DNSs), with arrows depicting possible locations of Sb out-diffusion. Close-up views for the nanostructures are also shown: (c) GaSb QD, (d) GaSb QR/QDR, and (e) GaSb cluster/QDR. Reprinted with permission from Ref. 11. (Copyright 2020, AIP Publishing).

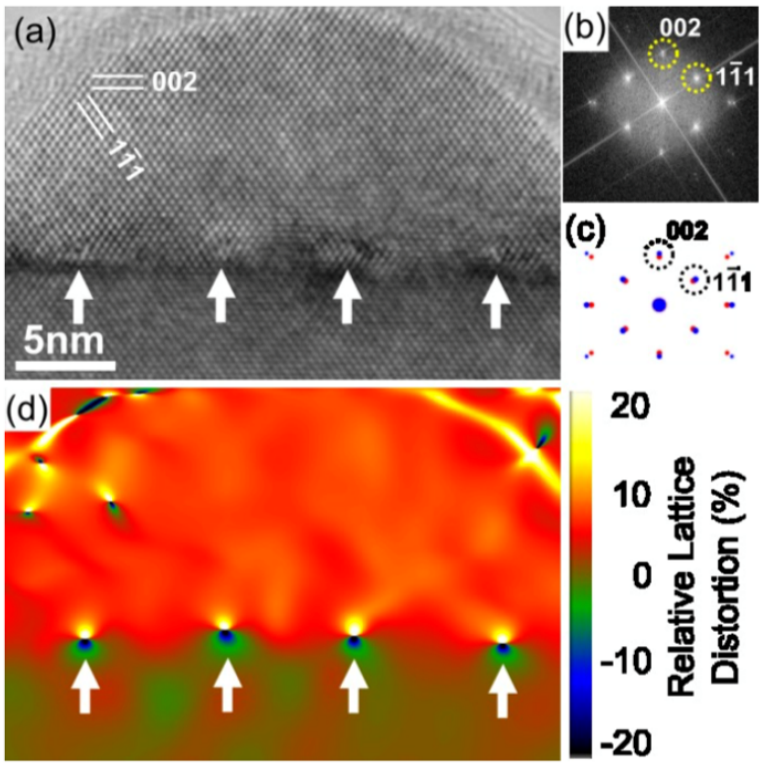

Figure 6.5 (a) HRTEM image of a crystalline InAs QD formed by Stranski-Krastanov mode (4ML In exposure), where misfit dislocations are indicated by vertical arrows. The corresponding fast Fourier transformation pattern is shown in (b), where the spots selected for geometric phase analysis (GPA) (circled with dashed lines) correspond to the <002> and <1-11> reflections, as indicated in the simulated diffraction pattern from both InAs (red) and GaAs (blue) shown in (c). The corresponding in-plane lattice distortion map from GPA of image (a) is shown in (d). Reprinted with permission from Ref. 21. (Copyright 2020, AIP Publishing).

6.4 References

[1] S. Birner, S. Hackenbuchner, M. Sabathil, G. Zangler, J. A. Majewski, T. Andlauer, T. Zibold, R. Morschl, A. Trellakis, and P. Vogl, "Modeling of Semiconductor Nanostructures with nextnano^3", Acta Phys. Pol. A 110, 111 (2006).

[2] T. Jen, "Ion Beam Analysis of Solute Incorporation in GaAsN and GaAsNBi Alloys", Ph.D. Thesis, University of Michigan, 2016, pp. 106-112.

[3] J. Walrath, "Probing the Band Structure and Local Electronic Properties of Low-Dimensional Semiconductor Structures", Ph.D. Thesis, University of Michigan, 2017, pp. 51-72.

[4] S.J. Sweeney and S.R. Jin, "Bismide-Nitride Alloys: Promising for Efficient Light Emitting Devices in the near- and Mid-Infrared", J. Appl. Phys. 113, 043110 (2013).

[5] W. Shan, W. Walukiewicz, J. Ager, E. Haller, J. Geisz, D. Friedman, J. Olson, and S. Kurtz, "Band Anticrossing in GaInNAs Alloys", Phys. Rev. Lett. 82, 1221 (1999).

[6] K. Alberi, O.D. Dubon, W. Walukiewicz, K.M. Yu, K. Bertulis, and A. Krotkus, "Valence Band Anticrossing in GaBixAs1−x", Appl. Phys. Lett. 91, 051909 (2007).

[7] C.A. Broderick, M. Usman, S.J. Sweeney, and E.P. O'Reilly, "Band Engineering in Dilute Nitride and Bismide Semiconductor Lasers", Semicon. Sci. Tech. 27, 094011 (2012).

[8] J. Hwang and J.D. Phillips, "Band Structure of Strain-Balanced GaAsBi/GaAsN Superlattices on GaAs", Phys. Rev. B 83, 195327 (2011).

[9] C.A. Broderick, S. Jin, I.P. Marko, K. Hild, P. Ludewig, Z.L. Bushell, W. Stolz, J.M. Rorison, E.P. O'Reilly, K. Volz, and S.J. Sweeney, "$GaAs_{1-x}Bi_x/GaN_yAs_{1-y}$ Type-II Quantum Wells: Novel Strain-Balanced Heterostructures for GaAs-Based near- and Mid-Infrared Photonics", Sci. Rep. 7, 46371 (2017).

[10] E.S. Zech, A.S. Chang, A.J. Martin, J.C. Canniff, Y.H. Lin, J.M. Millunchick, and R.S. Goldman, "Influence of GaAs Surface Termination on GaSb/GaAs Quantum Dot Structure and Band Offsets", Appl. Phys. Lett. 1-3, 082107 (2013).

[11] C. Greenhill, A.S. Chang, E.S. Zech, S. Clark, G. Balakrishnan, and R.S. Goldman, "Influence of Quantum Dot Morphology on the Optical Properties of GaSb/GaAs Multilayers", Appl. Phys. Lett. 116, 252107 (2020).

[12] L. Wang, L. Zhang, L. Yue, D. Liang, X. Chen, Y. Li, P. Lu, J. Shao, and S. Wang, "Novel Dilute Bismide, Epitaxy, Physical Properties and Device Application", Crystals, 7, 63 (2017).

[13] Z. Batool, K. Hild, T.J. Hosea, X. Lu, T. Tiedje, and S.J. Sweeney, "The Electronic Band Structure of GaBiAs/GaAs layers: Influence of Strain and Band Anti-crossing", J. Appl. Phys. 111, 113108 (2012).

[14] K. Alberi, O.D. Dubon, W. Walukiewicz, K.M. Yu, K. Bertulis, and A. Krotkus, "Valence Band Anticrossing in $GaBi_xAs_{1-x}$", App. Phys. Lett. 91, 051909 (2007).

[15] Z.L. Bushell, C.A. Broderick, L. Nattermann, R. Joseph, J.L. Keddie, J.M. Rorison, K.Volz, and S.J. Sweeney, "Giant Bowing of the Band Gap and Spin-orbit Splitting energy in $GaP_{1-x}Bi_x$ Dilute Bismide Alloys", Scientific Reports, 9, 6835, (2019).

[16] L. Wang, L. Zhang, L. Yue, D. Liang, X. Chen, Y. Li, P. Lu, J. Shao, and S. Wang, "Novel Dilute Bismide, Epitaxy, Physical Properties and Device Application", Crystals, 7, 63 (2017).

[17]C.G. Van De Walle, "Band Lineups and Deformation Potentials in the Model-solid Theory", Phys. Rev. B. 39, 1871 (1989).

[18] M. Hayne, J. Maes, S. Bersier, V. V. Moshchalkov, A. Schliwa, L. Müller-Kirsch, C. Kapteyn, R. Heitz, and D. Bimberg, "Electron Localization by Self-Assembled GaSb/GaAs Quantum Dots", Appl. Phys. Lett. 82, 4355 (2003).

[19] G. Balakrishnan, J. Tatebayashi, A. Khoshakhlagh, S.H. Huang, A. Jallipalli, L.R. Dawson, and D.L. Huffaker, "III/V Ratio Based Selectivity Between Strained Stranki-Krastanov and Strain-free GaSb Quantum Dots on GaAs", Appl. Phys. Lett. 89, 161104 (2006).

[20] M.J. Hÿtch, E. Snoeck, R. Kilaas, "Quantitative Measurement of Displacement and Strain Fields from HREM Micrographs", Ultramicroscopy, 73, 131 (1998).

[21] S. Huang, S.J. Kim, X. Q. Pan, and R.S. Goldman, "Origins of Interlayer Formation and Misfit Dislocation Displacement in the Vicinity of InAs/GaAs Quantum Dot", Appl. Phys. Lett. 105, 032107 (2014).

[22] B.R. Bennet, P.M. Thibado, M.E. Twigg, E.R. Glaser, R. Magno, B.V. Shanabrook, and L.J. Whitman, "Self-assembled InSb and GaSb Quantum Dots on GaAs (001)", J. Vac. Sci. Technol. B, **14,** 3 (1996).

[23] A. Lorke, R.J. Luyken, J.M. Garcia, and P.M. Petroff. "Growth and Electronic Properties of Self-Organized Quantum Rings", Jpn. J. Appl. Phys. **40,** 1857 (2001).

[24] S. Kobayashi, C. Jiang, T. Takuya, and H. Sakai, "Self-assembled Growth of GaSb Type II Quantum Ring Structures", Jpn. J. Appl. Phys. **43,** 662, (2004).

Appendices

Appendix A

Specimen Preparation Techniques

Overview

In this appendix, we describe the preparation steps of our LEAP specimens using a FEI Helios secondary electron microscope (SEM), equipped with a focused-ion-beam (FIB). Specimens were prepared by the author using the FEI Helios SEM at the Michigan Center for Materials Characterization $(MC)^2$.

A.1 LEAP sample preparation

In general, sample wafers were loaded onto the SEM stage such that the growth direction (001) was parallel to the SEM beam. For the Helios system, the FIB ion beam is tilted at an angle of 52º with respect to the sample surface and stage. Before specimen preparation, we calibrated the height of the sample surface at which tilting does not change its distance from the electron beam (i.e., the eucentric height). First, a ~1 μm x 1 μm feature is moved to focus on the center field-of-view. The sample is then tilted by 5º. If the feature moves from the center field-of-view, the stage height is adjusted in +z or -z to bring the feature back to the center field of view. This step is repeated for sample tilts of 15º, 30º, 45º, and 52º until the feature no longer moves from the center field-of-view for all sample tilt angles.

A.1.1 Depositing platinum (Pt) protective layer

To reduce potential damage that could occur when imaging with the FIB, a protective layer of Pt (~12 μm length x 2.8 μm width x 100 nm depth) was deposited by the electron beam at 2 kV and 1.6 nA on a selected area of the sample surface. After Pt deposition with the electron beam, the sample was tilted to 52º and more Pt was deposited with the FIB at 30 kV and 80 pA. Figure A.1(a) shows the area of the sample surface after both SEM and FIB depositions. The purpose of the Pt layer is to protect the underlying sample from Ga^+ ion implantation from the FIB source during milling and tip shaping, as ion implantation can change the atomic structure of the sample.[1]

A.1.2 Ion milling and lift-out

To mill out the edges around the protective layer using the FIB, the sample stage was tilted to 22º. The FIB was used to form a ~30º wedge-shaped sample, partially freeing the prepared material from the wafer, as shown in Figure A.1(b). After three edges of the sample were milled, a sharp tungsten (W) needle mounted on the Omniprobe, was placed in contact with the sample, attached using Pt, as shown in Figure A.1(c), and the final edge was cut with the ion beam. The wedge-shaped portion of the sample was then "lifted-out" and subsequently transferred to the Si posts using Pt, as shown in Figure A.1(d).

After securing the wedge-shaped sample to the Si post using Pt, the sample was detached from the Omniprobe using FIB milling. Finally, the Si post with attached specimen is rotated 180º to deposit Pt on the opposite side of the specimen for properly securing the sample before tip-shaping. An example of the resulting sample piece is shown

in Figure A.2(a). Steps that include mounting the specimen on the Si post were repeated to generate 3-4 samples on Si posts for the production of multiple LEAP specimens.

A.1.3 Tip shaping

Needle-like specimens are prepared using FIB milling using steps listed in Table A.1. The SEM grid containing the Si posts and specimens is tilted 52º such that the ion beam is parallel to the Si posts. A computer-assisted donut-shaped pattern with a 4 μm outer diameter (OD) and a 2 μm inner diameter (ID) was centered over the specimen and FIB milling is performed using 30 kV voltage and a 9.3 nA current. An example SEM image of a GaAsNBi sample is shown in Figure A.2(b), with constrast variations associated with SEM-deposited versus FIB-deposited Pt. Each of the steps listed in Table A.1 were performed. Finally, a low-energy ion beam is used to reduce the thickness of topmost damaged, as studied by Bogdanowicz, et al.[2]

	Voltage (kV)	**Current (nA)**	**OD (μm)**	**ID (μm)**	**z-depth (μm)**	**Est. Time**
Step 1	30	9.3	10	4	2	0:50
Step 2	30	2.5	6	2	3.5	1:56
Step 3	30	0.79	3	1	3.5	1:34
Step 4	30	0.08	2	0.5	0.5	1:07
Final Cleaning Step	5	0.068	3x3 rectangle		2	~0:15

Table A.1 LEAP specimen-shaping procedure using the FEI Helios SEM/FIB at the Michigan Center for Materials Characterization (MC)[2].

A.2 Figures

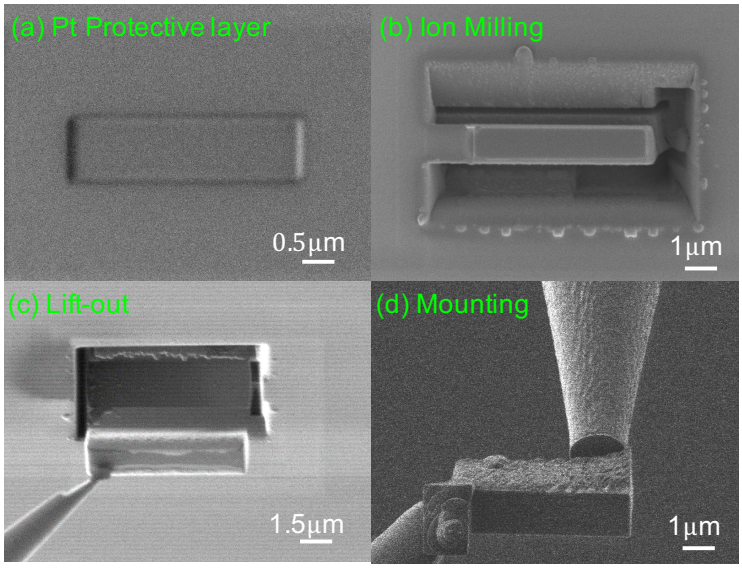

Figure A.1 SEM images of "lift-out" and mounting steps for making LEAP specimens: (a) Platinum layer deposited by SEM/FIB to protect underlying sample from ion beam damage during tip shaping. (b) Milling around the sample area to partially free the sample piece from the wafer. (c) Sample piece is "lifted-out" using a needle-shaped tool, called an Omniprobe. (d) Wedged sample is mounted on a silicon post.

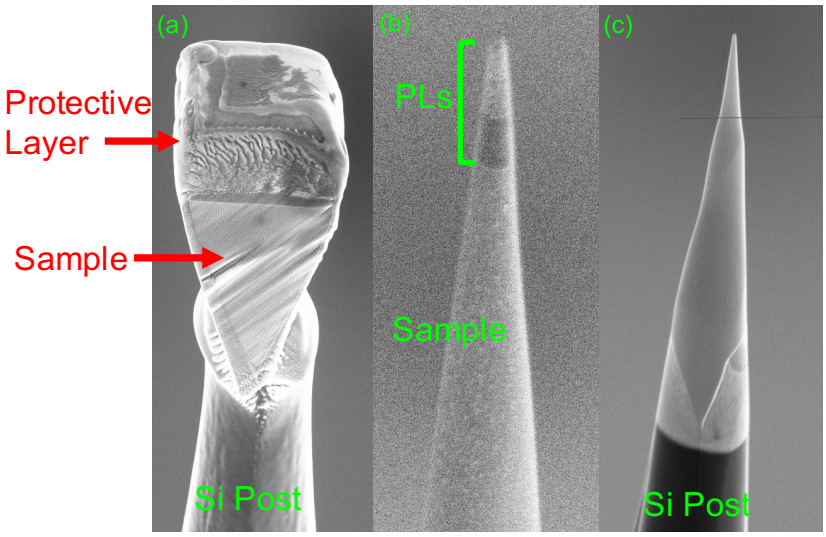

Figure A.2 SEM images of tip shaping process for LEAP specimens: (a) GaAsNBi sample mounted on a silicon post with a thin layer of SEM-deposited Pt and a thick layer of FIB-deposited Pt on top of the sample. (b) Partially-shaped sample which resembles a cone with layer of SEM- and FIB-deposited Pt apparent. (c) LEAP specimen after final tip-shaping step.

Appendix B

IVAS™ Reconstruction Parameters

Overview

In this appendix, we describe the details of performing 3D reconstructions of the LEAP datasets for the specimens described in Chapters 3 and 4, including labeling mass spectra and selecting reconstruction parameters using the Cameca Integrated Visualization and Analysis Software (IVAS™).[24]

B.1 LEAP dataset reconstruction in IVAS™

In this dissertation, IVAS 3.8 was used to reconstruct LEAP datasets presented. In general, reconstruction details involve (1) selection of an ion sequence from experiment, (2) labeling of detected ions in the mass spectra, and (3) setting parameters (i.e., image compression factor, initial tip radius, etc.) for the final shape of the reconstruction. Further instructions for building the reconstructions and performing different analyses are detailed in the IVAS 3.8 manual provided with the software. Additional information on LEAP analyses can be found in Larson, et al.[3]

B.1.1 Selecting appropriate ion sequence

After reviewing details of the experiment at the start of a new project in IVAS™, the first step is to select ion sequence to be used for the reconstruction. Figure B.1 shows the voltage evolution with ion sequence number during LEAP acquisition. For the reconstructions in this work, only single and multiple hit classes were selected, as these classes represent majority (>97%) of the hits. To disable (enable) a hit class, uncheck (check) the appropriate box relating that hit class and click "Apply" to load the changes. The bounding box in the X and Y axes was adjusted to include the most linear region of the acquisition, avoiding the beginning of the acquisition where the stage, laser energies, and applied voltages were being adjusted during the LEAP experiment. It is useful for the user to note the starting ion sequence number during the LEAP experiment to mark the beginning of the bounding box for reconstructing the LEAP dataset later. Sudden jumps in the voltage, likely due to tip microfractures, such as those labeled in Figure B.1, were avoided.

B.1.2 Selecting detector region of interest (ROI)

Figure B.2 shows the distribution of hits across the detector. Low numbers of hits are shaded in purple and blue, while high numbers of hits are shaded in green, yellow, orange, and red. The ions to be included in the reconstruction were isolated to eliminate regions of the histogram with very low counts. This was done by adjusting the black ellipse on the detector event histogram, as shown in Figure B.2.

B.1.3 Time-of-flight (TOF) corrections

As a part of the LEAP reconstruction process, the next step involves corrections to the TOF paths due to variations in the applied voltage and bowl corrections to account for the shape of the detector and geometry of the flight path. Two to three well-separated peaks are identifed. In this work, the H-1, Ga-69, and Bi-209 peaks were selected. Iterative corrections were made until there were negligible improvements in resolution of the half-max (FWHM), tenth-max (FWTM), and hundredth-max (FW01M) of the selected peaks.

B.1.4 Mass spectra calibration and labeling

Using peaks selected in the previous step, the reconstruction wizard then shifts the entire mass spectrum according to a mass linearization algorithm. More details about the algorithm are described in the manual for the IVAS software.[24] After calibration, the remaining peaks in the mass spectrum were assigned by the user. The mass-to-charge ratios (m/z) for the ions studied in this work are presented in Table. B.1.

m/z	ion species	m/z	ion species	m/z	ion species
1	H	75	As^{+} or As_2^{2+}	172 and 173	As_3Sb^{2+}
2	H_2	89	AsN^{+}	187.5	As_5^{2+}
25	As^{3+}	98 and 99	AsSb2+	196 and 198	$AsSb^{+}$
37.5	As^{+} or As^{2+}	104.5	Bi^{2+}	209	Bi+
40.3 and 41	Sb_2^{3+}	112.5	As_3^{2+}	225	As_3^{+}
44.5	AsN^{2+}	121 and 123	Sb^{+}	300	As^{4+}
60.5 and 61.5	Sb^{2+}	125	$AsSb^{3+}$		
69 and 71	Ga^{+}	135 and 136	As_2Sb^{2+}		
69.6	Bi^{3+}	150	As^{2+} or As_4^{2+}		

Table B.1 Ion species and their corresponding mass-to-charge ratios (m/z) used for the work presented in this dissertation.

B.1.5 Final reconstruction parameters

For final reconstruction, SEM images of the sharpened specimens was used to estimate the initial tip radius and shank half angle in IVAS. For our work, the initial tip radii typically ranged from 20-30nm, while the estimated shank half angles ranged from 10° to 20°. This method proved best for the reconstruction of GaAsNBi specimens. To evaluate the quality of the reconstructions, spatial distribution maps (SDMs)[4] were created to validate the periodicity of the reconstruction against known planar spacing within the specimen. An example of a SDM created for a GaAsNBi reconstruction is presented in Figure B.4(b). For creating the SDM, a cylindrical region of interest (ROI) near the center of the reconstruction was constructed, as depicted in Figure B.4(a). To view the nearest neighbor distances between Ga ions, "Ga" was selected as "centers" and "Ga" were selected as "neighbors" within IVAS SDM analysis tab. The lattice spacing in the z-direction (001) is depicted by the most defined peaks to the left and right of the center peak at z = 0.0, as shown by the black, dotted lines in Figure B.4(b). The SDM shows the average distances between Ga ions are 0.34 nm and 0.56 nm. The distance of 0.56 nm is similar to the lattice constant for a GaAs zinc-blende unit cell, while the average distance of 0.34 nm is similar to the distance between the Ga positions at the corners and face centers of the unit cell. The radii, shank half angle, and image compression factor (ICF) were varied until these average nearest neighbor distances were obtained. More information about these parameters can be found in Section 6 of the IVAS manual.[24]

B.2 Figures

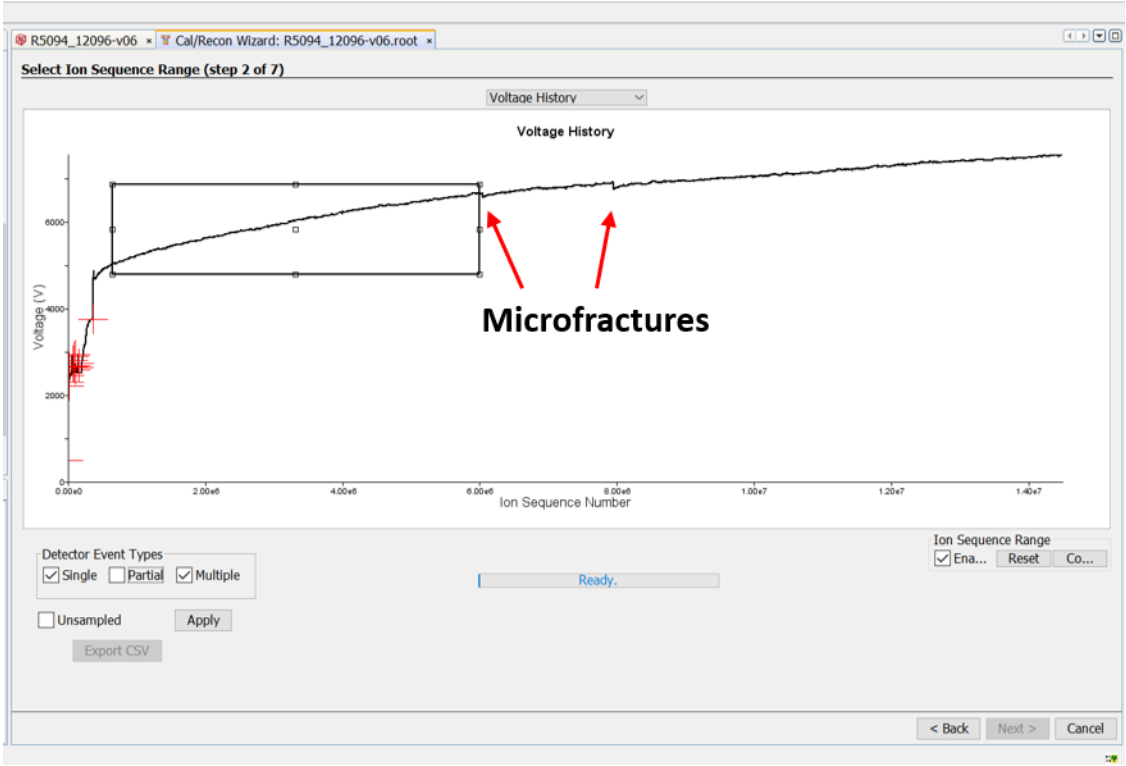

Figure B.1 IVAS Reconstruction Wizard Step 2 of 7: The voltage evolution of the acquisition as a function of ion sequence number. An adjustable box is used to define the portion of the acquisition from which hits will be reconstruction. Select "Commit" after the bounding box has been modified to commit ion range for the reconstruction.

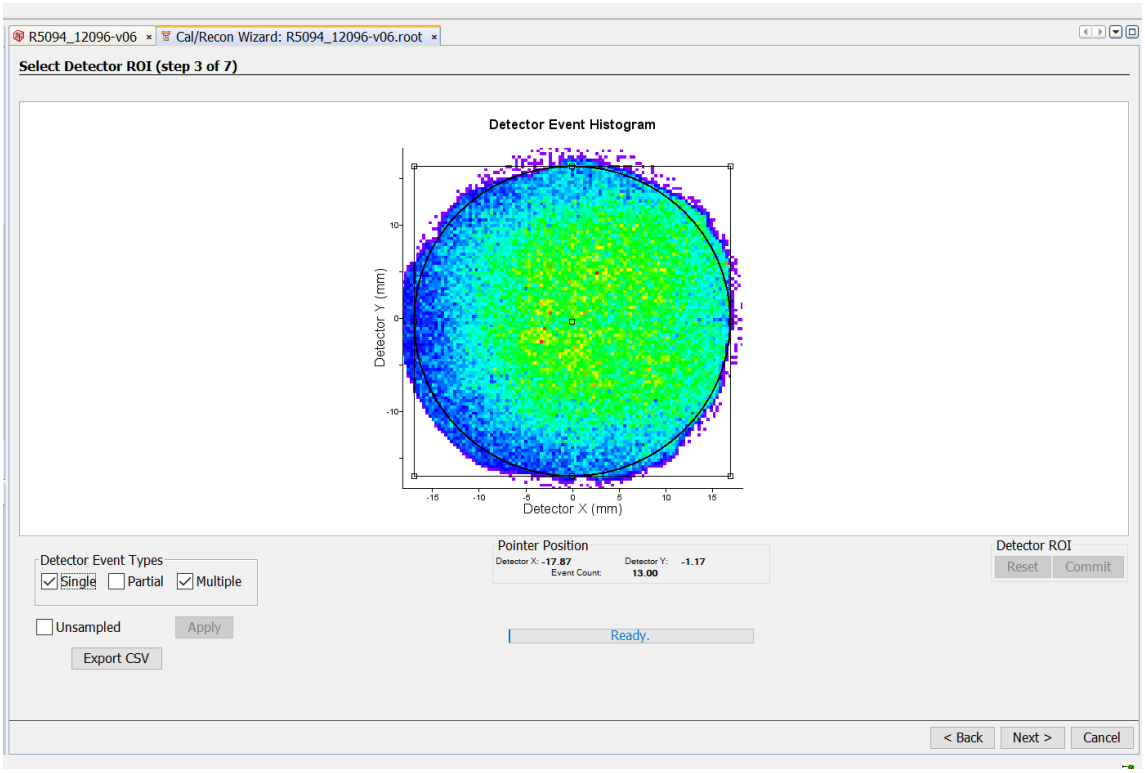

Figure B.2 IVAS Reconstruction Wizard Step 3 of 7: A color map showing the distribution of hits across the detector for ~14.5 million hits. Low numbers of hits are shaded in purple and blue, while high numbers of hits are shaded in green, yellow, orange, and red.

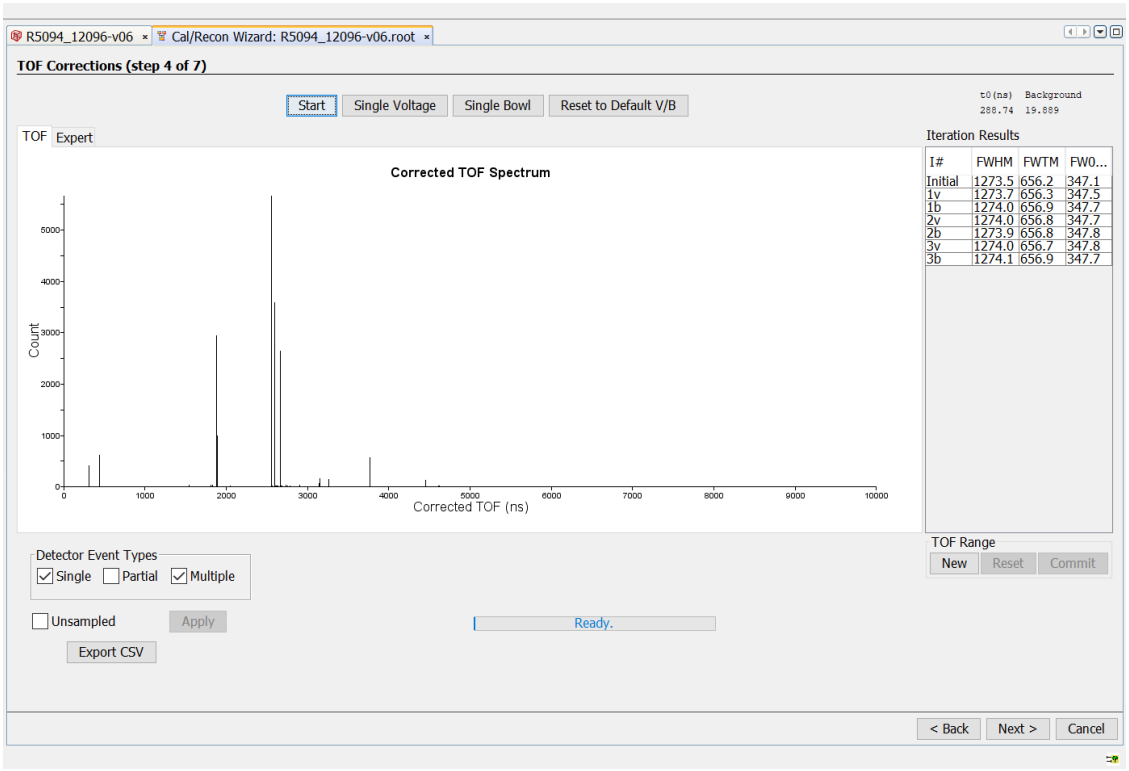

Figure B.3 IVAS Reconstruction Wizard Step 4 of 7: Voltage and bowl corrections are computed for the analysis by clicking "Start". Two to three well-separated peaks are identified. In this work, the H-1, Ga-69, and Bi-209 peaks were selected. Iterative voltage and bowl corrections were made until there were negligible improvements in resolution of the half-max (FWHM), tenth-max (FWTM), and hundredth-max (FW01M) of the selected peaks.

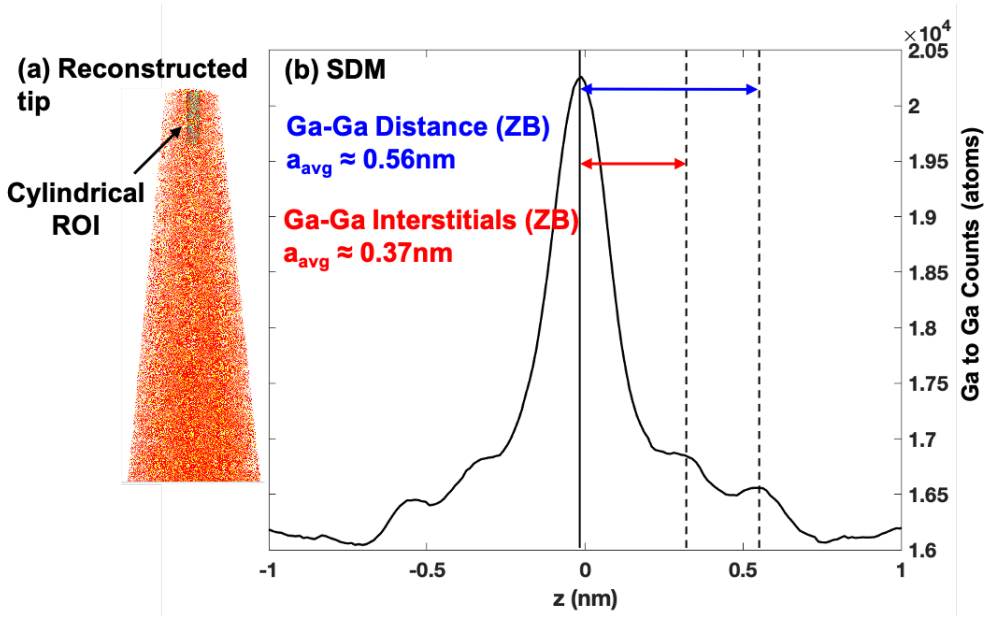

Figure B.4 (a) Reconstructed GaAsNBi tip, with 5 nm (diameter) x 20 nm (length), with cylindrical region of interest (ROI) selected near center of the reconstruction. The Ga counts as a function of distance across the ROI diameter are averaged over the ROI length and plotted in the (b) spatial distribution map (SDM). For generating the SDM, Ga elements are centered around other Ga atoms in 3 dimensions within the ROI (Ga to Ga). The resulting first and second nearest neighbors for Ga are then compared with expected values for GaAs.

Appendix C

Data Analysis

Overview

In this appendix, we describe the methods for data analyses included in this dissertation.

C.1 LEAP Data Analysis

In this section, we describe our method of analyzing Sb compositions and estimating Sb densities within the GaSb/GaAs multilayers described Chapter 4, followed by our method of estimating effective fields described in Chapter 3.

C.1.1 Sb composition profiles

To determine the average Sb composition within the GaSb layers in Section 3.4, 5 cylindrical regions (15 nm diameter x 100-130 nm length) along the [001] growth axis were selected. 1D profiles of the fraction of Sb atoms within the cylindrical volume, x_{Sb}, we measured using a z-step size of 0.30 nm. The Sb fraction was denoted as the number of Sb atoms out of the total number of Group V elements. For 2DLs and 2DLs+3DNSs, the average x_{Sb} values are 0.08 and 0.12 within the 2D layers, with x_{Sb}< ~0.01 within the GaAs spacer regions.

C.1.2 Sb density calculations

To determine the areal Sb densities within the cylinders, we integrated the 1D compositional profile and divided by the circular cross-sectional area. Figure C.1 shows an example of an integrated 1D compositional profile for the 2DLs+3DNSs, showing the total number of Sb atoms measured within each layer. To determine the measured areal Sb density, the total number of Sb atoms was then divided by the cross-sectional area (πr^2) of the cylindrical region used to obtain the 1D profile. The LEAP-determined Sb areal densities were 2.69 and 4.86 Sb atoms/nm^2 for 2DLs and 2DLs+3DNSs, lower than the targeted areal densities of 5.97 and 7.96 atoms/nm^2, respectively. To compute the targeted areal density from growth deposition, a closely-packed zinc-blende GaSb unit cell was assumed, where the unit cell consist of 2 monolayers (MLs). The method for estimating the theoretical number of deposited Sb atoms is shown in Figure C.2.

C.1.3 Effective field estimations

The effective field is described by probability of post-ionization of metallic ions from a specimen, as described by the post-ionization theory introduced by Kingham.[5] Kingham's post-ionization theory involves the initial evaporation of an ion as a singly-charged species that is further ionized into higher charge states by electrons tunneling back to the specimen. Post-ionization takes place at a distance within several angstroms of the specimen and is assumed to be material-independent. Russo, et al.[6] discussed limitations to Kingham's model, including that *initial* ion evaporation is only singly-charged, with higher charge states forming post-evaporation. However, this assumption may be violated

at higher laser energies,[7] where initial ion evaporation of multiply-charged states occurs. Furthermore, more complicated evaporation behavior may occur in semiconductors due to atomic polarizations.[25]

Kingham's effective field estimates are based on the evaporation of monotomic species (i.e. X^+, X^{2+}, X^{3+}, etc). Since we observe no cluster ions for Ga, only monotomic Ga^+ (Ga^{2+}) at 69 and 71 (34.5 and 35.5) Da, we use charge-state metrics of Ga to estimate the effective fields in Section 4. Figure C.3(a) and (b) show the integrated mass spectra for Ga^{2+} and Ga^+ ions, respectively. The charge-state ratio (CSR) was calculated by dividing the total number of Ga^{2+} ions by the total number of Ga^+ ions from the integrated mass spectra. The CSRs were then compared to the probability versus effective field calculations adapted from Kingham, as shown in Figure C.3(c).

C.2 Nextnano Data Analysis

To estimate the electronic band structure of the GaSb/GaAs multilayers presented in Chapter 4, confined hole energies were calculated using an 8 x 8 $\mathbf{k}\cdot\mathbf{p}$ approximation within the nextnano commercial software package.[9] Strain was calculated in the continuum elasticity approach with elastic constants from Vurgaftman et al.[10] Values for band offsets[11] within model-solid theory[12] and deformation potentials[13] were subsequently used to calculate the conduction and valence bands, assuming a 1.43 eV bowing parameter for GaSb-GaAs.[10] Finally, the confined energy levels were determined by solving the Schrödinger and Poisson equations, self-consistently, as described elsewhere.[14,15] Below are the parameters used in this program as well as the input script for nextnano^{++}.

C.2.1 Material Parameters

Materials database	Symbol	GaAs	GaSb
lattice constant (nm)[10]	a	0.56532	0.60959
electron effective mass (kg)[10]	m_e/m_o	$0.067m_o$	$0.039m_o$
hole effective mass[14]	m_h/m_o	0.51	0.34
band offset (eV)[14]	ΔE_v	0.67	
band gap (eV)[10]	E_g	1.519	0.81
spin-orbital coupling (eV)[10]	Δ_{SO}	0.341	0.76
Varshni parameters (Γ)[10]	α (meV/K)	0.5405	--

*$m_o = 9.11 \times 10^{-31}$ kg

Table C.1 The parameters for ternary alloys, such as $GaAs_{1-x}Sb_x$, refer to interpolation between their binary constituents – GaAs and GaSb.

C.2.2 Modified k·p parameters (Luttinger and DKK)

In 8 x 8 **k·p** theory, the lowest conduction band is included in the **k·p** Hamiltonian and not treated as a perturbation, as in 6 x 6 **k·p** theory.[26] Thus, values described by the 8 x 8 matrix must be replaced within nextnano for the **k·p** calculations used in Chapter 4. For the zinc-blende structure, the values that describe the 8 x 8 matrix depend on the band gap at the Γ-point (E_{gap}), $E_p = 2m_o\mathbf{p}^2/\hbar^2$, and the modified Luttinger parameters (γ_i'). The equations used to calculate the modified Luttinger parameters in this work are below.[16]

$$\gamma_1' = \gamma_1 - \frac{1}{3}\frac{E_p}{E_{gap}} \tag{C.1}$$

$$\gamma_2' = \gamma_2 - \frac{1}{6}\frac{E_p}{E_{gap}} \tag{C.2}$$

$$\gamma_3' = \gamma_3 - \frac{1}{6}\frac{E_p}{E_{gap}} \tag{C.3}$$

$$\kappa' = \kappa - \frac{1}{6}\frac{E_p}{E_{gap}} \tag{C.4}$$

where γ_1, γ_2, and γ_3 are Luttinger parameters taken from Vurgaftman, et al.[10] The equations used to calculate the modified temperature-dependent DKK (Dresslhaus-Kip-Kittel) parameters are below.[16]

$$L' = L + \frac{\hbar^2}{2m_o}\frac{E_p}{E_{gap}} = L + \frac{p^2}{E_{gap}} \tag{C.5}$$

$$M' = M \tag{C.6}$$

$$N' = N + \frac{\hbar^2}{2m_o}\frac{E_p}{E_{gap}} = N + \frac{p^2}{E_{gap}} \tag{C.7}$$

where L, M, and N are the DKK parameters for the 6 x 6 matrix, which are already within the nextnano's materials database.

C.2.3 Nextnano^{++} Code

```
#GaAsSb QD model with Sb gradient, GaAs substrate and matrix. Written by
Christian Greenhill, March 2020

#Begin NextnanoWizard parameter section
$WIDTH = 15                 #width of QD (nm)
$HEIGHT = 6                 #height of QD (nm)
$WETTING = 1.0              #wetting layer thickness (nm)
$ALLOYWETTING = 0.12        #Sb concentration of wetting layer
$ALLOWREGIONI = 0.15        #Sb concentration of QD (gradient)
$ALLOWREGIONII = 0.20       #Sb concentration of QD (gradient)
$ALLOWREGIONIII = 0.25      #Sb concentration of QD (gradient)
$ALLOWREGIONIV = 0.30       #Sb concentration of QD (gradient)
$ALLOWREGIONV = 0.35        #Sb concentration of QD (gradient)
$ALLOWREGIONVI = 0.50       #Sb concentration of QD (gradient)
$ALLOWREGIONVII = 0.60      #Sb concentration of QD (gradient)
$ALLOWREGIONVIII = 0.70 #Sb concentration of QD (gradient)
$SPACING = 0.75             #grid spacing
$NUME = 8                   #number of electron states to be calculated
$NUMH = 6                   #number of hole states to be calculated
#End NextnanoWizard parameter section

# fixed parameters
$DIST = 20                  # thickness of surrounding GaAs region (nm)
$BARRIER = 3                # expansion of quantum region into barriers (nm)


#Simulation setup
global{
   simulate2D{}
   temperature  = 25
   substrate{ name = "GaAs" }
   crystal_zb{ x_hkl = [1, 0, 0] y_hkl = [0, 1, 0] } # defines orientation of
simulation domain (growth direction: z = [001])
   periodic{
```

```
      x = yes
      y = yes
   }
}

#Grid setup
grid{
   xgrid{
      line{ pos = -$DIST/2              spacing = $SPACING}
      line{ pos = -$WIDTH/2 - 1       spacing = $SPACING/2}
      line{ pos = $WIDTH/2 + 1         spacing = $SPACING}
      line{ pos = $DIST/2               spacing = $SPACING}
   }

   ygrid{
      line{ pos = -$DIST/2              spacing = $SPACING}
      line{ pos = -$WIDTH/2           spacing = $SPACING/2}
      line{ pos = -$WIDTH/2 + 1       spacing = $SPACING}
      line{ pos = $DIST/2               spacing = $SPACING}
   }
}


#Structure setup
structure{
   output_material_index{}
   output_alloy_composition{}

   # GaAs substrate
   region{
      everywhere{}
      binary{ name = "GaAs"}
      contact{ name = "dummy" }
   }

   # GaAsSb QW
   region{
      ternary_constant{
         name = "GaAs(1-x)Sb(x)"
         alloy_x = $ALLOYWETTING
      }
      rectangle{
         x = [0, $WETTING]
         y = [-$DIST, $DIST]
      }
   }


#QD Region I
 # GaAsSb semiellipsoid quantum dot - top half
   region{
      ternary_constant{ name = "GaAs(1-x)Sb(x)"
         alloy_x = $ALLOWREGIONI
         }

      semiellipse{    # 2D object, e.g. a simple semiellipse along the x axis
         base_x     = [0, 0]       #extension of base plane in x direction
         base_y     = [ -$WIDTH/2,  $WIDTH/2]       # base line at y = 5 nm
         top        = [3*$HEIGHT/4,0]       # top coordinate of the semiellipse
(x,y) [nm]
      }
   }
```

```
 # GaAsSb semiellipsoid quantum dot - bottom half
   region{
      ternary_constant{ name = "GaAs(1-x)Sb(x)"
         alloy_x = $ALLOWREGIONI
      }

      semiellipse{
         base_x     = [0,0
         base_y     = [ -$WIDTH/2,  $WIDTH/2]
         top        = [-$HEIGHT/4,0]             }
   }


#QD Region II
 #GaAsSb semiellipsoid quantum dot - top half
   region{
      ternary_constant{ name = "GaAs(1-x)Sb(x)"
         alloy_x = $ALLOWREGIONII
         }

      semiellipse{
         base_x     = [0, 0]
         base_y     = [ -7*$WIDTH/16,  7*$WIDTH/16]
         top        = [21*$HEIGHT/32,0]
      }
   }

 #GaAsSb semiellipsoid quantum dot - bottom half
   region{
      ternary_constant{ name = "GaAs(1-x)Sb(x)"
         alloy_x = $ALLOWREGIONII
      }

      semiellipse{
         base_x     = [0,0]
         base_y     = [ -7*$WIDTH/16,  7*$WIDTH/16]
         top        = [-7*$HEIGHT/32,0
      }
   }

#QD Region III
 # GaAsSb semiellipsoid quantum dot - top half
   region{
      ternary_constant{ name = "GaAs(1-x)Sb(x)"
         alloy_x = $ALLOWREGIONIII
         }

      semiellipse{
         base_x     = [0, 0]
         base_y     = [ -3*$WIDTH/8,  3*$WIDTH/8]
         top        = [9*$HEIGHT/16,0]
      }
   }

 # GaAsSb semiellipsoid quantum dot - bottom half
   region{
      ternary_constant{ name = "GaAs(1-x)Sb(x)"
         alloy_x = $ALLOWREGIONIII
      }

      semiellipse{
         base_x     = [0,0]
         base_y     = [ -3*$WIDTH/8,  3*$WIDTH/8]
```

```
         top         = [-3*$HEIGHT/16,0]
      }
   }


#Region IV
 # GaAsSb semiellipsoid quantum dot - top half
   region{
      ternary_constant{ name = "GaAs(1-x)Sb(x)"
         alloy_x = $ALLOWREGIONIV
         }

      semiellipse{
         base_x      = [0, 0]
         base_y      = [ -5*$WIDTH/16,  5*$WIDTH/16]
         top         = [15*$HEIGHT/32,0]
      }
   }

 #GaAsSb semiellipsoid quantum dot - bottom half
   region{
      ternary_constant{ name = "GaAs(1-x)Sb(x)"
         alloy_x = $ALLOWREGIONIV
      }

      semiellipse{
         base_x      = [0,0]
         base_y      = [ -5*$WIDTH/16,  5*$WIDTH/16]
         top         = [-5*$HEIGHT/32,0]
      }
   }



#QD Region V
 # GaAsSb semiellipsoid quantum dot - top half
   region{
      ternary_constant{ name = "GaAs(1-x)Sb(x)"
         alloy_x = $ALLOWREGIONV
         }

      semiellipse{
         base_x      = [0, 0]
         base_y      = [ -$WIDTH/4,  $WIDTH/4]
         top         = [3*$HEIGHT/8,0]
      }
   }

   #GaAsSb semiellipsoid quantum dot - bottom half
   region{
      ternary_constant{ name = "GaAs(1-x)Sb(x)"
         alloy_x = $ALLOWREGIONV
      }

      semiellipse{
         base_x      = [0,0]
         base_y      = [ -$WIDTH/4,  $WIDTH/4]
         top         = [-$HEIGHT/8,0]
      }
   }


#Region VI
```

```
 #GaAsSb semiellipsoid quantum dot - top half
   region{
      ternary_constant{ name = "GaAs(1-x)Sb(x)"
         alloy_x = $ALLOWREGIONVI
         }

      semiellipse{
         base_x     = [0, 0]
         base_y     = [ -3*$WIDTH/16,  3*$WIDTH/16]
         top        = [9*$HEIGHT/32,0]
      }
   }

   #GaAsSb semiellipsoid quantum dot - bottom half
   region{
      ternary_constant{ name = "GaAs(1-x)Sb(x)"
         alloy_x = $ALLOWREGIONVI
      }

      semiellipse{
         base_x     = [0,0]
         base_y     = [ -3*$WIDTH/16,  3*$WIDTH/16]
         top        = [-3*$HEIGHT/32,0]
      }
   }


#Region VII
 # GaAsSb semiellipsoid quantum dot - top half
   region{
      ternary_constant{ name = "GaAs(1-x)Sb(x)"
         alloy_x = $ALLOWREGIONVII
         }

      semiellipse{
         base_x     = [0, 0]
         base_y     = [ -$WIDTH/8,  $WIDTH/8]
         top        = [3*$HEIGHT/16,0]
      }
   }

 #GaAsSb semiellipsoid quantum dot - bottom half
   region{
      ternary_constant{ name = "GaAs(1-x)Sb(x)"
         alloy_x = $ALLOWREGIONVII
      }

      semiellipse{
         base_x     = [0,0]
         base_y     = [ -$WIDTH/8,  $WIDTH/8]
         top        = [-$HEIGHT/16,0]
      }
   }


#Region VIII
 # GaAsSb semiellipsoid quantum dot - top half
   region{
      ternary_constant{ name = "GaAs(1-x)Sb(x)"
         alloy_x = $ALLOWREGIONVIII
      }

      semiellipse{
```

```
         base_x     = [0, 0]
         base_y     = [ -$WIDTH/16,  $WIDTH/16]
         top        = [3*$HEIGHT/32,0]
      }
   }

 #GaAsSb semiellipsoid quantum dot - bottom half
   region{
      ternary_constant{ name = "GaAs(1-x)Sb(x)"
         alloy_x = $ALLOWREGIONVIII
      }

      semiellipse{
         base_x     = [0,0]
         base_y     = [ -$WIDTH/16,  $WIDTH/16]
         top        = [-$HEIGHT/32,0]
      }
   }
}


#New material parameters. Overwrites parameters in materials database
database{
   #binary_zb{
      #name = GaAs
      #kp_8_bands{
         #E_P = 28.8
         #B = 7.979
         #L = 4.02630
         #S = -4.01594
         #M = -3.860
         #N = 2.66630          #Calculated for T=300K
         #B = 0
         #L = 2.75827
         #M = -3.86            #L',M',N' for 8kp, calculated for T=25K,
Birner's thesis (not necessarily needed here)
         #N = 1.39827          #L',M',N' calculated using gamma1, gamma2, and
gamma3 from Vurgaftman
      #}
   #}

   ternary_zb{
      name = "GaAs(1-x)Sb(x)"
      valence = III_V
      binary_x = GaSb
      binary_1_x = GaAs

      valence_bands{
         bandoffset = -1.06      #Vurgaftman
         delta_SO = 0.6          #Vugaftman
      }
   }
}

#Calculates bandedges
classical{
   Gamma{}
   LH{}
   HH{}
   SO{}

   output_bandedges{}
   output_carrier_densities{}
```

```
   output_ionized_dopant_densities{}
   output_intrinsic_density{}
}


#Setup for Quantum calculations (i.e. hole confiment energies)
quantum{
   region{
      name = "dot"
      x = [-$DIST/2, $DIST/2]
      y = [-$DIST/2, $DIST/2]
      boundary{ x = dirichlet y = dirichlet}


kp_8band{                          # solves 8x8 k.p Schrodinger equation for the
Gamma conduction band and the heavy, light and split-off hole valence bands
         num_electrons     = $NUME      # number of electron eigenvalues
         num_holes         = $NUMH      # number of hole eigenvalues
         kp_parameters{
            use_Luttinger_parameters = yes
            from_6band_parameters = yes
            evaluate_S = yes
            approximate_kappa = yes
            rescale_S_to = 1.0 }
         #accuracy          = 5e-4       # accuracy of eigenvalue (default is:
1e-7)
         k_integration{                 # Integration over k|| space for
density calculations (for 1D and 2D only).
            relative_size = 0.1          # range of k|| integration relative to
size of Brillouin zone (default is: 1.0, often 0.1-0.2 is sufficient)
            num_points    = 10           # number of k|| points, where
Schrï¿½dinger equation has to be solved (in one direction) (default is: 10)
                                    # In 1D, the number of Schrï¿½dinger
equations that have to be solved depends quadratically on num_points.
                                    # In 2D, the number of Schrï¿½dinger
equations that have to be solved depends linearly         on num_points.
            #num_subpoints = 2           # number of points between two k||
points, where wave functions and eigenvalues will be interpolated (default is:
5)
            #max_symmetry  = no          # do not use symmetry of Brillouin
zone to reduce number of k|| points
            #          = C2          # use up to C2 symmetry of Brillouin zone
to reduce number of k|| points
            #          = full        # use full symmetry of Brillouin zone to
reduce number of k|| points (default)
         }
         #lapack {}
         #iterations        = 2000        # number of iterations for eigenvalue
solver (default is: 500)
         # shift_min_CB      = 0.0       # (optional) [eV] (default is: 0.0 eV,
must be >= 0)
         # shift_max_VB      = 0.0       # (optional) [eV] (default is: 0.0 eV,
must be <= 0)
      } #kp

      output_wavefunctions{  amplitudes = no  probabilities = yes  max_num =
$NUME+$NUMH }
   }
}


poisson{
   output_potential{}
```

```
}


contacts{
   fermi{ name = "dummy" bias = 0.0 } # only needed to define reference energy
}

output{
   section1D{     # ouput a 1D section of the simulation area (1D slice)
       name = "vertical_slice_middle_along_x"
       y =  0.0   # 1D slice at y = 0 nm (through center)
    }
}<>


strain{
   debuglevel = 3
   #minimized_strain{}
   pseudomorphic_strain{}
   #growth_direction = [0,0,1]

   output_strain_tensor{}
   output_polarization_charges{}
}


run{
   solve_strain{}
   solve_poisson{}
   solve_quantum{}
   outer_iteration{                      # solves the Schrodinger,  Poisson
(and current) equations self-consistently
      #iterations      = 20               # number of iterations, i.e. self-
consistency cycles (default is: 30)
      #residual        = 1e5              # residual occupation changes
(default is: 1e5/cm2 (1D), 1e3/cm (2D), 1e-3 (3D))
                                          # (applies to exact Schrï¿½dinger
equation, not to subspace Schrï¿½dinger equation)
      #subspace        = yes/no           # solve Schrï¿½dinger equation within
subspace of eigenvectors of previous iteration
                                          # as long as achieved residual is
larger than desired residual * residual_factor
                                          # and at least in every second
iteration (default is: yes)
      #residual_factor = 1e6              # controls number of subspace
iterations (default is: 1e6)
      #alpha           = 0.1              # underrelaxation parameter for Fermi
level (default is: 1.0, possible range: 0.001 <= alpha <= 1)
      output_log      = yes              # write outer_iteration residuals into
separate logfile (default is: no)
   }}
```

C.3 STS Data Analysis

In this section, the analysis procedures for determining the band edges and effective band gap energies from the STS spectra presented in Chapter 5 are described. The band energies are determined using extrapolation of the linear onsets of the band edges, based

on the work by R. Timm et al.[17] The general steps of the procedure are outlined below, followed by the MATLAB code and graphical user interface, written by A.S. Chang[18] and edited by the author.

C.3.1 Band gap analysis procedure

For analyzing the STS spectra, the first few and last few data points are first removed to avoid troubled areas. The data is then smoothed using MATLAB's "smooth" algorithm, which employs adjacent-averaging.[19] A smoothing constant is chosen such that the conductance values are averaged over an energy less than ~ k_BT. The data are then normalized from 0 to 1 and plotted in a graphical user interface (GUI). The user sets a boundary at dI/dV = 0 and then defines a range for the valence and conduction bands for which linear least-squares fits are performed using MATLAB's "polyfit" algorithm.[20] The valence band and conduction band edges are defined at the intercept of these linear fits and dI/dV = 0. The effective band gap is defined to be the energy difference between the conduction and valence band edges. An example of the GUI applied to an STS spectra is shown in Fig. C.1.

The energy resolution of the STS measurement is determined using an approximation of the full width of half maximum δE,

$$\gamma_1' = \sqrt{(3.3\ x\ k_B T)^2 + (1.8\ x\ eV_{mod})^2} \qquad \text{(E.1)}$$

where T is temperature, k_B is Boltzmann's constant, e is the elementary charge, and V_{mod} is the modulation voltage applied to the bias during the STS measurement.[21] For a modulation voltage of 30 mV at room temperature, δE ≈ 0.1 eV.

C.3.2 STS Band gap analysis MATLAB script

```
function [] = normalization_code_2_subtraction_narrow_bandgap_h()

%-------------------------------------------------------------------------
%This code is based off 9/9/15 version c. For this script to run properly,
%data must contain either forward or backwards STS, but not both. Previous
%versions written by JCW and ASJ only allowed voltage range to vary from
%negative to positive. This problem was fixed in this version by CMG,
%allowing for voltage to vary in either direction for analysis. GDC: This code
%first displays plots of smoothed data with varying smoothing constants for
%determining an appropriate smoothing level. After inspecting each graph,
%the user can decide which smoothed data is preferred for using the GUI.
%-------------------------------------------------------------------------

%Pay careful attention to the way the offset from zero is calculated. A good
%calculation for the offset depends on the specific data set. A better/consistent
%way to calculate the offset is currently being worked on. Also pay close
%attention to smoothing, as this drastically affects the shape of the curve
%for accurately calculating the band edges.

clear variables
clc
close all

%*****************************Nota Bene***********************************%
%Changes made in this section need to be repeated in the section that
%updates the plot

list = dir('*.txt');
n = length(list);
input_text = [ 'Please input the value for i (from 1 to ',num2str(n),') = '];
global i;
i = input(input_text);

%import the voltage values and the I(V) and dI/dV readings
aux = importdata(list(i).name);
disp(list(i).name);

%Save the variables in vectors
v = aux(:,1);
didv = (aux(:,2));

%If bias sweep begins with positive bias voltage
if v(1)>0
     v=-aux(:,1);
     didv = flip (didv);
     display('Warning: Raw data begins with positive voltage. ')
     display('Note: Bias voltage has been inverted.')
     display ('Note: Also, conductance data has been flipped accordingly.')
     dummy=1;
end
```

```
%delete first few points and last few points to avoid trouble areas
pts = 20;
for j=1:pts
    didv(1)=[];
    v(1)=[];
end
for j=length(didv)-pts:length(didv)
    didv(length(didv))=[];
    v(length(v))=[];
end

%If data is turned upside down (LIA phase = 180 degrees)
%mdpt = round( length(didv)/2 );
%if didv (mdpt) < 1
%    didv = -didv;
%    display ('Data has been flipped 180 degrees due to phase parameter.')
%end

%************************End Nota Bene**********************************%


%********************Smoothing Determination*****************************%
%Obtain the number of smoothing processes from the user (typically 50-100)
%Takes all smoothing constants from 5-30 in intervals of 1, and applies each
%constant to the didv data for user analysis before GUI is run.
smooth_constants = 5:1:30;

didv_smoothed = zeros(length(didv),length(smooth_constants));
for j = 1:length(smooth_constants)
    didv_smoothed(:,j) = smooth(didv,smooth_constants(j));
end

%Calculate the offset for each dI/dV curve from zero.
for j = 1:length(smooth_constants)
    offset_temp(j) = min(didv_smoothed(:,j));
    didv_smoothed(:,j) = didv_smoothed(:,j) - offset_temp(j);
    didv_smoothed(:,j) = didv_smoothed(:,j) / max(didv_smoothed(:,j));
end

%Create figures with various smoothing constants for user to decide is best
%for ensuing analysis. Value j = 1 corresponds to smoothing constant 5, j =
%2 to smoothing constant 6, etc.
for j=1:length(smooth_constants)
    figure(j)
    plot(v,didv_smoothed(:,j), 'Linewidth', 1.5);
    grid on;
    %title(['Smoothing Constant ',num2str(smooth_constants(j))]);
    title(['Smoothing Constant Element ',num2str(j)]);
    xlabel('Applied bias (V)');
    ylabel('dI/dV (arb. unit)');
    hold on;
end
```

```
input_text = [ 'Please choose the value for k (from 1 to
',num2str(length(smooth_constants)),') ' ...
    'to determine smoothing constant = '];
global k;
k = input(input_text);

final_smooth_constant = smooth_constants (k);
didv = smooth (didv, final_smooth_constant);


X = ['Remember to first set the smoothing constant value to ',...
    num2str(final_smooth_constant),' later in code. Then rerun',...
    ' script again before analysis.'];

display(X)
close all;

%***************End of Smoothing Determination Section*******************%



%**************************** GUI Part *********************************%
% Creates the figure
S.fh = figure('units','pixels',...
              'position',[10 10 900 600],...
              'menubar','none',...
              'name','STS band edge calc',...
              'numbertitle','off',...
              'resize','off');

%   Creates borders around slider sets
%   Must be done before other code in order to keep these in background
S.b1 = uicontrol('style','edit',...
                 'unit', 'pix',...
                 'enable', 'inactive',...
                 'position', [10 120 440 110],...
                 'backgroundc', get(S.fh,'color'));
S.b2 = uicontrol('style','edit',...
                 'unit', 'pix',...
                 'enable', 'inactive',...
                 'position', [10 240 440 110],...
                 'backgroundc', get(S.fh,'color'));
S.b3 = uicontrol('style','edit',...
                 'unit', 'pix',...
                 'enable', 'inactive',...
                 'position', [10 360 440 110],...
                 'backgroundc', get(S.fh,'color'));

S.b4 = uicontrol('style','edit',...
                 'unit', 'pix',...
                 'enable', 'inactive',...
                 'position', [10 480 440 110],...
                 'backgroundc', get(S.fh,'color'));
```

```
          %   Sets axes object
S.ax = axes('units','pixels',...
            'position',[510 120 350 350]);

%   Sets text boxes for properties
S.Zoom = uicontrol('style','text',...
                   'unit','pix',...
                   'position',[10 570 200 20],...
                   'fontsize',12,...
                   'fontweight','bold',...
                   'BackgroundColor',[.74 0.69 0.03],...
                   'string','Zoom in / out of graph');
S.Flat = uicontrol('style','text',...
                   'unit','pix',...
                   'position',[10 450 200 20],...
                   'fontsize',12,...
                   'fontweight','bold',...
                   'BackgroundColor',[.74 0.69 0.03],...
                   'string','Flat region of the graph');
S.Valence = uicontrol('style','text',...
                   'unit','pix',...
                   'position',[10 330 200 20],...
                   'fontsize',12,...
                   'fontweight','bold',...
                   'BackgroundColor',[.74 0.69 0.03],...
                   'string','Valence band edge');
 S.Conductance = uicontrol('style','text',...
                   'unit','pix',...
                   'position',[10 210 200 20],...
                   'fontsize',12,...
                   'fontweight','bold',...
                   'BackgroundColor',[.74 0.69 0.03],...
                   'string','Conduction band edge');

%Code to save picture of the plot
S.FMT = {[],'jpg','png','bmp'};  % List of file formats.

% Now we create a menu for the figure itself.
S.fm = uimenu(S.fh,'label','Save Plot As');
S.fm(2) = uimenu(S.fm(1),'label','jpg');
S.fm(3) = uimenu(S.fm(1),'label','png');
S.fm(4) = uimenu(S.fm(1),'label','bmp');
set(S.fm(2:4),'callback',{@fm_call})  % To save the drawing.

%Slider titles
%Minimum value of the graph
S.sl5 = uicontrol('style','slide',...
                  'unit','pix',...
                  'position',[60 490 100 20],...
                  'min',-2,'max',2,'val',-2);
S.ed5(1) = uicontrol('style','edit',...
                     'unit','pix',...
                     'position',[20 490 40 20],...
                     'fontsize',10,...
```

```
                    'string','-2');   % Displays the min.
S.ed5(2) = uicontrol('style','edit',...
                    'unit','pix',...
                    'position',[60 515 100 20],...
                    'fontsize',10,...
                    'string','-2');  % Displays the value.
S.ed5(3) = uicontrol('style','edit',...
                    'unit','pix',...
                    'position',[160 490 40 20],...
                    'fontsize',10,...
                    'string','2');    % Displays the max.
S.tex5 = uicontrol('style','text',...
                  'unit','pix',...
                  'position',[20 535 185 20],...
                  'fontsize',10,...
                  'BackgroundColor',[.8 .8 .8],...
                  'string','Minimum value of graph');

%   Maximum value of the graph
S.sl6 = uicontrol('style','slide',...
                 'unit','pix',...
                 'position',[290 490 100 20],...
                 'min',-2,'max',2,'val',2);
S.ed6(1) = uicontrol('style','edit',...
                    'unit','pix',...
                    'position',[250 490 40 20],...
                    'fontsize',10,...
                    'string','-2');   % Displays the min.
S.ed6(2) = uicontrol('style','edit',...
                    'unit','pix',...
                    'position',[290 515 100 20],...
                    'fontsize',10,...
                    'string','2');  % Displays the value.
S.ed6(3) = uicontrol('style','edit',...
                    'unit','pix',...
                    'position',[390 490 40 20],...
                    'fontsize',10,...
                    'string','2');    % Displays the max.
S.tex6 = uicontrol('style','text',...
                  'unit','pix',...
                  'position',[250 535 185 20],...
                  'fontsize',10,...
                  'BackgroundColor',[.8 .8 .8],...
                  'string','Maximum value of graph');


%Minimum value of the flat region
S.sl7 = uicontrol('style','slide',...
                 'unit','pix',...
                 'position',[60 370 100 20],...
                 'min',-2,'max',2,'val',-1);
S.ed7(1) = uicontrol('style','edit',...
                    'unit','pix',...
                    'position',[20 370 40 20],...
```

```
                    'fontsize',10,...
                    'string','-2');   % Displays the min.
S.ed7(2) = uicontrol('style','edit',...
                    'unit','pix',...
                    'position',[60 395 100 20],...
                    'fontsize',10,...
                    'string','-1');  % Displays the value.
S.ed7(3) = uicontrol('style','edit',...
                    'unit','pix',...
                    'position',[160 370 40 20],...
                    'fontsize',10,...
                    'string','2');    % Displays the max.
S.tex7 = uicontrol('style','text',...
                  'unit','pix',...
                  'position',[20 415 185 20],...
                  'fontsize',10,...
                  'BackgroundColor',[.8 .8 .8],...
                  'string','Minimum value');


%   Maximum value of the flat region
S.sl8 = uicontrol('style','slide',...
                 'unit','pix',...
                 'position',[290 370 100 20],...
                 'min',-2,'max',2,'val',1);
S.ed8(1) = uicontrol('style','edit',...
                    'unit','pix',...
                    'position',[250 370 40 20],...
                    'fontsize',10,...
                    'string','-2');   % Displays the min.
S.ed8(2) = uicontrol('style','edit',...
                    'unit','pix',...
                    'position',[290 395 100 20],...
                    'fontsize',10,...
                    'string','1');  % Displays the value.
S.ed8(3) = uicontrol('style','edit',...
                    'unit','pix',...
                    'position',[390 370 40 20],...
                    'fontsize',10,...
                    'string','2');    % Displays the max.
S.tex8 = uicontrol('style','text',...
                  'unit','pix',...
                  'position',[250 415 185 20],...
                  'fontsize',10,...
                  'BackgroundColor',[.8 .8 .8],...
                  'string','Maximum value');

%   Left edge of Valence band
S.sl3 = uicontrol('style','slide',...
                 'unit','pix',...
                 'position',[60 250 100 20],...
                 'min',-2,'max',2,'val',-2);
S.ed3(1) = uicontrol('style','edit',...
                    'unit','pix',...
```

```
                    'position',[20 250 40 20],...
                    'fontsize',10,...
                    'string','-2');   % Displays the min.
S.ed3(2) = uicontrol('style','edit',...
                    'unit','pix',...
                    'position',[60 275 100 20],...
                    'fontsize',10,...
                    'string','-2');  % Displays the value.
S.ed3(3) = uicontrol('style','edit',...
                    'unit','pix',...
                    'position',[160 250 40 20],...
                    'fontsize',10,...
                    'string','2');    % Displays the max.
S.tex3 = uicontrol('style','text',...
                  'unit','pix',...
                  'position',[20 295 185 20],...
                  'fontsize',10,...
                  'BackgroundColor',[.8 .8 .8],...
                  'string','Minimum value of valence band');



%   Right edge of valence band
S.sl4 = uicontrol('style','slide',...
                 'unit','pix',...
                 'position',[290 250 100 20],...
                 'min',-2,'max',2,'val',2);
S.ed4(1) = uicontrol('style','edit',...
                    'unit','pix',...
                    'position',[250 250 40 20],...
                    'fontsize',10,...
                    'string','-2');   % Displays the min.
S.ed4(2) = uicontrol('style','edit',...
                    'unit','pix',...
                    'position',[290 275 100 20],...
                    'fontsize',10,...
                    'string','2');  % Displays the value.
S.ed4(3) = uicontrol('style','edit',...
                    'unit','pix',...
                    'position',[390 250 40 20],...
                    'fontsize',10,...
                    'string','2');    % Displays the max.
S.tex4 = uicontrol('style','text',...
                  'unit','pix',...
                  'position',[250 295 185 20],...
                  'fontsize',10,...
                  'BackgroundColor',[.8 .8 .8],...
                  'string','Maximum value of valence band');


%   Left edge of conduction band
S.sl = uicontrol('style','slide',...
                 'unit','pix',...
                 'position',[60 130 100 20],... %slider
```

```
                  'min',-2,'max',2,'val',-2);
S.ed(1) = uicontrol('style','edit',...
                    'unit','pix',...
                    'position',[20 130 40 20],...
                    'fontsize',10,...
                    'string','-2');   % Displays the min.
S.ed(2) = uicontrol('style','edit',...
                    'unit','pix',...
                    'position',[60 155 100 20],...
                    'fontsize',10,...
                    'string','-2');  % Displays the value.
S.ed(3) = uicontrol('style','edit',...
                    'unit','pix',...
                    'position',[160 130 40 20],...
                    'fontsize',10,...
                    'string','2');    % Displays the max.
S.tex = uicontrol('style','text',...
                  'unit','pix',...
                  'position',[20 175 185 20],...
                  'fontsize',10,...
                  'BackgroundColor',[.8 .8 .8],...
                  'string','Minimum value of conduction band');

%   Right edge of conduction band
S.sl2 = uicontrol('style','slide',...
                  'unit','pix',...
                  'position',[290 130 100 20],...
                  'min',-2,'max',2,'val',2);
S.ed2(1) = uicontrol('style','edit',...
                    'unit','pix',...
                    'position',[250 130 40 20],...
                    'fontsize',10,...
                    'string','-2');   % Displays the min.
S.ed2(2) = uicontrol('style','edit',...
                    'unit','pix',...
                    'position',[290 155 100 20],...
                    'fontsize',10,...
                    'string','2');  % Displays the value.
S.ed2(3) = uicontrol('style','edit',...
                    'unit','pix',...
                    'position',[390 130 40 20],...
                    'fontsize',10,...
                    'string','2');    % Displays the max.
S.tex2 = uicontrol('style','text',...
                  'unit','pix',...
                  'position',[250 175 185 20],...
                  'fontsize',10,...
                  'BackgroundColor',[.8 .8 .8],...
                  'string','Maximum value of conduction band');

% Display the file name
S.text10 = uicontrol('style','text',...
                  'unit','pix',...
                  'position',[495 570 375 30],...
```

```
                    'fontsize',10,...
                    'BackgroundColor',[.8 .8 .8],...
                    'string',list(i).name);

%   Display the calculated valence edge
S.ed11 = uicontrol('style','edit',...
                     'unit','pix',...
                     'position',[545 545 70 20],...
                     'fontsize',10,...
                     'string','N/A');  % Displays the value.
S.tex11 = uicontrol('style','text',...
                    'unit','pix',...
                    'position',[495 545 50 20],...
                    'fontsize',10,...
                    'BackgroundColor',[.8 .8 .8],...
                    'string','VBE');

%Display the calculated conduction edge
S.ed12 = uicontrol('style','edit',...
                     'unit','pix',...
                     'position',[545 520 70 20],...
                     'fontsize',10,...
                     'string','N/A');  % Displays the value.
S.tex12 = uicontrol('style','text',...
                    'unit','pix',...
                    'position',[495 520 50 20],...
                    'fontsize',10,...
                    'BackgroundColor',[.8 .8 .8],...
                    'string','CBE');

%   Display the calculated band gap
S.ed9 = uicontrol('style','edit',...
                     'unit','pix',...
                     'position',[545 495 70 20],...
                     'fontsize',10,...
                     'string','100');  % Displays the value. Fix this! 100
S.tex9 = uicontrol('style','text',...
                    'unit','pix',...
                    'position',[495 495 50 20],...
                    'fontsize',10,...
                    'BackgroundColor',[.8 .8 .8],...
                    'string','Egap');

 %   Display the calculated valence slope
S.ed13 = uicontrol('style','edit',...
                     'unit','pix',...
                     'position',[735 545 70 20],...
                     'fontsize',10,...
                     'string','N/A');  % Displays the value.
S.tex13 = uicontrol('style','text',...
                    'unit','pix',...
                    'position',[625 545 110 20],...
                    'fontsize',10,...
                    'BackgroundColor',[.8 .8 .8],...
```

```
                  'string','Valence slope');

%   Display the calculated conduction slope
S.ed14 = uicontrol('style','edit',...
                    'unit','pix',...
                    'position',[735 520 70 20],...
                    'fontsize',10,...
                    'string','N/A');  % Displays the value.
S.tex14 = uicontrol('style','text',...
                  'unit','pix',...
                  'position',[625 520 110 20],...
                  'fontsize',10,...
                  'BackgroundColor',[.8 .8 .8],...
                  'string','Conduction slope');


%   Display Standard deviation
S.ed15 = uicontrol('style','edit',...
                    'unit','pix',...
                    'position',[735 495 70 20],...
                    'fontsize',10,...
                    'string','100');  % Displays the value.
S.tex15 = uicontrol('style','text',...
                  'unit','pix',...
                  'position',[625 495 110 20],...
                  'fontsize',10,...
                  'BackgroundColor',[.8 .8 .8],...
                  'string','Flat stdv');

%END OF SLIDER DEFINITIONS
%************************End of GUI Part *********************************%

%***************************Update Plot Section**************************%
%   Gets values from sliders
S.plot1 = get(S.sl,{'min','value','max'});  %Left edge of CB
S.plot2 = get(S.sl2,{'min','value','max'}); %Right edge of CB
S.plot3 = get(S.sl3,{'min','value','max'}); %Left edge of VB
S.plot4 = get(S.sl4,{'min','value','max'}); %Right edge of VB
S.plot5 = get(S.sl5,{'min','value','max'}); %Min value of graph
S.plot6 = get(S.sl6,{'min','value','max'}); %Max value of graph
S.plot7 = get(S.sl7,{'min','value','max'}); %Min value of flat region
S.plot8 = get(S.sl8,{'min','value','max'}); %Max value of flat region

%Get the range for the plot
n_min_temp = []; %creates empty array
n_max_temp = []; %creates empty array

%Takes minimum voltage values set by slider and creates a new array with the data
%points that have values greater than the set value of S.plot5 (Min value of graph)
%The starting value is set by default in GUI code
for j = 1: length(v)
    if S.plot5{2} < v(j)
        n_min_temp = [n_min_temp, j];
    end
```

```
end
n_min = min(n_min_temp); %takes data point # of minimum voltage value for the new range
set by sliders

%Takes maximum voltage values set by slider and creates a new array with the data
%points that have values less than the set value of S.plot6 (Max value of graph)
%The starting value is set by default in GUI code
for j = length(v):-1:1
    if S.plot6{2} > v(j)
        n_max_temp = [n_max_temp, j];
    end
end
n_max = max(n_max_temp); %maximum voltage value of the data for the new range set by
sliders

plot(v(n_min:n_max),didv(n_min:n_max),'k', 'Linewidth', 1.5); %Plots graph
datacursormode on %allows you see the coordinates when you click on the graph

%Sets axes properties
set(gca,'unit','pix','position',[510 120 350 350]); %allows you to modify axes
grid on %displays gridlines
xlabel('Applied bias (V)')
ylabel('dI/dV (arb. unit)')
hold on;

%Get the range for linear fitting for the valence band
for j = 1: length(v)
    if S.plot3{2} < v(j)  %takes VB minimum set by slider
        n_valence_min = j;
        break
    end
end
for j = length(v):-1:1
    if S.plot4{2} > v(j)
        n_valence_max = j; %takes VB maximum set by slider
        break
    end
end


%Get the range for linear fitting for the conduction band
for j = 1: length(v)
    if S.plot1{2} < v(j)
        n_conduction_min = j; %takes CB minimum set by slider
        break
    end
end
for j = length(v):-1:1
    if S.plot2{2} > v(j)
        n_conduction_max = j; %takes CB maximum set by slider
        break
    end
end
```

```
%Calculates a linear fitline using VB min and VB max and plots them
fit_valence =
polyfit(v(n_valence_min:n_valence_max),didv(n_valence_min:n_valence_max),1);
v_fit = v*fit_valence(1) + fit_valence(2); %y = mx + b, where x = voltage
n_valence_end = length(v);
for j = 1: length(v_fit)
    if 0 > v_fit(j)
        n_valence_end = j;
        break
    end
end
plot(v(n_valence_min:n_valence_end), v_fit(n_valence_min:n_valence_end),...
    'b','Linewidth',1.2);

%Calculates a linear fitline using CB min and CB max and plots them
fit_conduction =
polyfit(v(n_conduction_min:n_conduction_max),didv(n_conduction_min:n_conduction_max),1);
v_fit = v*fit_conduction(1) + fit_conduction(2);
n_conduction_end = 1;
for j = length(v_fit):-1:1
    if 0 > v_fit(j)
        n_conduction_end = j;
        break
    end
end
plot(v(n_conduction_end:n_conduction_max), v_fit(n_conduction_end:n_conduction_max),...
    'r','Linewidth',1.2);

%Get the range for flat region
for j = 1: length(v)
    if S.plot7{2} < v(j)
        n_flat_min = j;
        break
    end
end

for j = length(v):-1:1
    if S.plot8{2} > v(j)
        n_flat_max = j;
        break
    end
end

%Sets flat region to zero, plots fit line
numb_zero = length(v(n_flat_min:n_flat_max));
didv_0 = [];
for k = 1:numb_zero
    didv_0 = [didv_0; 0]; %creates an array of zeros for new flat region
end
%fit_flat = polyfit(v(n_flat_min:n_flat_max),didv_0,1);
fit_flat = polyfit(v(n_flat_min:n_flat_max),didv(n_flat_min:n_flat_max),1);

plot(v(n_min:n_max), v(n_min:n_max)*fit_flat(1) + fit_flat(2),...
    'g','Linewidth', 1.2);
```

```
hold off


%Updates plot after slider change
set([S.ed(:);S.sl],'call',{@sl_call,S});          % Shared Callback. %Left CB
set([S.ed2(:);S.sl2],'call',{@sl_call2,S});       % Shared Callback. %Right CB
set([S.ed3(:);S.sl3],'call',{@sl_call3,S});       % Shared Callback. %Left VB
set([S.ed4(:);S.sl4],'call',{@sl_call4,S});       % Shared Callback. %Right VB
set([S.ed5(:);S.sl5],'call',{@sl_call5,S});       % Shared Callback. %Min of graph
set([S.ed6(:);S.sl6],'call',{@sl_call6,S});       % Shared Callback. %Max of graph
set([S.ed7(:);S.sl7],'call',{@sl_call7,S});       % Shared Callback. %Min of flat region
set([S.ed8(:);S.sl8],'call',{@sl_call8,S});       % Shared Callback. %Max of flat region


%Callback function for saving plot picture
function [] = fm_call(varargin)
    % Callback for the figure menu.
        N = inputdlg('Enter a file name.','FileName'); % Get a name.
        %F = getframe(S.fh,get(S.ax,'OuterPosition')+ [80 30 -190 30]);  % Only want to
get axes.
        F = getframe(S.fh);  % Only want to get axes.
        FMT = S.FMT{varargin{1}==S.fm};  % User's format choice.
        imwrite(F.cdata,[N{1},'.',FMT],FMT)  % Write the image.
end
end

%Each of these functions below update the plot after changing
%Slider values
function [] = sl_call(varargin)
    % Callback for the edit box and slider.
    [h,S] = varargin{[1,3]};  % Get calling handle and structure.
    SL = get(S.sl,{'min','value','max'});  % Get the slider's info.
    E = str2double(get(h,'string'));  % Numerical edit string.

    switch h  % Who called?
        case S.ed(1)
            if E <= SL{2}
                set(S.sl,'min',E)  % E is less than current value.
                Updateplot(S)
            elseif E < SL{3}
                set(S.sl,'val',E,'min',E) % E is less than max value.
                set(S.ed(2),'string',E) % Set the current display.
                Updateplot(S)
            else
                set(h,'string',SL{1}) % Reset the value.
                Updateplot(S)
            end
        case S.ed(2)
            if E >= SL{1} && E <= SL{3}
                set(S.sl,'value',E)  % E falls within range of slider.
                Updateplot(S)
            else
                set(h,'string',SL{2}) % User tried to set slider out of range.
```

```
                Updateplot(S)
            end
        case S.ed(3)
            if E >= SL{2}
                set(S.sl,'max',E)  % E is less than current value.
                Updateplot(S)
            elseif E > SL{1}
                set(S.sl,'val',E,'max',E) % E is less than max value.
                set(S.ed(2),'string',E) % Set the current display.
                Updateplot(S)
            else
                set(h,'string',SL{3}) % Reset the value.
                Updateplot(S)
            end
        case S.sl
            set(S.ed(2),'string',SL{2}) % Set edit to current slider
            Updateplot(S)
        otherwise
            % Do nothing
    end
end

function [] = sl_call2(varargin)
    % Callback for the edit box and slider.
    [h,S] = varargin{[1,3]};  % Get calling handle and structure.
    SL = get(S.sl2,{'min','value','max'});  % Get the slider's info.
    E = str2double(get(h,'string'));  % Numerical edit string.


    switch h  % Who called?
        case S.ed2(1)
            if E <= SL{2}
                set(S.sl2,'min',E)  % E is less than current value.
                Updateplot(S)
            elseif E < SL{3}
                set(S.sl2,'val',E,'min',E) % E is less than max value.
                set(S.ed2(2),'string',E) % Set the current display.
                Updateplot(S)
            else
                set(h,'string',SL{1}) % Reset the value.
                Updateplot(S)
            end
        case S.ed2(2)
            if E >= SL{1} && E <= SL{3}
                set(S.sl2,'value',E)  % E falls within range of slider.
                Updateplot(S)
            else
                set(h,'string',SL{2}) % User tried to set slider out of range.
                Updateplot(S)
            end

        case S.ed2(3)
            if E >= SL{2}
                set(S.sl2,'max',E)  % E is less than current value.
```

```
                Updateplot(S)
            elseif E > SL{1}
                set(S.sl2,'val',E,'max',E) % E is less than max value.
                set(S.ed2(2),'string',E) % Set the current display.
                Updateplot(S)
            else
                set(h,'string',SL{3}) % Reset the value.
                Updateplot(S)
            end
        case S.sl2
            set(S.ed2(2),'string',SL{2}) % Set edit to current slider
        Updateplot(S)
        otherwise
            % Do nothing
    end
end

function [] = sl_call3(varargin)
    % Callback for the edit box and slider.
    [h,S] = varargin{[1,3]};  % Get calling handle and structure.
    SL = get(S.sl3,{'min','value','max'});  % Get the slider's info.
    E = str2double(get(h,'string'));  % Numerical edit string.

    switch h  % Who called?
        case S.ed3(1)
            if E <= SL{2}
                set(S.sl3,'min',E)  % E is less than current value.
                Updateplot(S)
            elseif E < SL{3}
                set(S.sl3,'val',E,'min',E) % E is less than max value.
                set(S.ed3(2),'string',E) % Set the current display.
                Updateplot(S)
            else
                set(h,'string',SL{1}) % Reset the value.
                Updateplot(S)
            end
        case S.ed3(2)
            if E >= SL{1} && E <= SL{3}
                set(S.sl3,'value',E)  % E falls within range of slider.
            else
                set(h,'string',SL{2}) % User tried to set slider out of range.
            end
        case S.ed3(3)
            if E >= SL{2}
                set(S.sl3,'max',E)  % E is less than current value.
                Updateplot(S)
            elseif E > SL{1}
                set(S.sl3,'val',E,'max',E) % E is less than max value.
                set(S.ed3(2),'string',E) % Set the current display.
                Updateplot(S)
            else
                set(h,'string',SL{3}) % Reset the value.
                Updateplot(S)
            end
```

```
        case S.sl3
            set(S.ed3(2),'string',SL{2}) % Set edit to current slider.
            Updateplot(S)
        otherwise
            % Do nothing
    end
end

function [] = sl_call4(varargin)
    % Callback for the edit box and slider.
    [h,S] = varargin{[1,3]};  % Get calling handle and structure.
    SL = get(S.sl4,{'min','value','max'});  % Get the slider's info.
    E = str2double(get(h,'string'));  % Numerical edit string.

    switch h  % Who called?
        case S.ed4(1)
            if E <= SL{2}
                set(S.sl4,'min',E)  % E is less than current value.
                Updateplot(S)
            elseif E < SL{3}
                set(S.sl4,'val',E,'min',E) % E is less than max value.
                set(S.ed4(2),'string',E) % Set the current display.
                Updateplot(S)
            else
                set(h,'string',SL{1}) % Reset the value.
                Updateplot(S)
            end
        case S.ed4(2)
            if E >= SL{1} && E <= SL{3}
                set(S.sl4,'value',E)  % E falls within range of slider.
                Updateplot(S)
            else
                set(h,'string',SL{2}) % User tried to set slider out of range.
                Updateplot(S)
            end
        case S.ed4(3)
            if E >= SL{2}
                set(S.sl4,'max',E)  % E is less than current value.
                Updateplot(S)
            elseif E > SL{1}
                set(S.sl4,'val',E,'max',E) % E is less than max value.
                set(S.ed4(2),'string',E) % Set the current display.
                Updateplot(S)
            else
                set(h,'string',SL{3}) % Reset the value.
                Updateplot(S)
            end
        case S.sl4
            set(S.ed4(2),'string',SL{2}) % Set edit to current slider.
            Updateplot(S)
        otherwise
            % Do nothing
    end
end
```

```
function [] = sl_call5(varargin)
    % Callback for the edit box and slider.
    [h,S] = varargin{[1,3]};  % Get calling handle and structure.
    SL = get(S.sl5,{'min','value','max'});  % Get the slider's info.
    E = str2double(get(h,'string'));  % Numerical edit string.

    switch h  % Who called?
        case S.ed5(1)
            if E <= SL{2}
                set(S.sl5,'min',E)  % E is less than current value.
                Updateplot(S)
            elseif E < SL{3}
                set(S.sl5,'val',E,'min',E) % E is less than max value.
                set(S.ed5(2),'string',E) % Set the current display.
                Updateplot(S)
            else
                set(h,'string',SL{1}) % Reset the value.
                Updateplot(S)
            end
        case S.ed5(2)
            if E >= SL{1} && E <= SL{3}
                set(S.sl5,'value',E)  % E falls within range of slider.
                Updateplot(S)
            else
                set(h,'string',SL{2}) % User tried to set slider out of range.
                Updateplot(S)
            end
        case S.ed5(3)
            if E >= SL{2}
                set(S.sl5,'max',E)  % E is less than current value.
                Updateplot(S)
            elseif E > SL{1}
                set(S.sl5,'val',E,'max',E) % E is less than max value.
                Updateplot(S)
                set(S.ed5(2),'string',E) % Set the current display.
                Updateplot(S)
            else
                set(h,'string',SL{3}) % Reset the value.
                Updateplot(S)
            end
        case S.sl5
            set(S.ed5(2),'string',SL{2}) % Set edit to current slider.
            Updateplot(S)
        otherwise
            % Do nothing
    end
end

function [] = sl_call6(varargin)
    % Callback for the edit box and slider.
    [h,S] = varargin{[1,3]};  % Get calling handle and structure.
    SL = get(S.sl6,{'min','value','max'});  % Get the slider's info.
    E = str2double(get(h,'string'));  % Numerical edit string.
```

```
    switch h  % Who called?
        case S.ed6(1)
            if E <= SL{2}
                set(S.sl6,'min',E)  % E is less than current value.
                Updateplot(S)
            elseif E < SL{3}
                set(S.sl6,'val',E,'min',E) % E is less than max value.
                set(S.ed6(2),'string',E) % Set the current display.
                Updateplot(S)
            else
                set(h,'string',SL{1}) % Reset the value.
                Updateplot(S)
            end
        case S.ed6(2)
            if E >= SL{1} && E <= SL{3}
                set(S.sl6,'value',E)  % E falls within range of slider.
                Updateplot(S)
            else
                set(h,'string',SL{2}) % User tried to set slider out of range.
                Updateplot(S)
            end
        case S.ed6(3)
            if E >= SL{2}
                set(S.sl6,'max',E)  % E is less than current value.
                Updateplot(S)
            elseif E > SL{1}
                set(S.sl6,'val',E*.9,'max',E) % E is less than max value.
                set(S.ed6(2),'string',E) % Set the current display.
                Updateplot(S)
            else
                set(h,'string',SL{3}) % Reset the value.
                Updateplot(S)
            end
        case S.sl6
            set(S.ed6(2),'string',SL{2}) % Set edit to current slider.
            Updateplot(S)
        otherwise
            % Do nothing
    end
end


function [] = sl_call7(varargin)
    % Callback for the edit box and slider.
    [h,S] = varargin{[1,3]};  % Get calling handle and structure.
    SL = get(S.sl7,{'min','value','max'});  % Get the slider's info.
    E = str2double(get(h,'string'));  % Numerical edit string.

    switch h  % Who called?
        case S.ed7(1)
            if E <= SL{2}
                set(S.sl7,'min',E)  % E is less than current value.
                Updateplot(S)
```

```
            elseif E < SL{3}
                set(S.sl7,'val',E,'min',E) % E is less than max value.
                set(S.ed7(2),'string',E) % Set the current display.
                Updateplot(S)
            else
                set(h,'string',SL{1}) % Reset the value.
                Updateplot(S)
            end
        case S.ed7(2)
            if E >= SL{1} && E <= SL{3}
                set(S.sl7,'value',E)  % E falls within range of slider.
                Updateplot(S)
            else
                set(h,'string',SL{2}) % User tried to set slider out of range.
                Updateplot(S)
            end
        case S.ed7(3)
            if E >= SL{2}
                set(S.sl7,'max',E)  % E is less than current value.
                Updateplot(S)
            elseif E > SL{1}
                set(S.sl7,'val',E,'max',E) % E is less than max value.
                set(S.ed7(2),'string',E) % Set the current display.
                Updateplot(S)
            else
                set(h,'string',SL{3}) % Reset the value.
                Updateplot(S)
            end
        case S.sl7
            set(S.ed7(2),'string',SL{2}) % Set edit to current slider.
            Updateplot(S)
        otherwise
            % Do nothing
    end
end

function [] = sl_call8(varargin)
    % Callback for the edit box and slider.
    [h,S] = varargin{[1,3]};  % Get calling handle and structure.
    SL = get(S.sl8,{'min','value','max'});  % Get the slider's info.
    E = str2double(get(h,'string'));  % Numerical edit string.


    switch h  % Who called?
        case S.ed8(1)
            if E <= SL{2}
                set(S.sl8,'min',E)  % E is less than current value.
                Updateplot(S)
            elseif E < SL{3}
                set(S.sl8,'val',E,'min',E) % E is less than max value.
                set(S.ed8(2),'string',E) % Set the current display.
                Updateplot(S)
            else
                set(h,'string',SL{1}) % Reset the value.
```

```
                Updateplot(S)
            end
        case S.ed8(2)
            if E >= SL{1} && E <= SL{3}
                set(S.sl8,'value',E)  % E falls within range of slider.
                Updateplot(S)
            else
                set(h,'string',SL{2}) % User tried to set slider out of range.
                Updateplot(S)
            end

        case S.ed8(3)
            if E >= SL{2}
                set(S.sl8,'max',E)  % E is less than current value.
                Updateplot(S)
            elseif E > SL{1}
                set(S.sl8,'val',E,'max',E) % E is less than max value.
                set(S.ed8(2),'string',E) % Set the current display.
                Updateplot(S)
            else
                set(h,'string',SL{3}) % Reset the value.
                Updateplot(S)
            end
        case S.sl8
            set(S.ed8(2),'string',SL{2}) % Set edit to current slider
        Updateplot(S)
        otherwise
            % Do nothing
    end
end

%Base function to update the plot as sliders change
function[] = Updateplot(varargin)
    [S] = varargin{[1]};
    global i;
    S.plot1 = get(S.sl,{'min','value','max'});
    S.plot2 = get(S.sl2,{'min','value','max'});
    S.plot3 = get(S.sl3,{'min','value','max'});
    S.plot4 = get(S.sl4,{'min','value','max'});
    S.plot5 = get(S.sl5,{'min','value','max'});
    S.plot6 = get(S.sl6,{'min','value','max'});
    S.plot7 = get(S.sl7,{'min','value','max'});
    S.plot8 = get(S.sl8,{'min','value','max'});

%Repeated part from beginning of script. Smoothing constant should be updated in this
subsection
list = dir('*.txt');
n = length(list);

%import the voltage values and the I(V) and dI/dV readings
aux = importdata(list(i).name);
disp(list(i).name);

%Save the variables in vectors
```

```
v = aux(:,1);
didv = (aux(:,2));

%If bias sweep begins with positive bias voltage
if v(1)>0
     v=-aux(:,1);
     didv = flip (didv);
     display('Warning: Raw data begins with positive voltage. ')
     display('Note: Bias voltage has been inverted.')
     display ('Note: Also, conductance data has been flipped accordingly.')
     dummy=1;
end


%delete first few points and last few points to avoid trouble areas
pts = 20;
for j=1:pts
    didv(1)=[];
    v(1)=[];
end
for j=length(didv)-pts:length(didv)
    didv(length(didv))=[];
    v(length(v))=[];
end

%If data is turned upside down (180 degrees)
%mdpt = round( length(didv)/2 );
%if didv (mdpt) < 1
%    didv = -didv;
%    display ('Data has been flipped 180 degrees due to phase parameter.')
%end

%Obtain the number of smoothing constant from beginning of script
final_smooth_constant = 30;

%Smooth the dI/dV values
didv = smooth(didv, final_smooth_constant);

%Calculate the offset of the dI/dV curve from zero.
offset = min(didv);
didv = didv - offset;
didv = didv / max(didv);

%Get the range for the plot
n_min_temp = [];
n_max_temp = [];

%Get the range for the plot
for j = 1: length(v)
    if S.plot5{2} < v(j)
        n_min_temp = [n_min_temp, j];
    end
end
n_min = n_min_temp(1);
```

```
for j = length(v):-1:1
    if S.plot6{2} > v(j)
        n_max_temp = [n_max_temp, j];
    end
end
n_max = max(n_max_temp);


plot(v(n_min:n_max),didv(n_min:n_max),'k', 'Linewidth', 1.5)
%Sets axes properties
set(gca,'unit','pix','position',[510 120 350 350]); %allows you to modify axes
grid on %displays gridlines
xlabel('Applied bias (V)')
ylabel('dI/dV (arb. unit)')
hold on;
datacursormode on

%Get the range for linear fitting for the valence band
for j = 1: length(v)
    if S.plot3{2} < v(j)
        n_valence_min = j;
        break
    end
end

for j = length(v):-1:1
    if S.plot4{2} > v(j)
        n_valence_max = j;
        break
    end
end

%Get the range for linear fitting for the conduction band
for j = 1: length(v)
    if S.plot1{2} < v(j)
        n_conduction_min = j;
        break
    end
end

for j = length(v):-1:1
    if S.plot2{2} > v(j)
        n_conduction_max = j;
        break
    end
end

fit_valence =
polyfit(v(n_valence_min:n_valence_max),didv(n_valence_min:n_valence_max),1);
v_fit = v*fit_valence(1) + fit_valence(2);
n_valence_end = length(v);
for j = 1: length(v_fit)
    if 0 > v_fit(j)
```

```
        n_valence_end = j;
        break
    end
end
plot(v(n_valence_min:n_valence_end), v_fit(n_valence_min:n_valence_end),...
    'b','Linewidth',1.2);

fit_conduction =
polyfit(v(n_conduction_min:n_conduction_max),didv(n_conduction_min:n_conduction_max),1);
v_fit = v*fit_conduction(1) + fit_conduction(2);
n_conduction_end = 1;
for j = length(v_fit):-1:1
    if 0 > v_fit(j)
        n_conduction_end = j;
        break
    end
end
plot(v(n_conduction_end:n_conduction_max), v_fit(n_conduction_end:n_conduction_max),...
    'r','Linewidth',1.2);

%Get the range for flat region
for j = 1: length(v)
    if S.plot7{2} < v(j)
        n_flat_min = j;
        break
    end
end

for j = length(v):-1:1
    if S.plot8{2} > v(j)
        n_flat_max = j;
        break
    end
end


numb_zero = length(v(n_flat_min:n_flat_max));
didv_0 = [];
for k = 1:numb_zero
    didv_0 = [didv_0; 0];
end
%fit_flat = polyfit(v(n_flat_min:n_flat_max),didv_0,1);
fit_flat = polyfit(v(n_flat_min:n_flat_max),didv(n_flat_min:n_flat_max),1);


plot(v(n_min:n_max), v(n_min:n_max)*fit_flat(1) + fit_flat(2),...
    'g','Linewidth',1.2);
stdv_flat_region = std(didv(n_flat_min:n_flat_max),1);

%********************End of Update Plot Section**************************%

%******************Effective Band Gap Calculation***********************%

%Calculate VBE using intersection of 2 lines mx +b = nx +c
```

```
VBE = (fit_flat(2) - fit_valence(2))/(fit_valence(1)-fit_flat(1));
CBE = (fit_flat(2) - fit_conduction(2))/(fit_conduction(1) - fit_flat(1));
Eg = CBE - VBE;

Eg_text = 'N/A';
if abs(Eg) < 5
    Eg_text = num2str(Eg);
else
    Eg_text = 'N/A';
end

VBE_text = 'N/A';
if abs(VBE)< 5
    VBE_text = num2str(VBE);
else
    VBE_text = 'N/A';
end

CBE_text = 'N/A';
     if abs(CBE) < 5
          CBE_text = num2str(CBE);
     else
          CBE_text = 'N/A';
     end

set(S.ed11, 'string', VBE_text);
set(S.ed12, 'string', CBE_text);
set(S.ed9, 'string', Eg_text)
set(S.ed13, 'string', num2str(fit_valence(1)));
set(S.ed14, 'string', num2str(fit_conduction(1)));
set(S.ed15, 'string', num2str(stdv_flat_region));

hold off

%***************End of Effective Band Gap Calculation********************%

end
```

Published with MATLAB® R2020b

C.4 Magneto-transport data analysis

In this section, we describe the process for analyzing Hall and resistance data as a function of magnetic field.

C.4.1 Data analysis procedure

For analyzing the magnetoresistance and Hall data, voltages were converted to resistance by dividing the raw data by the applied AC current. The data was then interpolated using 0.01 steps. Because the contacts were not lithographically placed, we made geometric corrections to the data by symmetrizing the longitudinal resistance (R_{xx}) and anti-symmetrizing the transverse resistance (R_{xy}) data. Each spectrum was then multiplied by the respective aspect ratio (W/L) of the contacts. Finally, the longitudinal and transverse conductivity tensor was calculated using resistivity and Hall resistivity data through the following relations.[22]

$$\sigma_{xx}(B) = \frac{\rho_{xx}(B)}{\rho^2_{xx}(B) + \rho^2_{xy}(B)} \tag{C.8}$$

$$\sigma_{xy}(B) = \frac{\rho_{xy}(B)}{\rho^2_{xx}(B) + \rho^2_{xy}(B)} \tag{C.9}$$

where B is the applied magnetic field in the z direction.

C.4.2 Multi-carrier fits

For a sample involving more than one type of carrier, the conductivity-tensor components can be expressed as a sum over the m species present within the multicarrier system:[23]

$$\sigma_{xx}(B) = \sum_{i=1}^{m} \frac{e\, n_i\, \mu_i}{1 + (\mu_i B)^2} \tag{C.10}$$

$$\sigma_{xy}(B) = \sum_{i=1}^{m} S_i \frac{e\, n_i\, \mu_i^2 B}{1 + (\mu_i B)^2} \tag{C.11}$$

where n_i and μ_i are the concentration and mobility of the i-th carrier species, respectively, and S_i is +1 for holes and -1 for electrons.

For the assumption of two conducting channels, surface and bulk, Equations C.8 and C.9 are employed to fit experimental data. For the fitting, we solve for 4 unknown parameters, μ_1, η_1, μ_2, η_2 using the following 4 equations:

$$A = e\, n_1\, \mu_1 + e\, n_2\, \mu_2 \tag{C.12}$$

$$C = \frac{e\, n_1\, \mu_1}{1+ (\mu_2 B)^2} + \frac{e\, n_2\, \mu_2}{1+ (\mu_2 B)^2} \tag{C.13}$$

$$D = e\, n_1 (\mu_1)^2 + e\, n_2 (\mu_2)^2 \tag{C.14}$$

$$E = \frac{e\, n_1\, \mu_1}{1+ (\mu_2 B)^2} + \frac{e\, n_2\, \mu_2}{1+ (\mu_2 B)^2} \tag{C.15}$$

where A and C are $\sigma_{xx}(B)$ values at B = 0 T and B = 14 T, respectively, from experimental data. D is the slope of $\sigma_{xy}(B)$ near B = 0 T and E is the $\sigma_{xy}(B)$ value at B = 14 T from experimental data.

C.5 Figures

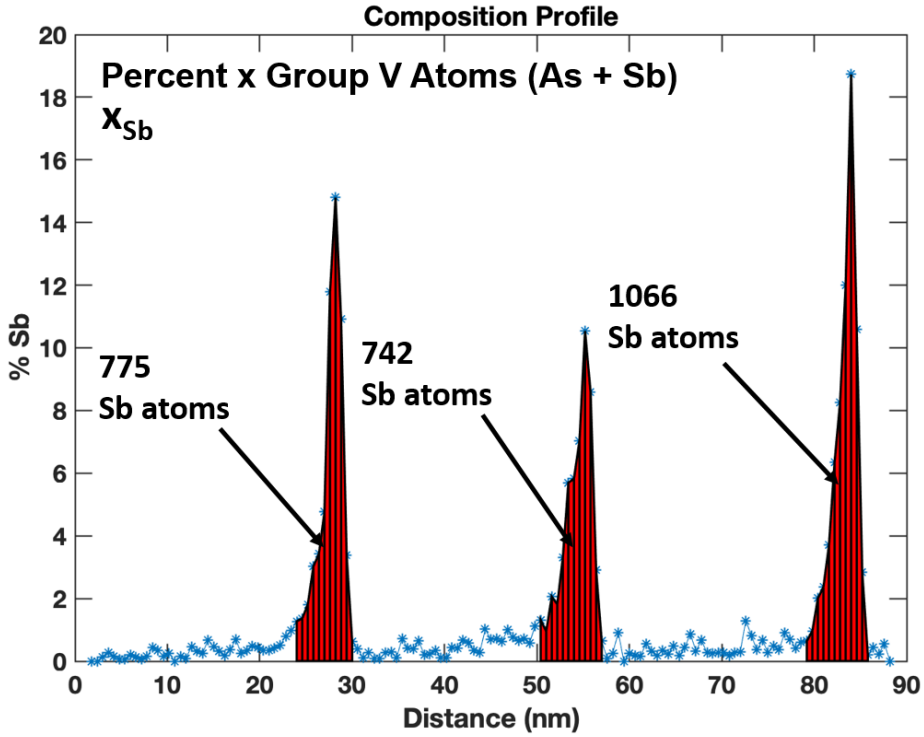

Figure C.1 Example plot of integrated 1D Sb compositional profile showing the number of Sb atoms within each layer for the 4ML GaSb/GaAs multilayered heterostructure. To obtain the LEAP-determined areal densities, the total number of Sb atoms is divided by the cross-sectional area (πr^2) of the cylindrical region used to obtain the 1D profile.

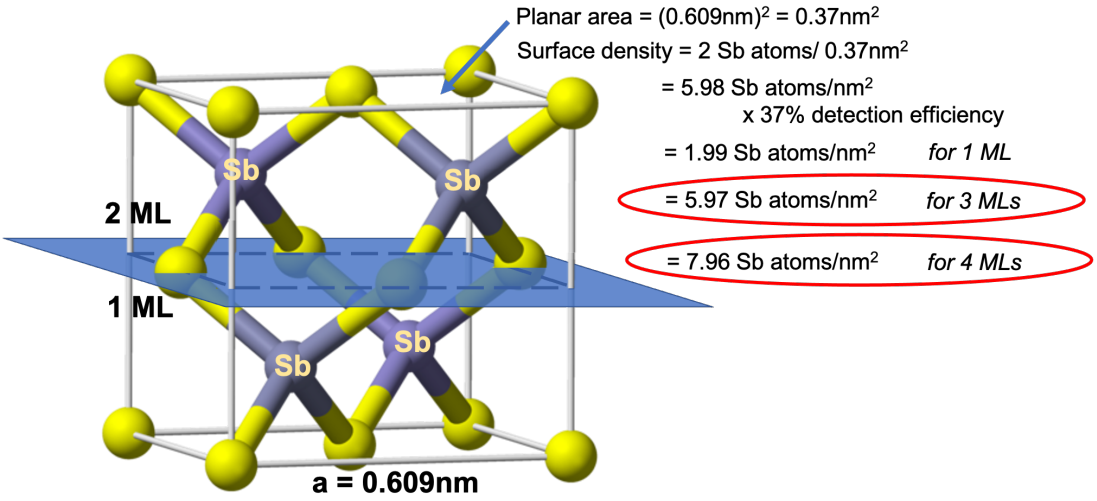

Figure C.2 Method for estimating the theoretical number of deposited Sb atoms. A closely-packed zinc-blende GaSb unit cell was assumed with the lattice constant = 0.609nm. The unit cell consists of 2 monolayers (MLs), with each ML containing two Sb atoms. The Sb surface density in each monolayer is multiplied by the detection efficiency of the LEAP 4000x (37%) to obtain the theoretical number of Sb atoms that should be measured in each ML. The targeted areal densities for 3ML and 4ML growths are estimated to be 5.97 and 7.96 Sb atoms/nm^2, respectively.

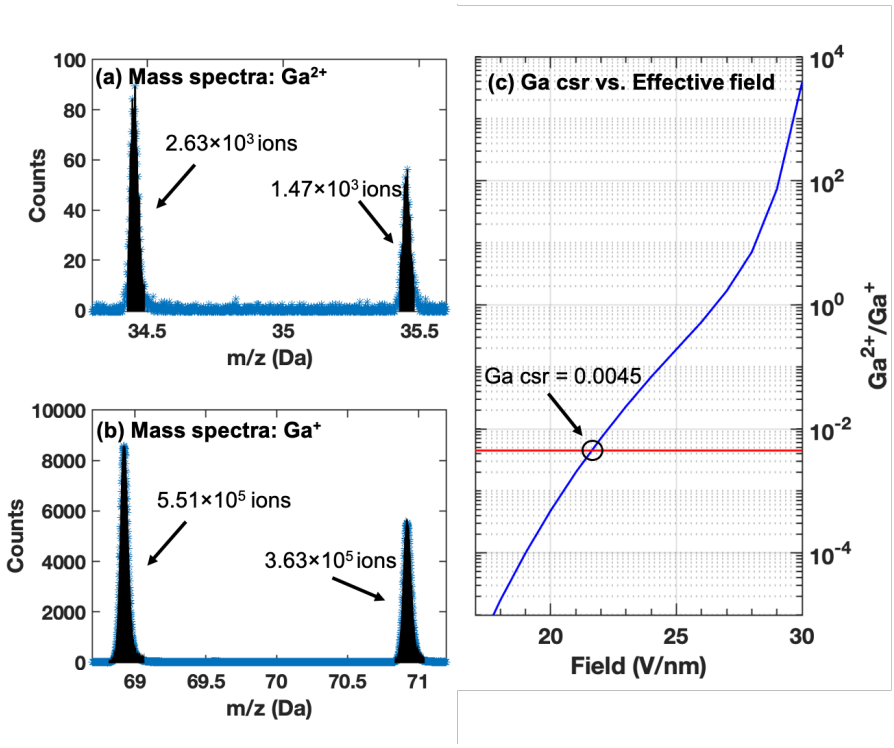

Figure C.3 Example plot of integrated mass spectra showing the number of (a) Ga^{2+} ions at ~34.5 and 35.5 Da and (b) Ga^{+} ions at ~69 and 71 Da from LEAP experiment. The charge-state-ratio is calculated by dividing the total number of Ga^{2+} ions by that of Ga^{+} ions. (c) Plot of csr vs. effective field for Ga adapted from Kingham's probability versus effective field for Ga.[5] Data is corrected for post-ionization, which requires atoms from one charge state to ionize into the next highest charge state.[8]

Appendix D

List of Samples and LEAP runs

Overview

This appendix summarizes the samples examined for this dissertation. LEAP runs are also summarized, along with the respective LEAP experimental conditions.

G.1 List of samples

Sample #	Description		Substrate	Techniques	Growth
RMBE 1333	GaAs	500nm epilayer	GaAs	LEAP	UM
RMBE 1281	GaAsNBi	400nm epilayer	GaAs	LEAP, RBS, XRC	UM
RMBE 1359	GaAsNBi	400nm epilayer	GaAs	LEAP, RBS, XRC	UM
RMBE 1360	GaAsNBi	400nm epilayer	GaAs	LEAP, RBS, XRC	UM
RMBE 1361	GaAsNBi	400nm epilayer	GaAs	LEAP, RBS, XRC	UM
RMBE 1362	GaAsNBi	400nm epilayer	GaAs	LEAP, RBS, XRC	UM
RMBE 1308	GaAsNBi	100nm epilayer	n-GaAs	Hall, XRC	UM
RMBE 1310	GaAsNBi SL	5x GaAs(40nm)/GaAsNBi (20nm)	n-GaAs	XSTM	UM
RMBE 1315	GaAsNBi SL	10x GaAs(10nm)/GaAsNBi(20nm)	n-GaAs	XSTM	UM
RMBE 1316	GaAsNBi SQW	200 nm single QW	n-GaAs	XSTM	UM
RMBE 1317	GaAsNBi SL Ref	10x GaAs(10nm)/GaAsNBi(20nm)	n-GaAs	Hall, XRC	UM
RMBE 1356	GaAsNBi SQW	200 nm single QW	n-GaAs	XSTM	UM
RMBE 1357	GaAsNBi SL	10x GaAs(10nm)/GaAsNBi(20nm)	n-GaAs	XSTM	UM
RMBE 1358	GaAsNBi SL Ref	10x GaAs(10nm)/GaAsNBi(20nm)	n-GaAs	Hall, XRC	UM
R12-131	GaSb QD SL	5x GaSb(3ML)/GaAs(30nm)	p-GaAs	LEAP, PL, STEM	UNM
R12-134	GaSb QD SL	5x GaSb(4ML)/GaAs(30nm)	p-GaAs	LEAP, PL, STEM	UNM
R18-019	GaSb QD SL	IMF/SK superlattice	p-GaAs	XSTM, STS, PL	UNM
R18-020	GaSb QD SL	SK superlattice	p-GaAs	PL	UNM
--	InAs QD SL	5x InAs(3ML)/GaAs(30nm)		LEAP	UM
Wei, 6nm	BiSbTe	6nm epilayer	sapphire	XSTM, STS, MR	UM
20130621	BiSbTe	18nm epilayer, x=0.64	sapphire	XSTM, STS, MR	UM
20130717B	BiSbTe	30nm epilayer, x=0.64	sapphire	XSTM, STS, MR	UM
20130717A	BiSbTe	30nm epilayer, x=0.58	sapphire	XSTM, STS, MR	UM
17023A	TbAs	epilayer	GaAs:Si	--	UDEL
17023B	ErAs/TbAs	superlattice	GaAs:Si	--	UDEL

Table D.1 List of samples examined or referenced in this dissertation.

G.2 Summary of LEAP runs

Sample Name/ LEAP run	Laser-pulse Energy (pJ)/ Voltage-pulse fraction (%)	Frequency (kHz)	Detection Rate (ions/pulse)	Number of ions
RMBE 1281 (R38_09380-v10)	25 pJ	160	0.5	~200k
RMBE 1281 (R38_09380-v11)	20 pJ	160	0.5	~200k
RMBE 1281 (R38_09380-v12)	15 pJ	160	0.5	~200k
RMBE 1281 (R38_09380-v13)	10 pJ	160	0.5	~200k
RMBE 1281 (R38_09380-v14)	5 pJ	160	0.5	~200k
RMBE 1281 (R38_09380-v15)	1 pJ	160	0.5	~200k
RMBE 1281 (R38_09380-v16)	0.25 pJ	160	0.5	~200k
RMBE 1281 (R38_09388)	0.25 pJ	100	0.5	5,076,564
RMBE 1333 (R5094_12099)	0.25 pJ	100	0.4	4,987,977
RMBE 1359 (R5094_12100)	0.25 pJ	100	0.4	6,515,943
RMBE 1360 (R5094_12096)	0.25 pJ	100	0.4	14,489,972
RMBE 1361 (R5094_12097)	0.25 pJ	100	0.4	5,254,747
RMBE 1362 (R5094_12101)	0.25 pJ	100	0.4	6,455,297
RMBE 1333 (R5094_12021)	1 pJ	100	0.4	16,078,407
RMBE 1359 (R5094_12038)	1 pJ	100	0.4	14,501,162
RMBE 1360 (R5094_12094)	1 pJ	100	0.4	8,729,766
RMBE 1362 (R5094_12024)	1 pJ	100	0.4	8,729,766
RMBE 1281 (R38_09853)	1 pJ	100	0.4	17,502474
R13-131 (R38_02747)	20%	200	0.3	14,532,546
R13-134 (R38_02793)	20%	200	0.5	18,007,431
InAs QDs (R38_07652)	20%	200	0.5	20,191,845
InAs QDs (R38_07673)	20%	200	0.5	15,559,073
InAs QDs (R38_07713)	1 pJ	160	0.5	10,281,636
InAs QDs (R38_08691)	1 pJ	200	0.5	5,893,941
InAs QDs (R38_08693)	1 pJ	200	0.5	5,254,536

Table D.2 Summary of LEAP experimental runs, along with LEAP experimental conditions and total number of ions collected.

Appendices References

[1] K. Thompson, D. Lawrence, D.J. Larson, J.D. Olson, T.F. Kelly, and B. Gorman, "In Situ Site-specific Specimen Preparation for Atom Probe Tomography," Ultramicroscopy 107, 131 (2007).

[2] J. Bogdanowicz, A. Kumar, C. Fleischmann, M. Gilbert, J. Houard, A. Vella, W. Vandervorst, "Laser-assisted Atom Probe Tomography of Semiconductors: The Impact of the Focused-ion Beam Specimen Preparation", Ultramicroscopy 188, 19 (2018).

[3] D.J. Larson, T.J. Prosa, R.M. Ulfig, B.P. Geiser, and Th.F. Kelly, "Local Electrode Atom Probe Tomography", Springer-Verlag New York, © (2013).

[4] B.P. Geiser, T.F. Kelly, D.J. Larson, J. Schneir, J.P. Roberts, "Spatial Distribution Maps for Atom Probe Tomography", Microsc. Microanal. 13, 437 (2007).

[5] D.R. Kingham, "The Post-ionization of Field Evaporated Ions: A Theoretical Explanation of Multiple Charge States", Surf. Sci. 116, 273 (1982).

[6] E. Di Russo, I. Blum, J. Houard, G. Da Costa, D. Blavette, and L. Rigutti, "Field-Dependent Measurement of GaAs Composition by Atom Probe Tomography", Microsc. Microanal. 23, 1067 (2017).

[7] G.L. Kellogg, "Pulsed Laser Atom-probe Study of Clean and Oxygen-covered Silicon", Appl. Surf. Sci. 11-2 (Jul), 186-195 (1982).

[8] E. Di. Russo, "Study of the Physical Mechanisms Leading to Compositional Biases in Atom Probe Tomography of Semiconductors", Ph.D. Thesis, Material Chemistry. Normandie Université, 2018. pp. 113-114.

[9] S. Birner, S. Hackenbuchner, M. Sabathil, G. Zangler, J.A. Majewski, T. Andlauer, T. Zibold, R. Morschl, A. Trellakis, and P. Vogl, "Modeling of Semiconductor Nanostructures with nextnano^3", Acta Phys. Pol. A 110, 111 (2006).

[10] I. Vurgaftman, J.R. Meyer, and L.R. Ram-Mohan, "Band parameters for III-V Compound Semiconductors and Their Alloys," J. Appl. Phys. 89, 5815 (2001).

[11] S.-H. Wei and Zunger, "Calculated Natural Band Offsets of All II-VI and III-V Semiconductors: Chemical Trends and the Role of Cation d Orbitals", Appl. Phys. Lett. 72, 2011 (1998).

[12] C.G. Van de Walle, "Band Lineups and Deformation Potentials in the Model-solid Theory", Phys. Rev. B: Condens. Matter **39,** 1871, (1989).

[13] S.-H. Wei and Zunger, "Predicted Band-gap Pressure Coefficients of All Diamond and Zinc-blende Semiconductors: Chemical Trends", Phys. Rev. B: Condens. Matter Mater. Phys. 60, 5404 (1999).

[14] S. Birner, T. Zibold, T. Andlauer, T. Kubis, M. Sabathil, A. Trellakis, and P. Vogl, "nextnano: General Purpose 3-D Simulations", IEEE Trans. Electron Devices. 54, 2137 (2007).

[15] A. Trellakis, T. Zibold, T. Andlauer, S. Birner, R. K. Smith, R. Morschl, and P. Vogl, "The 3D Nanometer Device Project nextnano: Concepts, Methods, Results", J. Comput. Electron. **5,** 285 (2006).

[16] S. Birner, "Modeling of Semiconductor Nanostructures and Semiconductor-electrolyte Interfaces", Ph.D. Thesis, Technische Universitat Muchen, 2011, pp. 33-56.

[17] R. Timm, H. Eisle, A. Lenz, L. Ivanova, V. Vosseburger, T. Warming, D. Bimberg, I. Farrer, D.A. Ritchie, and M. Dahne, "Confined States of Individual Type-II GaSb/GaAs Quantum Rings Studied by Cross-Sectional Scanning Tunneling Spectroscopy", Nano Lett. 10, 2972 (2010).

[18] A.S. Chang, "Nanoscale Studies of Energy Band Gaps and Band Offsets in Compound Semiconductor Heterostructures", PhD Thesis, University of Michigan, 2016.

[19] Mathworks Documentation. Smooth (r2020b). Retrieved October 9, 2020 from https://www.mathworks.com/help/curvefit/smooth.html

[20] Mathworks Documentation. Polyfit (r2020b). Retrieved October 9, 2020 from https://www.mathworks.com/help/matlab/ref/polyfit.html

[21] M. Morgenstern, "Scanning Tunneling Microscopy and Spectroscopy of Graphene on Insulating Substrates", Phys. Status Solidi B 248, 2423 (2011).

[22] Y. Murayama, "Mesoscopic Systems: Fundamentals and Applications, Appendix H Calculation of Conductivity Tensor in a Magnetic Field", Wiley Berlin, 2001, pp.217-221.

[23] J. Antoszewski, D.J. Seymour, and L. Faraone, "Magneto-Transport Characterization Using Quantitative Mobility-Spectrum Analysis", J. Elect. Mat., 24, 9 (1995).

[24] Cameca IVAS software. Retrieved February 8, 2021 from https://www.cameca.com/service/software/ivas

[25] T.F. Kelly, "Atom Probe Tomography", Rev. of Sci. Instruments, 78, 031101 (2007).

[26] M.J. Deen and P.K. Basu, "Silicon Photonics: Fundamentals and Devices, Appendix A: k.p Methods", John Wiley & Sons Ltd, 2012, pp. 403–420.